

# **Electrochemical Cell Modeling of Hierarchically Structured Electrodes in Lithium-Ion Batteries**

Zur Erlangung des akademischen Grades einer  
**Doktorin der Ingenieurwissenschaften (Dr.-Ing.)**  
von der KIT-Fakultät für Maschinenbau des  
Karlsruher Instituts für Technologie (KIT)

genehmigte  
**Dissertation**  
von

M.Sc. Johanna Naumann

Tag der mündlichen Prüfung:	14. März 2025
Referent:	Prof. Dr.-Ing. Marc Kamlah
Korreferent:	Prof. Dr. Hans Jürgen Seifert





This document is licensed under a Creative Commons  
Attribution 4.0 International License (CC BY 4.0):  
<https://creativecommons.org/licenses/by/4.0/deed.en>

# Abstract

The ongoing energy transition increases the need for high-power batteries. Especially suitable for high-power applications are hierarchically structured positive electrodes consisting of porous secondary particles. Since the electrolyte within the secondary particles is in direct contact with the smaller primary particles, diffusion paths in the active material shorten and the surface area of the electrode increases compared to compact particles. Consequently, hierarchically structured electrodes promise a high capacity at fast discharge. However, utilizing the full potential of hierarchically structured electrodes is currently hindered by a lack of understanding of the interplay between their inherent electrochemical processes. Improving hierarchically structured electrodes to enhance battery performance is the subject of current research.

In this work, I investigate how the specific design of the electrode structure influences the battery performance<sup>1</sup>. For this purpose, a continuum cell model is employed, which considers ionic and electronic transport across the electrode and in the secondary particles, the electrochemical reaction at the interface between the electrolyte and the primary particles, and diffusion in the primary particles. I extend the model to separate the effect of different structural properties. Furthermore, I develop a realistic prediction formula for effective ionic transport across hierarchically structured electrodes. Using the model, I study the performance of hierarchically structured electrodes with varying structural properties.

---

<sup>1</sup> Parts of the abstract have previously been published in Naumann et al. (2023) [1]  and Naumann et al. (2024) [2] . The texts have been combined and modified.

My simulations show that depending on the electrode structure, diffusion within the active material, ionic transport across the electrode, or electronic conductivity within the secondary particles limits the battery performance at high discharge rates. Mitigating these limits requires small primary particles and a thin electrode, as well as sufficient electronic conductivity in the secondary particles by the active material or additional carbon components. Furthermore, I show that compacting hierarchically structured electrodes shifts ionic transport from the pore space between secondary particles toward transport through the particle porosity. Models have to account for the latter if electrodes are highly compacted. The modeling framework and specific recommendations developed in this work enable the optimization of hierarchical electrode structures toward high power, which contributes to pushing the energy transition forward.





# Kurzfassung

Mit dem Voranschreiten der Energiewende steigt der Bedarf an Hochleistungsbatterien. Besonders geeignet für Hochleistungsanwendungen sind hierarchisch strukturierte positive Elektroden, die aus porösen Sekundärpartikeln bestehen. Da der Elektrolyt innerhalb der Sekundärpartikel in direktem Kontakt mit den kleineren Primärpartikeln steht, verkürzen sich die Diffusionswege im Aktivmaterial und die innere Oberfläche der Elektrode steigt im Vergleich zu dichten Partikeln an. Folglich stellen hierarchisch strukturierte Elektroden eine hohe Kapazität bei schneller Entladung in Aussicht. Die Nutzung des vollen Potenzials von hierarchisch strukturierten Elektroden wird derzeit jedoch durch ein mangelndes Verständnis des charakteristischen Zusammenspiels ihrer elektrochemischen Prozesse beeinträchtigt. Die Verbesserung hierarchisch strukturierter Elektroden zur Erhöhung der Batterieleistung ist Gegenstand der aktuellen Forschung.

In dieser Arbeit untersuche ich, wie der konkrete Aufbau der Elektrodenstruktur die Leistungsfähigkeit der Batterie beeinflusst<sup>1</sup>. Zu diesem Zweck wird ein Kontinuumszellmodell verwendet, das den Ionen- und Elektronentransport durch die Elektrode und in den Sekundärpartikeln, die elektrochemische Reaktion an der Grenzfläche zwischen Elektrolyt und Primärpartikeln, sowie die Diffusion in den Primärpartikeln berücksichtigt. Ich erweitere das Modell, um den Einfluss verschiedener Struktureigenschaften separat zu betrachten. Des Weiteren entwickle ich eine realistische Formel zur Vorhersage des effektiven Ionentransports durch hierarchisch strukturierte Elektroden. Mithilfe des Modells untersuche ich

---

<sup>1</sup> Teile der Kurzfassung wurden im Vorfeld in Naumann et al. (2023) [1]  und Naumann et al. (2024) [2]  veröffentlicht. Die Texte wurden zusammengeführt und verändert.

das Verhalten von hierarchisch strukturierten Elektroden mit unterschiedlichen Struktureigenschaften.

Meine Simulationen zeigen, dass je nach Elektrodenstruktur die Diffusion innerhalb des Aktivmaterials, der Ionentransport durch die Elektrode oder die elektronische Leitfähigkeit innerhalb der Sekundärpartikel die Leistungsfähigkeit der Batterie bei hohen Entladeraten einschränkt. Die Reduzierung dieser Limitierungen erfordert kleine Primärpartikel und eine dünne Elektrode sowie eine ausreichende elektronische Leitfähigkeit in den Sekundärpartikeln aufgrund des Aktivmaterials oder zusätzlicher Kohlenstoffanteile. Darüber hinaus zeige ich, dass die Verdichtung hierarchisch strukturierter Elektroden den Ionentransport vom Porenraum zwischen den Sekundärpartikeln hin zum Transport durch die Porosität der Partikel verlagert. Letzteres muss in Modellen berücksichtigt werden, wenn Elektroden stark verdichtet sind. Der Modellierungsansatz und die spezifischen Empfehlungen, die in dieser Arbeit entwickelt wurden, ermöglichen die Optimierung hierarchischer Elektrodenstrukturen bezüglich einer hohen elektrischen Leistung, was dazu beiträgt, die Energiewende voranzutreiben.

# Acknowledgements

I could write this thesis thanks to the manifold support I received over the entire period.

First of all, I would like to thank Prof. Dr.-Ing. Marc Kamlah for his extremely close supervision. You entrusted me with an exciting topic and allowed me to benefit from your great knowledge and experience. Your openness and support for all my ideas made the doctorate an enormously enriching experience for me. At the right moments, you had a confident perspective that kept me motivated.

I sincerely thank Associate Professor Dr.-Ing. Yixiang Gan for cordially welcoming me at USYD. Sharing your profound expertise has greatly enriched this work. I would like to thank Prof. Dr. Hans Jürgen Seifert for taking over the role of my second supervisor and for your sincere interest in my work. Thanks also to Prof. Dr.-Ing. Dipl.-Psych. Barbara Deml for chairing my doctoral examination.

I want to express my sincere thanks to Dr. Joachim R. Binder. During our exciting collaboration, you introduced me to the world of experimental battery research. I also thank my other cooperation partners: Dr. Marcus Müller for your valuable input, Dipl.-Ing. Nicole Bohn for your helpfulness, and Ass. Prof. Dr. Matthias Neumann for the many discussions. A huge thank you goes to Dr.-Ing. Oleg Birkholz. You laid the foundation for my work and patiently onboarded me.

During my doctorate, I was lucky to be surrounded by wonderful colleagues. I would like to thank the entire canteen crew for the lovely joint lunches and my colleagues at the IAM-MMI and POLiS for the great atmosphere. Important to mention are my proofreaders and test listeners Alex, Alexandra, Filiz, Max, Nils, Paula, Sabrina, Thimo, and Vanessa. Thank you for your valuable feedback.

Finally, my deepest gratitude goes to my friends and family. You are the support that enables me to go through life with joy and motivation.

Karlsruhe, im Monat April 2025

*Johanna Naumann*

# Contents

<b>Abstract</b>	<b>i</b>
<b>Kurzfassung</b>	<b>iii</b>
<b>Acknowledgements</b>	<b>v</b>
<b>1 Introduction</b>	<b>1</b>
1.1 Motivation	1
1.2 Objectives	2
1.3 Structure	3
<b>2 Battery Fundamentals</b>	<b>5</b>
2.1 Intercalation Batteries	5
2.2 Battery Terminology	8
2.3 Active Material for the Positive Electrode	10
2.4 Hierarchically Structured Electrodes	11
2.5 Electrochemical Battery Modeling	13
<b>3 Modeling Hierarchically Structured Electrodes</b>	<b>17</b>
3.1 Hierarchically Structured Cell Model	17
3.2 Effective Transport Properties	25
3.3 Ionic Transport in Hierarchically Structured Electrodes	29
3.4 Electrochemically Active Surface Area	31
3.5 Properties of Hierarchically Structured NMC Electrodes	33
3.6 Properties of Calendered Hierarchically Structured NMC Electrodes	38

<b>4 Influences of Morphology on the Cell Performance of Hierarchically Structured Electrodes . . . . .</b>	<b>43</b>
4.1 Effect of Electrochemically Active Surface Area on Reaction Kinetics . . . . .	44
4.2 Interplay between Secondary Particle Porosity and Electronic Conductivity . . . . .	47
4.3 Dependence of Electronic Conductivity on the Secondary Particle Size . . . . .	51
4.4 Limitations Due to Primary Particle Size and Solid Diffusion . .	54
4.5 Impact of Ionic Transport Depending on Electrode Thickness . .	58
<b>5 Ionic Transport Paths in Hierarchically Structured Electrodes</b>	<b>61</b>
5.1 Effective Ionic Transport . . . . .	62
5.2 Effect on the Cell Performance . . . . .	65
<b>6 Summary and Outlook . . . . .</b>	<b>69</b>
<b>Bibliography . . . . .</b>	<b>73</b>
<b>List of Figures . . . . .</b>	<b>101</b>
<b>List of Tables . . . . .</b>	<b>105</b>
<b>List of Abbreviations and Symbols . . . . .</b>	<b>107</b>
<b>A Cell Production and Experimental Testing . . . . .</b>	<b>115</b>
A.1 Electrodes A-D and E1-E4 . . . . .	115
A.2 Electrodes Cal-1, Cal-2, and Cal-3 . . . . .	116
<b>B Cell Properties . . . . .</b>	<b>117</b>
B.1 Reference Cell E1 . . . . .	119
B.2 Electrodes Cal-1, Cal-2, and Cal-3 . . . . .	123
<b>C Hashin-Shtrikman Bound . . . . .</b>	<b>129</b>

<b>D Extensive Simulation Results of Electrodes Cal-1, Cal-2, and Cal-3 . . . . .</b>	<b>131</b>
---	------------





# 1 Introduction

## 1.1 Motivation

One of the big challenges of our time is the reduction of CO<sub>2</sub> emissions. Consequently, processes that consume energy have to be electrified and the electricity itself must come from sustainable sources. Renewable energy sources like solar and wind energy are often available intermittently. Therefore, they strongly benefit from energy storage to balance peak production times with downtime. Furthermore, mobile devices require efficient and lightweight energy storage. Batteries are powerful and flexible energy storage systems because they combine a high energy density with the possibility to adapt size, capacity, and voltage. In the last decades, batteries have become a key technology to enable the transition of the energy and transport sectors to sustainability.

For high-power applications including freight transportation [3] and laser technology [4], batteries need to release energy quickly. Fast discharge often drastically reduces the amount of energy a battery cell can deliver. In this case, the low ion mobility within the active material limits the rate capability [5]. There are two approaches to improving the cell performance at high discharge rates: One approach is to enhance the material properties of the electrodes [6]. The second possibility lies in adapting the electrode structure [7], which will be the focus of this work. Downsizing electrode particles mitigates the limitation of slow diffusion in the active material. Furthermore, it increases the interface area between the electrolyte and the active material, which has proven effective in enabling fast reaction kinetics [8, 9]. However, nanoparticle electrodes suffer from challenges concerning processing and cycling [10, 11]. As an alternative, nanosized active

material particles, i.e. primary particles, may be assembled into porous secondary particles. The resulting hierarchical structure combines short transport paths in the active material, a high electrochemically active surface area, and a long cycle life [12–14].

In hierarchically structured electrodes (HSEs), transport and electrochemical processes take place at different length scales, i.e. electrode scale, secondary particle scale, and primary particle scale. A good cell performance depends on balancing out all processes. Consequently, the morphology of HSEs needs to be carefully designed. Recent experimental investigations have gained first insights into the relationship between electrode morphology and cell performance [15]. However, experimental investigations are time-consuming and cannot clearly separate morphological features. Cell modeling complements experimental investigations by a systematic variation of single morphological properties and a detailed picture of their influence on the discharge process to close the gaps in understanding the effect of morphology and its interrelation with the properties of the electrode materials.

## 1.2 Objectives

The present work investigates the effect of morphology on the discharge performance of hierarchically structured positive electrodes. For this purpose, I will set up a continuum modeling framework for HSEs, which is suitable for studying a variation of their relevant morphological features. Computationally efficient continuum cell models facilitate the variation of many input parameters within a large range of values while incorporating the different scales of HSEs. I will extend an existing continuum model [16] to examine the influence of the electrochemically active surface area as an independent parameter and to enable the investigation of ionic transport in highly compacted HSEs. The model will be validated using experimental results. Next, I will examine the rate capability of HSEs with different morphologies. Specifically, the influence of electrochemically active surface area, secondary particle porosity and size, primary particle

size, electrode thickness, and electrode compaction will be illustrated. My goal is to explain the resulting cell performance based on the underlying electrochemical processes. Furthermore, I will illuminate the interrelation between electrode morphology and properties of the electrode materials. In summary, this work aims to create a modeling tool that can be easily adapted to different types of HSEs and to offer a detailed picture of the electrochemical effects determining the cell performance in HSEs.

## 1.3 Structure

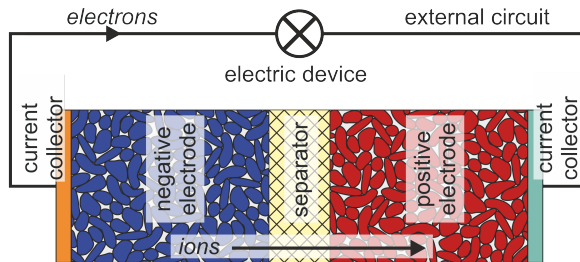
The work is structured as follows. After introducing the motivation and objectives of this work in Chapter 1, Chapter 2 explains the setup and general working principle of intercalation batteries. I introduce relevant concepts to describe cell operation and give background on the active material which serves as a basis for the investigations in this work. Furthermore, HSEs are described in detail including processing and performance. Finally, the chapter contains an overview of battery modeling with a focus on continuum cell models as well as recent work on modeling porous secondary particles and hierarchically porous systems. Chapter 3 introduces the methods used in this work. The selected continuum cell model for HSEs and its inherent concept of effective transport properties are outlined. I develop a new formula for the effective ionic transport in HSEs. In addition, the chapter reports two more extensions I made to the model, i.e. accounting for the contact resistance between the electrode and the current collector as well as separating the electrochemically active surface area from other morphological features. Finally, the chapter presents the studied electrodes and the comparison between model and experimental results. In Chapter 4, I study the interplay of morphology, material properties, electrochemical processes, and cell performance in HSEs. For this purpose, electrochemically active surface area, secondary particle porosity and size, primary particle size, and electrode thickness are varied. I explain their effect on the discharge behavior of the cell based on the electrochemical behavior of the electrode. Furthermore, I extrapolate the

results to HSEs of different material properties like diffusivity in the active material, electronic conductivity in the secondary particles, and reaction rate constant. Chapter 5 deals with the effect of electrode compaction. Ionic transport across HSEs at different intergranular porosities and its effect on cell performance are discussed. Moreover, I evaluate the formula developed in Chapter 3 and draw conclusions concerning the ionic transport paths. Chapter 6 summarizes the methods developed in Chapter 3 as well as the results obtained in Chapters 4 and 5. Finally, I contextualize the work in the current and future landscape of research and development.

## 2 Battery Fundamentals

### 2.1 Intercalation Batteries

Batteries are energy storage devices based on electrochemistry [17, 18]. They consist of one or more interconnected cells, which are the smallest functional unit. A battery cell contains two electrodes and a separator sandwiched between them, which spatially and electronically isolates the electrodes from each other (Fig. 2.1). The entire cell is soaked with electrolyte. When connected to an external circuit, the cell spontaneously discharges and converts its stored chemical energy to electric energy, which can be used to power a connected device. The driving force for the discharge is the potential difference between the two electrodes. During discharge, the negative electrode releases electrons as well as ions, maintaining the overall electroneutrality of the electrode. While the electrons leave the electrode and migrate through the external circuit, the ions dissolve in the electrolyte and move from the negative to the positive electrode. Since the




**Figure 2.1:** Working principle of an intercalation battery cell during discharge.

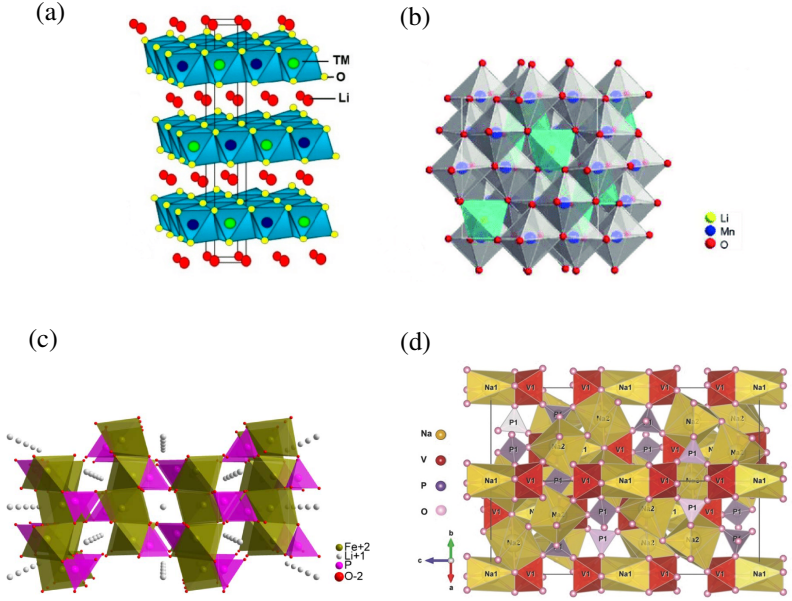
separator is a porous membrane, dissolved ions can travel through its pores. In the positive electrode, the ions recombine with the electrons and are incorporated into the electrode's active material. In primary batteries, the cell can perform only one discharge whereas in secondary batteries, the process is reversible and a connected power source can recharge the cell.

One specific type of secondary battery is the intercalation battery [23]. Here, the active material reversibly stores the shuttling ions by incorporating them into the crystal structure without chemically changing it. Once intercalated at the active material surface by an electrochemical reaction, the ion may diffuse through a network of lattice sites within the active material or reversibly deintercalate, thus leaving the material again by the reverse electrochemical reaction. Typical shuttling ions include lithium [24–27] and sodium [28–32]. The negative electrode is usually carbon-based, i.e. graphite for lithium-ion batteries (LIBs) or hard carbon for sodium-ion batteries (NIBs). Experimental setups may use half-cells with a plain lithium or sodium negative electrode to separately study effects at the positive electrode. In contrast to the negative electrode, a variety of active materials are available for the positive electrode, e.g. layered [33–40] (Fig. 2.2a), spinel [41, 42] (Fig. 2.2b), olivine [43–47] (Fig. 2.2c), or sodium superionic conductor (NASICON) [22] (Fig. 2.2d) materials.

To ease lithiation/sodiation, the active material has a granular form with particles in the nanometer to micrometer range [48–52]. This shortens diffusion paths in the active material and increases the electrochemically active surface area, where the electrochemical reaction takes place at the interface between the active material and the electrolyte. The granular particle structure is fixated by a polymer binder, which may incorporate carbon additives to enhance the electronic conductivity of the electrode. The metallic current collectors electronically connect each electrode to an external circuit. During production, the electrode films are directly coated onto the current collector foils<sup>1</sup>. Then, a calendaring step mechanically compresses the electrode, reducing thickness and porosity as well as

---

<sup>1</sup> Part of this paragraph has previously been published in Naumann et al. (2024) [2] . The text has been modified.



**Figure 2.2:** Crystal structures of intercalation materials: (a) layered<sup>[a]</sup>, (b) spinel<sup>[b]</sup>, (c) olivine<sup>[c]</sup>, (d) NASICON<sup>[d]</sup>.

[a] Layered structure of NCM compound. By Julien et al. (2020) [19]

[b] Crystal structure of spinel  $\text{LiMn}_2\text{O}_4$ . By Ding (2019) [20]

[c] Visualization of  $\text{LiFePO}_4$  crystal structure, viewing along [010] direction. By Molenda et al. (2013) [21]

[d] Crystal structure of  $\text{Na}_3\text{V}_2(\text{PO}_4)_3$  (110-face). Used with permission of John Wiley & Sons - Books, from "Challenges and Perspectives for NASICON-Type Electrode Materials for Advanced Sodium-Ion Batteries", *Advanced Materials*, Chen, Shuangqiang; Wu, Chao; Shen, Laifa; Zhu, Changbao; Huang, Yuanye; Xi, Kai; Maier, Joachim; Yu, Yan, vol. 29, no. 48, 2017 [22]; permission conveyed through Copyright Clearance Center, Inc.

ensuring good contact between active material, electronically conductive additives, and current collector. As a result, the volumetric energy density increases and the electronic conductivity through the electrode improves [53]. However, calendaring also aggravates the resistance for ionic transport in the pore space by raising the tortuosity [54]. After assembling the electrodes and separator into the cell, the pore space is soaked with electrolyte. Suitable liquid electrolytes include salts of the shuttling ion dissolved in non-aqueous organic solvents [55–58].

## 2.2 Battery Terminology

To describe the amount of shuttling ions present in the active material, the degree of lithiation/sodiation  $\xi$  (more commonly  $x$ ) is used [59]. It specifies the fraction of occupied lattice sites and ranges between  $\xi = 0$  for lack of shuttling ions to  $\xi = 1$  for full occupancy. E.g. the stoichiometry  $\text{Li}_\xi\text{MO}_2$  ( $M = \text{Ni}, \text{Mn}, \text{Co}$ ) describes a layered oxide. Usually, the active material degrades for low  $\xi$ . Therefore, a cell is only discharged to a specified cut-off voltage. Lithiation/sodiation of an electrode causes a change in Gibb's free energy  $\Delta G$ , which determines the open-circuit voltage (OCV) of the cell

$$U_{\text{OCV}} = -\frac{\Delta G}{n_{\text{eon}}F} \quad (2.1)$$

with  $n_{\text{eon}}$  transferred electrons and Faraday's constant  $F$ . For infinitely slow charge or discharge, the cell voltage equals the OCV. At faster discharge rates, the resistances within the cell cause an overpotential, which lowers the acquired voltage compared to the OCV. This reduces the capacity

$$Q = \int i_{\text{app}} A^{\text{pos}} dt, \quad (2.2)$$

which may be calculated from the extractable discharge current density  $i_{\text{app}}$  across the cross-sectional area  $A^{\text{pos}}$  of the electrode during time  $t$ . Batteries may be cycled galvanostatically at a constant current or potentiostatically at a



constant voltage. Galvanostatic discharge rates are classified by their relation to the maximum capacity of the cell. An  $nC$  discharge current

$$i_{\text{app}} = n \frac{L^{\text{pos}} \epsilon_s F (c_{s,\text{max}} - c_{s,0})}{3600\text{s}} \quad (2.3)$$

corresponds to a rate which extracts  $n$  times the maximum capacity per hour from an electrode with thickness  $L^{\text{pos}}$ , volume fraction of the active material  $\epsilon_s$ , maximum concentration of shuttling ions in the active material  $c_{s,\text{max}}$  and initial concentration in the active material  $c_{s,0}$ . Rate capability denominates the ability of a battery to retain a high capacity at high C-rates. The percentage of capacity available in the cell at a certain time is called the state of charge (SOC). Accordingly, the percentage of capacity missing until full charge at a certain time is called the depth of discharge (DOD). SOC and DOD are based on the nominal capacity, which is the theoretical maximum capacity an electrode can deliver. The reversibly accessible capacity usually lies below this, even for slow discharge. To compare the electrochemical performance of different active materials, the specific capacity

$$Q_{\text{spec}} = \frac{Q}{m_s} \quad (2.4)$$

with active material mass  $m_s$  of the electrode may be used. Other measures for electrode performance include energy and power. The stored energy of a battery

$$E = \int U_{\text{cell}} dQ \quad (2.5)$$

may be acquired from the measured capacity  $Q$  and cell voltage  $U_{\text{cell}}$  (Fig. 2.3). Relating the storable energy to active material mass or volume of an electrode yields specific energy or energy density, respectively. Power  $P$  with

$$P = \frac{\partial E}{\partial t} \quad (2.6)$$

indicates the rate at which a battery can deliver energy per time.

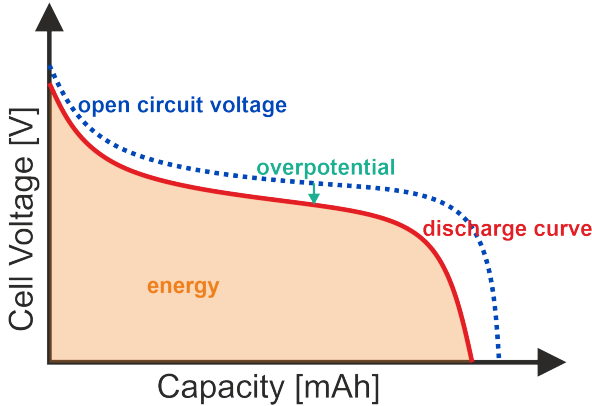


Figure 2.3: Schematic of a discharge curve.

## 2.3 Active Material for the Positive Electrode

With a 50% share of the LIB market [60], lithium nickel manganese cobalt oxide (NMC) is one of the standard commercialized active materials for the positive electrode. Especially its high energy density [61] and rate capability [62] qualify the material for high-tech applications. NMC has a layered crystal structure with alternating layers of  $\text{MO}_6$  ( $\text{M} = \text{Ni}, \text{Mn}, \text{Co}$ ) octahedra and mobile lithium atoms. The electrochemical properties of NMC depend on the ratio of nickel, manganese, and cobalt [61]. A sufficient manganese content ensures chemical stability [63], while high-nickel NMC provides higher voltage and capacity [61], and cobalt ensures good cycling stability [64]. Recent efforts have targeted a low cobalt content due to its scarcity and high cost [65].



$\text{LiNi}_{1/3}\text{Mn}_{1/3}\text{Co}_{1/3}\text{O}_2$  (NMC111) with an even ratio of nickel, manganese, and cobalt, balances the advantages of all components. Deintercalating lithium from NMC111 oxidizes the nickel and cobalt cations from their original states  $\text{Ni}^{2+}$  and  $\text{Co}^{3+}$  to  $\text{Ni}^{4+}$  and  $\text{Co}^{4+}$ , while manganese remains in its original oxidation state  $\text{Mn}^{4+}$  [66, 67]. Utilizing the full theoretical capacity of  $276 \text{ mAh g}^{-1}$  [66] would involve deep delithiation. Since this causes an undesired phase transition

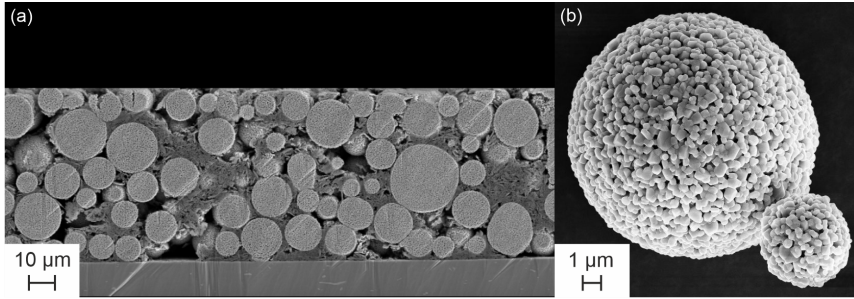
[68], cycling is usually performed below 4.6 V [66] yielding reversible capacities just over 200 mA h g<sup>-1</sup> [62].


## 2.4 Hierarchically Structured Electrodes

Delivering high power depends on the rate capability of battery cells<sup>2</sup>. One approach to improve the rate capability is the hierarchical structuring of the positive electrode [69, 70] (Fig. 2.4a). The secondary active material particles (Fig. 2.4b) consist of interconnected nanoparticles called primary particles. Hierarchically structured electrodes (HSEs) incorporate two classes of pores: the intragranular porosity inside the secondary particles and the intergranular porosity between the secondary particles. The open intragranular porosity is accessible for the electrolyte. Compared to a conventional electrode setup with compact secondary particles, the electrochemically active surface area of the electrode enlarges [13, 71] and transport paths in the active material shorten [12, 69]. This ensures fast reaction kinetics [70, 72] and mediates limitations due to solid diffusion [12, 73, 74]. Consequently, the specific capacity increases [15, 71, 75], especially at high insertion and extraction rates [72, 76].

Due to their small size, the primary particles experience less cracking than compact secondary active material particles [77]. Furthermore, the intragranular porosity of the secondary particles can buffer volume changes, e.g. of phase-transition active materials [78–80]. Both the small primary particle size and the secondary particle porosity reduce degradation and increase cycle life [14, 75, 81]. HSEs maintain a high volumetric energy density [82, 83] and experience few unwanted side reactions [84]. Contrary to electrodes from loose nanoparticles [85–87], HSEs continue to grant access to the primary particle surfaces during cycling [74] and require less carbon and binder additives [88]. HSEs

<sup>2</sup> Parts of the following chapter have previously been published in Naumann et al. (2023) [1]  and Naumann et al. (2024) [2] . The texts have been combined and modified.



**Figure 2.4:** SEM images: (a) Cross-section of hierarchically structured electrode E2 (see Chapter 4) with 73  $\mu\text{m}$  thickness. (b) Secondary particle of comparable powder to F900 from Wagner et al. [15] (see Chapter 4). Images by Amalia Wagner and Nicole Bohn. The images have previously been published in Naumann et al. (2023) [1] .

possess the additional advantage of allowing for the incorporation of carbon additives within the secondary particles. This approach may boost the electronic conductivity within the secondary particles [12, 70, 72]. Active materials with a low intrinsic electronic conductivity benefit from this approach, resulting in an improved cell performance [12]. Hierarchical electrode designs have been applied to a multitude of innovative battery technologies, including sodium [12, 89], potassium [90], zinc [91], and lithium-sulfur [92] batteries.

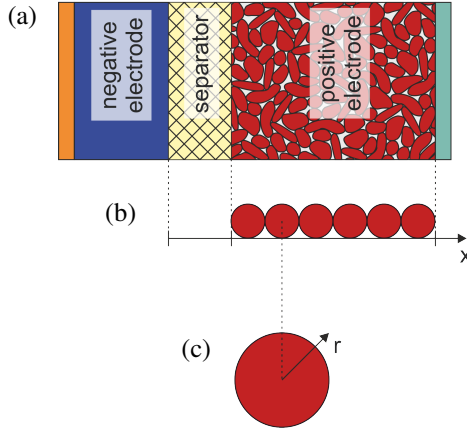
Electrode architecture also affects the ionic resistance of battery electrodes. In HSEs, the tortuosity is higher than in electrodes with compact particles at a given total electrode porosity [93]. Calendering HSEs initially reduces the intergranular pore space while the porous particles remain intact [88]. They may undergo a plasticity-like deformation to eliminate intergranular pores while maintaining their original intragranular porosity. Schneider et al. [93] found a strong increase in tortuosity when the intergranular porosity is eliminated at an electrode porosity of around 0.3. The small intragranular pore size causes a higher tortuosity than large intergranular pores at the same porosity. Below electrode porosities of 0.3, intragranular porosity may change due to massive compression [93] or fracture [94] of secondary particles.

A variety of processing routes can yield porous secondary active material particles. Many of them treat the mixture of precursor materials and solvent in order to achieve porous agglomerates, including hydrothermal treatment [13], freeze-drying [14], the use of a complexing agent and fuel [72], atomization [69], or spray-drying [12, 70]. Spray-drying can also obtain porous structures from nanoparticles of commercially available active material [15, 88]. Subsequent exposure to high temperatures leads to crystalline growth and sintering of primary particles, which forms the final secondary particles. At the same time, the heat treatment finalizes the synthesis of the active material. Another way to obtain porous secondary particles uses a finely distributed carbon source within the solvent-precursor mixture to restrict the size of developing primary particles [81]. The carbon source is decomposed in the following heat treatment, yielding carbon and porosity. Depending on the processing, the final morphology of the secondary particles may depend on the composition of the solvent-precursor-mixture, the size and shape of initial nanoparticles, and the processing conditions [83, 95].

## 2.5 Electrochemical Battery Modeling

Battery cells in general can be modeled in different levels of detail. Phenomenological models [96–98] provide high-level descriptions of cell behavior by approximating experimental observations. Equivalent-circuit models [99–101] present a popular example. They use common electronic elements like resistors and capacitors to fit the cell voltage. In contrast, electrochemical models [102, 103] rely on the physical processes within the cell and may employ a continuum [104] or spatially resolved [105] approach. Compared to phenomenological models, they possess greater predictive capability. Finally, atomistic models [106] provide an understanding of active material behavior at the Angstrom scale.

Among the electrochemical models, Doyle-Fuller-Newman (DFN) models [107–115] and single particle models (SPMs) [116–118] are most popular. DFN models combine porous electrode theory [59, 119, 120] with concentrated solution




**Figure 2.5:** Schematic of a Doyle-Fuller-Newman (DFN) model. (a) Half-cell for reference. (b) Half-cell level (coordinate  $x$ ) and (c) particle level (coordinate  $r$ ) of the DFN model.


theory [59, 121] and an expression for the electrochemical reaction. In the direction from the separator to the current collector, DFN models view the cell (Fig. 2.5a) as a one-dimensional continuum (Fig. 2.5b). Therefore, potentials and concentrations within the cell are continuum quantities. At each position, a continuum quantity represents the volume average of the microscopic distribution of that quantity in the vicinity of the position. The evolution of the solid-state potential in the electrodes is described by Ohm's law, viewing active material and additives as the solid phase. In the electrolyte, the potential is determined by Kirchhoff's law and Ohm's law, while the concentration is determined by Fick's law of diffusion. Only the concentration in the active material particles is spatially resolved but assumed to be spherically symmetric (Fig. 2.5c). Its evolution is tracked by Fick's law of diffusion. The cell and the active material particles represent two pseudo-dimensions, which are coupled by the reaction kinetics. Usually, the Butler-Volmer equation [122] is used, where the resulting flux density depends on the concentrations at the interface between active material and electrolyte, the local potentials, and the OCV. Assuming vanishing gradients in the electrolyte and in the solid phase at the cell level, DFN models can be reduced

to SPMs. This assumption is useful for thin electrodes or slow discharge. In this case, the processes within a single particle are representative of the cell behavior, which allows for a computationally less expensive SPM.

Porous secondary particles for battery electrodes have been modeled by several groups<sup>3</sup>. Combining experiments with 3D imaging and statistical image analysis, Wagner et al. [15] studied structure-property relationships of HSEs. Moreover, Neumann et al. [123] used stochastic nanostructure modeling and numerical simulations to quantitatively investigate effective ionic and electronic transport in secondary active material particles with a designed inner porosity. Wu et al. [124] employed a continuum model of a single secondary particle concentrating on intercalation-induced stresses. Cernak et al. [125] spatially resolved the secondary particle to investigate the effect of secondary particle porosity on the cell performance. Lüth et al. [126] developed a continuum cell model for electrodes that consist of secondary particles possessing a certain inner porosity due to their agglomerate character. With this model, they studied the dependence of cell performance on two morphological and two material properties. Namely, they considered the effects of the electrochemically active surface area, the secondary particle porosity, the diffusivity in the active material, and the electronic conductivity of the active material. Birkholz et al. [16] applied a similar model to HSEs with designed inner porosity of the secondary particles. They quantified the influence of diffusivity in the active material and electronic conductivity of the active material on the rate capability of the cell.

Multiple methods are available to model transport through a hierarchy of pores<sup>4</sup>. A widely used approach is pore network models [127], which simplify a porous medium to a network of pore bodies and pore throats of different sizes capturing the relevant features of the transport. Meyers et al. [128, 129] developed a

<sup>3</sup> This paragraph has previously been published in Naumann et al. (2023) [1] . The text has been modified.

<sup>4</sup> This paragraph has previously been published in Naumann et al. (2024) [2] . The text has been modified.

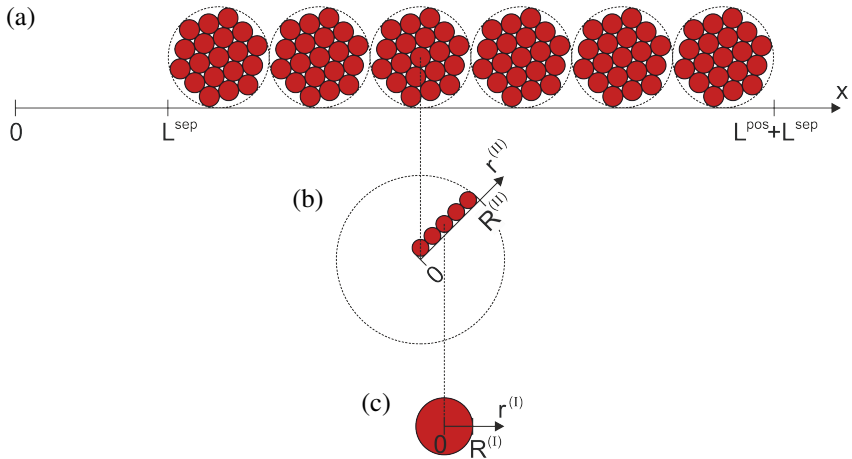
pore network model to study columns packed with chromatographic porous particles. Sadeghi et al. [130] investigated the reactive transport in a hierarchically porous catalyst with a pore network model. More detailed models resolve the hierarchical structure spatially. Examples include modeling reactive transport in micro-/mesoporous materials with added macropores by the lattice Boltzmann method [131], dynamic Monte Carlo simulations of mass transfer in a network of mesopores within a microporous continuum [132, 133], or molecular simulation of transport in different hierarchically porous structures under a pressure gradient [134]. Tallarek et al. [135] combined molecular dynamics with Brownian dynamics to derive effective diffusion coefficients in hierarchically structured materials. Gritti et al. [136, 137] compared and developed several models for macroscopic sample diffusion in chromatographic columns filled with porous particles as well as porous shells around compact particles. However, these approaches require time-consuming model building or numerically expensive simulations. In contrast, explicit formulas for the effective transport through hierarchically porous structures allow easy integration in multiphysics models. Combining the Maxwell equation and conductivity measurements, Barrande et al. [138] developed an explicit expression for the tortuosity of a suspension of porous particles. Yet, this expression lacks the possibility to include additional impermeable phases like carbon additive or binder, which are used in battery electrodes.



# 3 Modeling Hierarchically Structured Electrodes

## 3.1 Hierarchically Structured Cell Model

To study the electrochemical processes that take place in hierarchically structured electrodes (HSEs) during discharge, I use a model developed by Birkholz et al. [16]. It builds on Doyle-Fuller Newman (DFN) models (Chapter 2.5).



**Figure 3.1:** Schematic of the hierarchically structured half-cell model. (a) Half-cell level (coordinate  $x$ ), (b) secondary particle level (coordinate  $r^{(II)}$ ), and (c) primary particle level (coordinate  $r^{(I)}$ ).

Both models employ the porous electrode theory [59, 119, 120]. Birkholz et al. [16] extended the DFN model to describe HSEs (hierarchically structured half-cell model, HSCM). For this purpose, they defined three pseudo-dimensions: the half-cell (Fig. 3.1a), the secondary particles (Fig. 3.1b), and the primary particles (Fig. 3.1c). Half-cell and secondary particles are viewed as continua, whereas the primary particles are spatially resolved in the model. Furthermore, the model assumes primary particles as well as secondary particles to be spherically symmetric.

At the half-cell level, the single components, i.e. secondary particles, electrolyte, and additive, are not spatially resolved. Instead, they exist at every position in the electrode continuum according to their volume fractions  $\varepsilon$ . Similarly, the components of the secondary particles are represented by their volume fractions in the spherically symmetric secondary particle continua. Each secondary particle continuum behaves like a representative secondary particle at the respective position in the electrode. It experiences surface conditions that are present at this position within the intergranular electrolyte and within the solid phase of the electrode. In the same manner, each model primary particle experiences representative conditions according to its position within the secondary particles.

The HSCM incorporates the following electrochemical processes:

- ionic mass and charge transport via the electrolyte both at half-cell level (Eq. 3.9 and 3.10) and within the secondary particles (Eq. 3.16 and 3.17),
- electronic transport in the solid phase both at half-cell level (Eq. 3.3) and within the secondary particles (Eq. 3.18)
- electrochemical intercalation reaction at the primary particle surfaces (Eq. 3.19),
- diffusion of the intercalated ions in the active material (Eq. 3.22).

In the following, the partial differential equations and the boundary conditions describing the above-mentioned processes are introduced. My description covers the discharge process of a half-cell. For a charge scenario, all processes reverse.

During an  $nC$  discharge (Chapter 2.2, compare Eq. 2.3) of a half-cell, a constant current density of

$$i_{\text{app}} = n \frac{L^{\text{pos}} \varepsilon_s^{\text{pos}} \varepsilon_s^{(\text{II})} F (c_{s,\text{max}} - c_{s,0})}{3600 \text{ s}} \quad (3.1)$$

is extracted. The  $nC$ -current may be calculated using the thickness of the positive electrode  $L^{\text{pos}}$ , the volume fraction of secondary particles in the electrode  $\varepsilon_s^{\text{pos}}$ , the volume fraction of active material in the secondary particles  $\varepsilon_s^{(\text{II})}$ , Faraday's constant  $F$ , the maximum concentration of the intercalated species in the active material  $c_{s,\text{max}}$ , and the initial concentration in the active material  $c_{s,0}$ . The current density leaves the cell at the positive electrode current collector

$$\sigma_{\text{eff}} \frac{\partial \bar{\phi}_s}{\partial x} \bigg|_{x=L^{\text{sep}}+L^{\text{pos}}} = -i_{\text{app}}. \quad (3.2)$$

The through-thickness coordinate  $x$  (Fig. 3.1a) runs from the negative electrode at  $x = 0$  across the separator of length  $L^{\text{sep}}$  and the positive electrode to the current collector. The electric potential  $\bar{\phi}_s$  is a continuum variable, which is influenced by the effective electronic conductivity (Chapter 3.2) of the additives  $\sigma_{\text{eff}}$ . The electronic transport through the positive electrode is modeled via

$$\frac{\partial}{\partial x} \left( \sigma_{\text{eff}} \frac{\partial \bar{\phi}_s}{\partial x} \right) = -\varepsilon_s^{\text{pos}} \bar{j}_c. \quad (3.3)$$

This charge conservation equation contains electronic conduction and a sink term  $\varepsilon_s^{\text{pos}} \bar{j}_c$  due to electrons entering the secondary particles. Simultaneous with the electronic transport, there is an ion influx from the negative electrode into the separator

$$D_{\text{e,eff}}^{\text{sep}} \frac{\partial \bar{c}_e}{\partial x} \bigg|_{x=0} = -i_{\text{app}} \frac{1-t_+}{F}, \quad (3.4)$$

which affects the concentration of shuttling ions in the electrolyte  $\bar{c}_e$ , another continuum variable of the model. Here,  $D_{\text{e,eff}}^{\text{sep}}$  denotes the effective diffusivity

(Chapter 3.2) of the electrolyte in the separator and  $t_+$  is the transference number of the ions. In a half-cell, the magnitude of the ion influx directly corresponds to the applied current density  $i_{\text{app}}$ , maintaining the electroneutrality of the system. The ions move through the electrolyte of volume fraction  $\varepsilon_e^{\text{sep}}$  in the separator

$$\varepsilon_e^{\text{sep}} \frac{\partial \bar{c}_e}{\partial t} = \frac{\partial}{\partial x} \left( D_{e,\text{eff}}^{\text{sep}} \frac{\partial \bar{c}_e}{\partial x} \right), \quad (3.5)$$

$$\frac{\partial}{\partial x} \left( \kappa_{\text{eff}}^{\text{sep}} \frac{\partial \bar{\phi}_e}{\partial x} + \kappa_{D,\text{eff}}^{\text{sep}} \frac{\partial \ln \bar{c}_e}{\partial x} \right) = 0. \quad (3.6)$$

Eq. 3.5 ensures the conservation of mass during the diffusion of ions in the electrolyte. Eq. 3.6 guarantees conservation of charge. It expresses the conduction of ions according to the effective conductivity (Chapter 3.2) of the electrolyte in the separator  $\kappa_{\text{eff}}^{\text{sep}}$ . In addition, it includes a coupling term according to the effective diffusional conductivity  $\kappa_{D,\text{eff}}^{\text{sep}}$ . This ensures consistency between concentration  $\bar{c}_e$  and electrochemical potential  $\bar{\phi}_e$  in the electrolyte, which are both continuum variables. At the interface of the separator and the electrode, the ion flux is continuous with

$$D_{e,\text{eff}}^{\text{sep}} \frac{\partial \bar{c}_e}{\partial x} \bigg|_{x=L^{\text{sep}}} = D_{e,\text{eff}} \frac{\partial \bar{c}_e}{\partial x} \bigg|_{x=L^{\text{sep}}}, \quad (3.7)$$

$$\left( \kappa_{\text{eff}}^{\text{sep}} \frac{\partial \bar{\phi}_e}{\partial x} + \kappa_{D,\text{eff}}^{\text{sep}} \frac{\partial \ln \bar{c}_e}{\partial x} \right) \bigg|_{x=L^{\text{sep}}} = \left( \kappa_{\text{eff}} \frac{\partial \bar{\phi}_e}{\partial x} + \kappa_{D,\text{eff}} \frac{\partial \ln \bar{c}_e}{\partial x} \right) \bigg|_{x=L^{\text{sep}}}. \quad (3.8)$$

$D_{e,\text{eff}}$ ,  $\kappa_{\text{eff}}$ , and  $\kappa_{D,\text{eff}}$  are the effective diffusivity, conductivity, and diffusional conductivity of the electrolyte in the electrode. The ions travel through the positive electrode due to diffusion and conduction according to

$$\varepsilon_e^{\text{pos}} \frac{\partial \bar{c}_e}{\partial t} = \frac{\partial}{\partial x} \left( D_{e,\text{eff}} \frac{\partial \bar{c}_e}{\partial x} \right) - \varepsilon_s^{\text{pos}} \bar{j}_m, \quad (3.9)$$

$$\frac{\partial}{\partial x} \left( \kappa_{\text{eff}} \frac{\partial \bar{\phi}_e}{\partial x} + \kappa_{\text{D,eff}} \frac{\partial \ln \bar{c}_e}{\partial x} \right) = \epsilon_s^{\text{pos}} \bar{j}_c. \quad (3.10)$$

The sinks

$$\epsilon_s^{\text{pos}} \bar{j}_c = \frac{3\epsilon_s^{\text{pos}}}{(R^{(\text{II})})^3} \int_0^{R^{(\text{II})}} \left( r^{(\text{II})} \right)^2 a_s^{(\text{I})} \bar{j}^{(\text{I})} F \mathrm{d}r^{(\text{II})}, \quad (3.11)$$

$$\epsilon_s^{\text{pos}} \bar{j}_m = \frac{3\epsilon_s^{\text{pos}}}{(R^{(\text{II})})^3} \int_0^{R^{(\text{II})}} \left[ \left( r^{(\text{II})} \right)^2 \epsilon_e^{(\text{II})} \frac{\partial \bar{c}_e^{(\text{II})}}{\partial t} + \left( r^{(\text{II})} \right)^2 a_s^{(\text{I})} (1 - t_+) \bar{j}^{(\text{I})} \right] \mathrm{d}r^{(\text{II})} \quad (3.12)$$

represent the transport of ions into the secondary particles.

The continuity between cell level and secondary particle level demands at each position  $x$  of the electrode that potentials  $\bar{\phi}_s^{(\text{II})}$  and  $\bar{\phi}_e^{(\text{II})}$  as well as concentration  $\bar{c}_e^{(\text{II})}$  at the secondary particle surfaces corresponds to the same quantities at cell level

$$\bar{\phi}_s^{(\text{II})} \Big|_{r^{(\text{II})}=R^{(\text{II})}} = \bar{\phi}_s, \quad (3.13)$$

$$\bar{\phi}_e^{(\text{II})} \Big|_{r^{(\text{II})}=R^{(\text{II})}} = \bar{\phi}_e, \quad (3.14)$$

$$\bar{c}_e^{(\text{II})} \Big|_{r^{(\text{II})}=R^{(\text{II})}} = \bar{c}_e. \quad (3.15)$$

Within the secondary particles of radius  $R^{(\text{II})}$  and spherical coordinate  $r^{(\text{II})}$  (Fig. 3.1b), the electronic and ionic transport are analogous to the cell level

$$\epsilon_e^{(\text{II})} \frac{\partial \bar{c}_e^{(\text{II})}}{\partial t} = \frac{1}{(r^{(\text{II})})^2} \frac{\partial}{\partial r^{(\text{II})}} \left( \left( r^{(\text{II})} \right)^2 D_{\text{e,eff}}^{(\text{II})} \frac{\partial \bar{c}_e^{(\text{II})}}{\partial r^{(\text{II})}} \right) - a_s^{(\text{I})} (1 - t_+) \bar{j}^{(\text{I})}, \quad (3.16)$$

$$\frac{1}{(r^{(\text{II})})^2} \frac{\partial}{\partial r^{(\text{II})}} \left( (r^{(\text{II})})^2 \kappa_{\text{eff}}^{(\text{II})} \frac{\partial \bar{\phi}_{\text{e}}^{(\text{II})}}{\partial r^{(\text{II})}} + (r^{(\text{II})})^2 \kappa_{\text{D,eff}}^{(\text{II})} \frac{\partial \ln \bar{c}_{\text{e}}^{(\text{II})}}{\partial r^{(\text{II})}} \right) = a_{\text{s}}^{(\text{I})} F \bar{j}^{(\text{I})}, \quad (3.17)$$

$$\frac{1}{(r^{(\text{II})})^2} \frac{\partial}{\partial r^{(\text{II})}} \left( (r^{(\text{II})})^2 \sigma_{\text{eff}}^{(\text{II})} \frac{\partial \bar{\phi}_{\text{s}}^{(\text{II})}}{\partial r^{(\text{II})}} \right) = -a_{\text{s}}^{(\text{I})} F \bar{j}^{(\text{I})}. \quad (3.18)$$

Here, all quantities  $X^{(\text{II})}$  are the secondary particle counterparts of the electrode level quantities. Furthermore,  $a_{\text{s}}^{(\text{I})}$  denotes the electrochemically active surface area of the active material, i.e. the interface between primary particles and electrolyte. Ions and electrons move from the secondary particle surfaces toward their centers separately in the electrolyte and the solid. At the primary particle surfaces, they undergo an electrochemical reaction and intercalate. This causes the flux density

$$\bar{j}^{(\text{I})} = k_0 \left( \bar{c}_{\text{e}}^{(\text{II})} \right)^{1-\alpha} \left( c_{\text{s,max}} - c_{\text{s}}^{(\text{I})} \Big|_{r^{(\text{I})}=R^{(\text{I})}} \right)^{1-\alpha} \left( c_{\text{s}}^{(\text{I})} \Big|_{r^{(\text{I})}=R^{(\text{I})}} \right)^{\alpha} \left[ \exp \left( \frac{(1-\alpha)F}{RT} \bar{\eta}^{(\text{II})} \right) - \exp \left( \frac{-\alpha F}{RT} \bar{\eta}^{(\text{II})} \right) \right], \quad (3.19)$$

which has a negative value for intercalation and a positive value for deintercalation by definition. These Butler-Volmer reaction kinetics incorporate reaction rate constant  $k_0$ , charge transfer coefficient  $\alpha$ , gas constant  $R$ , and temperature  $T$ . They also depend on the concentration  $\bar{c}_{\text{e}}^{(\text{II})}$  in the electrolyte contacting the primary particles, the concentration of the intercalated species  $c_{\text{s}}^{(\text{I})}$  at the surface of the primary particles where their spherical coordinate  $r^{(\text{I})}$  (Fig. 3.1c) has the maximum value  $R^{(\text{I})}$ , as well as on the overpotential

$$\bar{\eta}^{(\text{II})} = \bar{\phi}_{\text{s}}^{(\text{II})} - \bar{\phi}_{\text{e}}^{(\text{II})} - U_{\text{OCV}} \left( c_{\text{s}}^{(\text{I})} \Big|_{r^{(\text{I})}=R^{(\text{I})}} \right). \quad (3.20)$$

The intercalated ions enter the primary particles at their surfaces

$$D_s \frac{\partial c_s^{(I)}}{\partial r^{(I)}} \bigg|_{r^{(I)}=R^{(I)}} = \bar{j}^{(I)}, \quad (3.21)$$

causing a change in the concentration variable  $c_s^{(I)}$ . Within the primary particles, the ions are stored and transported by diffusion according to Fick's second law

$$\frac{\partial c_s^{(I)}}{\partial t} = \frac{1}{(r^{(I)})^2} \frac{\partial}{\partial r^{(I)}} \left( D_s (r^{(I)})^2 \frac{\partial c_s^{(I)}}{\partial r^{(I)}} \right) \quad (3.22)$$

with diffusivity of the active material  $D_s$ .

For better readability, the following boundary conditions were not mentioned above. The electronic insulation of the separator is accounted for by

$$\frac{\partial \bar{\phi}_s}{\partial x} \bigg|_{x=L^{\text{sep}}} = 0. \quad (3.23)$$

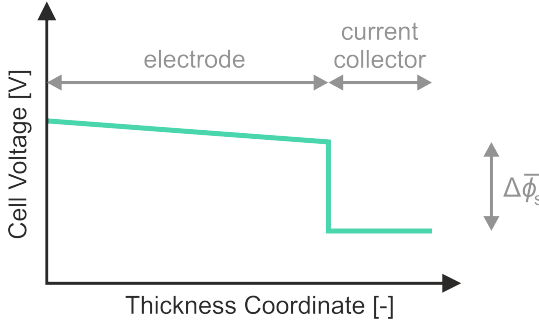
Furthermore, the ionic transport through the electrolyte within the positive electrode stops at the current collector

$$\left( \kappa_{\text{eff}} \frac{\partial \bar{\phi}_e}{\partial x} + \kappa_{D,\text{eff}} \frac{\partial \ln \bar{c}_e}{\partial x} \right) \bigg|_{x=L^{\text{sep}}+L^{\text{pos}}} = 0, \quad (3.24)$$


$$\frac{\partial \bar{c}_e}{\partial x} \bigg|_{x=L^{\text{sep}}+L^{\text{pos}}} = 0. \quad (3.25)$$

Finally, the assumption of spherical symmetry within the secondary and primary particles prohibits gradients at the particle centers

$$\frac{\partial \bar{\phi}_s^{(II)}}{\partial r^{(II)}} \bigg|_{r^{(II)}=0} = 0, \quad (3.26)$$



**Figure 3.2:** Schematic of electric potential over cell thickness with potential drop due to contact resistance between the electrode and the current collector.



This image has previously been published in Naumann et al. (2024) [2] .

$$\left. \frac{\partial \bar{\phi}_e^{(\text{II})}}{\partial r^{(\text{II})}} \right|_{r^{(\text{II})}=0} = 0, \quad (3.27)$$

$$\left. \frac{\partial \bar{c}_e^{(\text{II})}}{\partial r^{(\text{II})}} \right|_{r^{(\text{II})}=0} = 0, \quad (3.28)$$

$$\left. \frac{\partial c_s^{(\text{I})}}{\partial r^{(\text{I})}} \right|_{r^{(\text{I})}=0} = 0. \quad (3.29)$$

I modified the HSCM in four ways<sup>1</sup>. First, I assumed diffusion paths to be longer than the primary particle radius by a factor of 1.5. Schmidt et al. [139] suggested this assumption if part of the active material particle surface is blocked. This is

<sup>1</sup> Parts of this paragraph have previously been published in Naumann et al. (2023) [1]  and Naumann et al. (2024) [2] . The texts have been combined and modified.



the case for HSEs since the primary particles are sintered together. In the following,  $R^{(1)}$  denotes the representative length of the diffusion paths. Second, I developed an explicit formula that realistically predicts the effective ionic transport across hierarchically structured electrodes even at high compaction (Chapter 3.3). Third, I decoupled the electrochemically active surface area of the electrode from other morphological properties by modifying the boundary condition at the primary particle surfaces Eq. 3.21 (Chapter 3.4). Fourth, I additionally accounted for a changing contact resistance between the electrode and the current collector during calendaring [93], which contributed to a decrease in cell resistivity [88]. The contact resistance  $R_{\text{cont}}$  leads to a potential drop

$$\Delta\bar{\phi}_s = R_{\text{cont}}i_{\text{app}} \quad (3.30)$$

at the interface of the electrode and the current collector depending on the applied current  $i_{\text{app}}$ , which affects the acquired cell voltage (Fig. 3.2).

For my modeling studies, I used the HSCM to investigate a hierarchically structured positive electrode in a half-cell setup under galvanostatic discharge until a cut-off voltage of 3.0 V. The corresponding differential equations and boundary conditions were solved in COMSOL Multiphysics by implementing the boundary value problem in the Coefficient Form PDE module.

## 3.2 Effective Transport Properties

The HSCM (Chapter 3.1) has to accurately capture transport phenomena within the electrode, the separator, and the secondary particles. Viewing these model entities as continua causes the loss of structural information since the model does not explicitly capture the morphology of the pore and solid phase. However, a realistic model has to incorporate the effect of morphology on the physical processes within the cell. For this purpose, effective transport properties

$$D_{\text{eff}} = MD \quad (3.31)$$

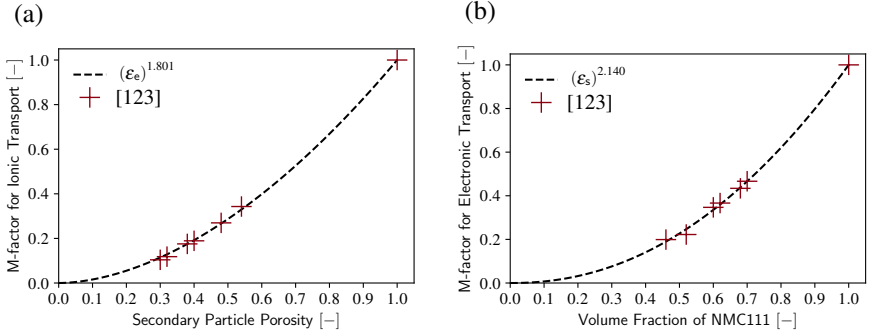
are determined. They employ M-factor  $M$  to capture the effect of morphology on the transport in a material structure with bulk transport property  $D$ . A multitude of methods predict M-factors. One option is experimentally measuring effective transport in porous structures, e.g. by electrochemical impedance spectroscopy (EIS) [140], and comparing it to the bulk transport property. Furthermore, different modeling techniques are available to determine M-factors. Modeling steady-state transport on three-dimensional voxel image data of a microstructure yields the effective transport property [141, 142]. Virtually generated microstructures, which are stochastically equivalent to the real microstructure, may serve as an alternative to direct voxel image data [143]. In the simplest case, electrode microstructures can be represented by a cluster of ellipsoids [144] or spheres [145]. The numerically inexpensive Resistor Network (RN) Method can then extract the M-factor [144, 145]. Different fit formulas have been deduced from modeling results. Elaborate formulas may depend on a multitude of morphological properties, e.g. volume fraction, tortuosity, overlap of particles, particle size distribution, surface area of pore walls, and bottleneck effects [146, 147]. A widely used fit formula is the Bruggeman relation [148, 149]


$$M = \varepsilon^{1.5} \quad (3.32)$$

for random porous media of spherical particles with volume fraction  $\varepsilon$ .

Regarding the investigations of hierarchically structured NMC electrodes in this work (Chapter 4 and 5), fit formulas for the M-factors at the electrode level are available. Birkholz et al. [147, 150] obtained a fit formula for the M-factor of the intergranular pore space of volume fraction  $\varepsilon_e^{\text{pos}} + \varepsilon_f^{\text{pos}}$ . For this purpose, they applied a Bruggeman-type fit to RN data of virtual sphere assemblies with varying properties. Then, they employed an additive split of the pore space between the electrolyte of volume fraction  $\varepsilon_e^{\text{pos}}$  and the additives of volume fraction  $\varepsilon_f^{\text{pos}}$ , which carry the effective ionic and electronic transport, respectively. This yields M-factor

$$M_{\text{ion}}^{\text{pos}} = (\varepsilon_e^{\text{pos}} + \varepsilon_f^{\text{pos}})^{1.342} \frac{\varepsilon_e^{\text{pos}}}{\varepsilon_e^{\text{pos}} + \varepsilon_f^{\text{pos}}} = (\varepsilon_e^{\text{pos}} + \varepsilon_f^{\text{pos}})^{0.342} \varepsilon_e^{\text{pos}} \quad (3.33)$$



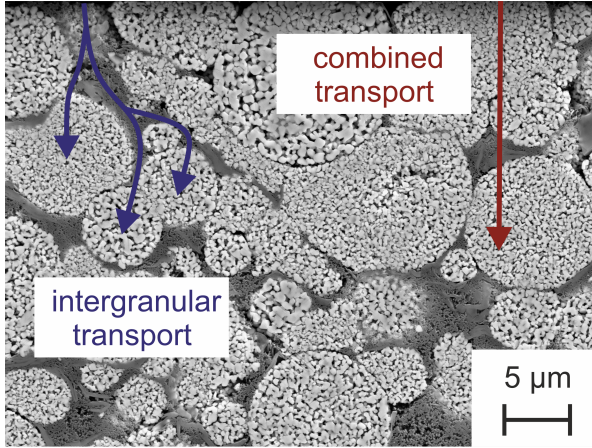
**Figure 3.3:** Fit of M-factor for (a) ionic and (b) electronic transport in the secondary particles. The images have previously been published in Naumann et al. (2023) [1] .

for the effective ionic transport in the intergranular pore space. Since the electronic conductivity of the additives often is significantly larger than the electronic conductivity of the active material, the latter can be neglected in this case. With this assumption, the M-factor for the effective electronic conductivity in the electrode is


$$M_{\text{con}}^{\text{pos}} = (\epsilon_e^{\text{pos}} + \epsilon_f^{\text{pos}})^{1.342} \frac{\epsilon_f^{\text{pos}}}{\epsilon_e^{\text{pos}} + \epsilon_f^{\text{pos}}} = (\epsilon_e^{\text{pos}} + \epsilon_f^{\text{pos}})^{0.342} \epsilon_f^{\text{pos}}. \quad (3.34)$$

M-factors for ionic and electronic transport within the secondary particles are available from Neumann et al. [123]. They virtually reconstructed the inner morphology of different porous secondary NMC particles and obtained M-factors by finite element (FE) simulations. The M-factor  $M_{\text{ion}}^{(\text{II})}$  for ionic transport showed a power-law dependence on the volume fraction of electrolyte  $\epsilon_e^{(\text{II})}$  (Fig. 3.3a). Similarly, the M-factor  $M_{\text{con}}^{(\text{II})}$  for electronic transport depended on the volume fraction of active material  $\epsilon_s^{(\text{II})}$  (Fig. 3.3b). Similar to the fit formulas by Birkholz et al., I chose a Bruggeman-type fit

$$M = \epsilon^\beta \quad (3.35)$$



**Figure 3.4:** Schematic of possible ionic transport paths across the electrode thickness: Main ionic transport through intergranular pores (intergranular transport) or significant contribution by intragranular pores (combined transport).

This image has previously been published in Naumann et al. (2024) [2] 

with respective volume fraction  $\varepsilon$  and fitting parameter  $\beta$ . By minimizing the root mean square error, I obtained the M-factors

$$M_{\text{ion}}^{(\text{II})} = \left( \varepsilon_{\text{e}}^{(\text{II})} \right)^{1.801}, \quad (3.36)$$

$$M_{\text{eon}}^{(\text{II})} = \left( \varepsilon_{\text{s}}^{(\text{II})} \right)^{2.140} \quad (3.37)$$

for ionic and electronic transport in the secondary particles (Fig. 3.3).

### 3.3 Ionic Transport in Hierarchically Structured Electrodes


The original HSCM assumes effective ionic transport from the separator to the current collector in the intergranular pores of the electrode (Fig. 3.4, intergranular transport) in the form

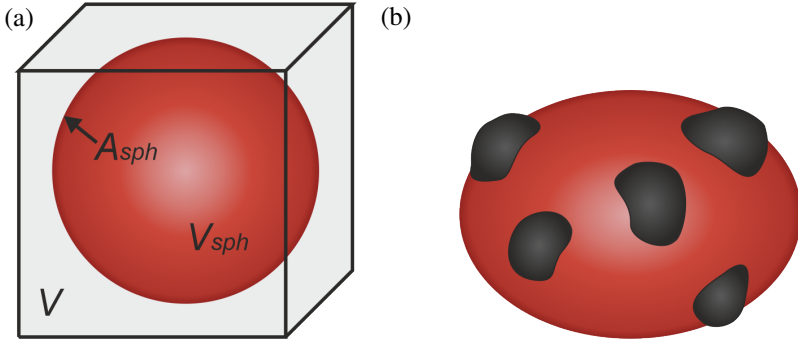
$$D_{\text{eff}} = M_{\text{ion}}^{\text{pos}} D \quad (3.38)$$

with M-factor  $M_{\text{ion}}^{\text{pos}}$ , which reduces the bulk property  $D$  according to the intergranular pore network<sup>2</sup>. This purely intergranular transport occurs when all of the ions entering the porous particles are consumed by the electrochemical intercalation reaction on the way inside. If the ionic current exceeds this amount, part of the ions will travel through the particles and contribute to the overall ionic current from the separator to the current collector. This additional transport path will decrease the ionic resistance of the electrode compared to compact particles. Therefore, I deduced the M-factor for parallel transport through the porous particles and through the intergranular pores (Fig. 3.4, combined transport),

$$D_{\text{eff}} = M_{\text{ion}}^{\text{combi}} D = (M_{\text{ion}}^{\text{pos}} + M_{\text{ion}}^{\text{intra}}) D \quad (3.39)$$

with M-factor  $M_{\text{ion}}^{\text{combi}}$  for a combined intra- plus intergranular ionic transport. The partial M-factor  $M_{\text{ion}}^{\text{intra}}$  describes the effective ionic transport through the network of porous particles, which depends on two factors. First, the intragranular porosity possesses an intrinsic tortuosity described by M-factor  $M_{\text{ion}}^{(\text{II})}$ . Due to the small intragranular pore size,  $M_{\text{ion}}^{(\text{II})}$  is lower than  $M_{\text{ion}}^{\text{pos}}$  at the same porosity (compare Eq. 3.33 and 3.36). Second, bottlenecks at the contact regions of two porous particles will further reduce the effective ionic transport through the

<sup>2</sup> This chapter has previously been published in Naumann et al. (2024) [2] . The text has been modified.



**Figure 3.5:** (a) Spherical particle inside a unit cell. (b) Oval particle with partially blocked surface.

particle network. The M-factor of interconnected spherical particles of the same size follows the fit formula [147]

$$M^{\text{particles}} = (\epsilon_s^{\text{pos}} - 0.62)^{0.8015 + \frac{0.3227}{\theta} - \frac{13.88}{47.37 - \theta}} \quad (3.40)$$

with volume fraction  $\epsilon_s^{\text{pos}}$  of the particles and percolation threshold 0.62. The mean contact angle  $\theta$  can be calculated via the fit formula [147]

$$\theta = \frac{\ln\left(\frac{15.625}{1 - \epsilon_s^{\text{pos}}} - 43.277\right)}{0.166}. \quad (3.41)$$

For  $\theta < 0$ ,  $M^{\text{particles}}$  is set to zero since there is no percolation among the particles. Combining all partial M-factors yields the overall M-factor for intra- plus intergranular transport

$$M_{\text{ion}}^{\text{combi}} = M_{\text{ion}}^{\text{pos}} + M^{\text{particles}} M_{\text{ion}}^{(\text{II})}. \quad (3.42)$$

### 3.4 Electrochemically Active Surface Area

In DFN cell models (Chapter 2.5), the electrochemically active surface area  $a_s$  has to comply with the volume fraction of the solid phase  $\varepsilon_s$  as well as the particle radius  $R_p$  [109]. The models assume ideal spherically symmetric particles. Picture one particle of volume  $V_{\text{sph}}$  and surface area  $A_{\text{sph}}$  inside the unit cell of volume  $V$  (Fig. 3.5a). The volume fraction of the spherical particle is

$$\begin{aligned} \varepsilon_s &= \frac{V_{\text{sph}}}{V} = \frac{\frac{4}{3}\pi R_p^3}{V} \\ \iff V &= \frac{4}{3} \frac{\pi R_p^3}{\varepsilon_s}. \end{aligned} \quad (3.43)$$

The electrochemically active surface area results in

$$a_{\text{sph}} = \frac{A_{\text{sph}}}{V} = \frac{4\pi R_p^2}{\frac{4}{3} \frac{\pi R_p^3}{\varepsilon_s}} = \frac{3\varepsilon_s}{R_p}. \quad (3.44)$$

This relationship is an inherent property of the model.

In reality, it is possible that Eq. 3.44 is not fulfilled. This may be caused by non-spherical particle shapes or if parts of the particle surfaces are blocked by other phases (Fig. 3.5b). Let us assume active material particles of volume  $V_s$  and accessible surface area  $A_s$ . This results in the electrochemically active surface area

$$a_s = \frac{A_s}{V} = p \frac{3\varepsilon_s}{R_p}. \quad (3.45)$$

The newly introduced factor  $p$  describes the deviation of the electrochemically active surface area from Eq. 3.44.

In the following, I derive how the factor  $p$  enters DFN cell models. The volume-averaged temporal change in solid phase concentration at an arbitrary position

results solely from the mass flux  $\bar{j}$  across the solid's surface due to the electrochemical reaction

$$\frac{1}{V} \int_{V_s} \frac{\partial c_s}{\partial t} dV = \frac{1}{V} \int_{A_s} \bar{j} dA = \bar{j} \frac{A_s}{V} = \bar{j} a_s. \quad (3.46)$$

DFN models assume  $\bar{j}$  to be homogeneous on the surface of the model particles. For these idealized spherical particles, the volume-averaged temporal change in concentration can be deduced from the solid diffusion equation in the primary particles (compare Eq. 3.22) as

$$\begin{aligned} \frac{1}{V} \int_{V_s} \frac{\partial c_s}{\partial t} dV &= \frac{1}{V} \int_{V_{\text{sph}}} \frac{\partial c_s}{\partial t} dV \\ &= \frac{3}{4} \frac{\varepsilon_s}{\pi R_p^3} \int_0^{R_p} 4\pi r^2 \frac{\partial c_s}{\partial t} dr \\ &= \frac{3\varepsilon_s}{R_p^3} \int_0^{R_p} r^2 \frac{\partial c_s}{\partial t} dr \\ &= \frac{3\varepsilon_s}{R_p^3} \int_0^{R_p} r^2 \frac{1}{r^2} \frac{\partial}{\partial r} \left( D_s r^2 \frac{\partial c_s}{\partial r} \right) dr \\ &= \frac{3\varepsilon_s}{R_p^3} \left[ R_p^2 D_s \frac{\partial c_s}{\partial r} \Big|_{r=R_p} - 0^2 D_s \frac{\partial c_s}{\partial r} \Big|_{r=0} \right] \\ &= \frac{3\varepsilon_s}{R_p} D_s \frac{\partial c_s}{\partial r} \Big|_{r=R_p}. \end{aligned} \quad (3.47)$$

Combining Eq. 3.46 and 3.47 yields the boundary condition at the surfaces of the model particles

$$D_s \frac{\partial c_s}{\partial r} \Big|_{r=R_p} = p \bar{j} \quad (3.48)$$

with

$$p = \frac{R_p a_s}{3\varepsilon_s}. \quad (3.49)$$



When the electrochemically active surface area does not comply with Eq. 3.44, the boundary condition at the particle surfaces has to be modified by the  $p$ -factor. The modification can be interpreted as distributing the flux density associated with the actually available electrochemically active surface area  $a_s$  evenly across the surfaces of the model particles.

A similar approach can decouple the electrochemically active surface area in the HSCM. Here,  $a_s^{(I)}$  complies with the primary particle radius  $R^{(I)}$  and the volume fraction of active material in the secondary particles  $\epsilon_s^{(II)}$ . Following the same derivation as before leads to a modification of Eq. 3.21

$$D_s \frac{\partial c_s^{(I)}}{\partial r^{(I)}} \bigg|_{r^{(I)}=R^{(I)}} = p \bar{j}^{(I)} \quad (3.50)$$

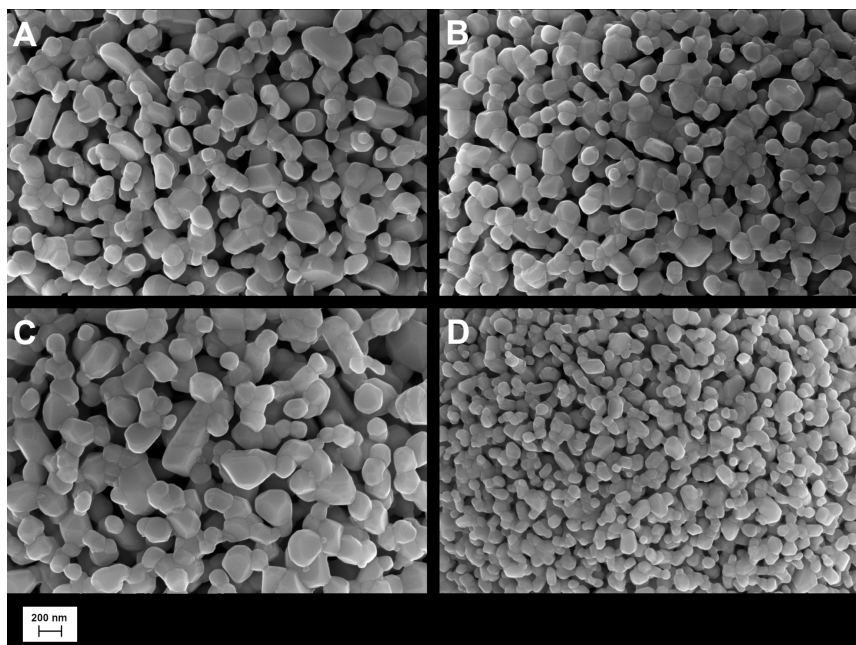
with

$$p = \frac{R^{(I)} a_s^{(I)}}{3 \epsilon_s^{(II)}}. \quad (3.51)$$


In HSEs, primary particles are typically sintered together to form porous secondary particles. Therefore, part of their surface is always blocked, which makes decoupling necessary.

### 3.5 Properties of Hierarchically Structured NMC Electrodes

To study the effects of morphology on the performance of slightly calendered hierarchically structured NMC111 electrodes (Chapter 4), Joachim R. Binder's



**Figure 3.6:** SEM images: NMC111 powders A-D with different secondary particle porosity, electrochemically active surface area, and primary particle size.

Images by Amalia Wagner and Nicole Bohn. The images have previously been published in Naumann et al. (2023) [1] 

group at the Karlsruhe Institute of Technology<sup>3</sup> prepared 8 electrodes of varying properties (Chapter A.1) [1]. Using ball-milling, spray-drying, and sintering, they transformed commercially available NMC111 granules into porous secondary particles (Fig. 3.6). These were used to assemble HSEs, which were investigated in a half-cell setup, i.e. using a lithium-metal negative electrode. By

<sup>3</sup> Dr. Joachim R. Binder, Institute for Applied Materials, Karlsruhe Institute of Technology, 76344 Eggenstein-Leopoldshafen, Germany, joachim.binder@kit.edu.


**Table 3.1:** Powder characteristics of the porous NMC111 materials. Significant differences in powder properties are highlighted in **bold font**.

Measurements by Amalia Wagner and Nicole Bohn. This table has previously been published in Naumann et al. (2023) [1] .

Electrode	Secondary Particle Porosity [-]	Primary Particle Radius [ $\mu\text{m}$ ]	Electrochem. Active Surface Area [ $\text{m}^2 \text{g}^{-1}$ ]	Secondary Particle Radius [ $\mu\text{m}$ ]
A	<b>0.514</b>	0.127	5.1	<b>4.5</b>
B	<b>0.439</b>	0.102	4.9	<b>3.5</b>
C	0.476	<b>0.156</b>	3.6	<b>4.8</b>
D	0.474	<b>0.072</b>	7.4	<b>3.6</b>

altering the production process, they obtained electrodes with different intragranular porosity, primary particle radius, secondary particle radius, and electrode thickness (Tab. 3.1 and 3.2).

As a reference cell, I chose the half-cell with the E1 electrode<sup>4</sup>. Chapter B.1 lists geometric properties (Tab. B.1), material properties (Tab. B.2 and B.3), and effective transport properties (Tab. B.4) of the E1 reference cell. Müller et al. [88] and Schneider et al. [93] investigated similar electrodes, including charge-discharge behavior, incremental capacities (cyclic voltammograms), internal resistances (electrochemical impedance spectroscopy), and aging behavior. To validate the applicability of the HSCM, I compared modeled discharge curves at rates between C/20 and 5C to the experimental results. The model results showed a qualitatively good agreement and captured the general shape of the discharge curves (Fig. 3.7). In addition, the model reproduced the trend of decreasing specific capacity with increasing discharge rate and predicted the specific capacity

<sup>4</sup> This paragraph has previously been published in Naumann et al. (2023) [1] . The text has been modified.

**Table 3.2:** Properties of hierarchically structured electrodes. Significant differences in electrode properties are highlighted in **bold font**. Measurements by Amalia Wagner and Nicole Bohn. This table has previously been published in Naumann et al. (2023) [1] 

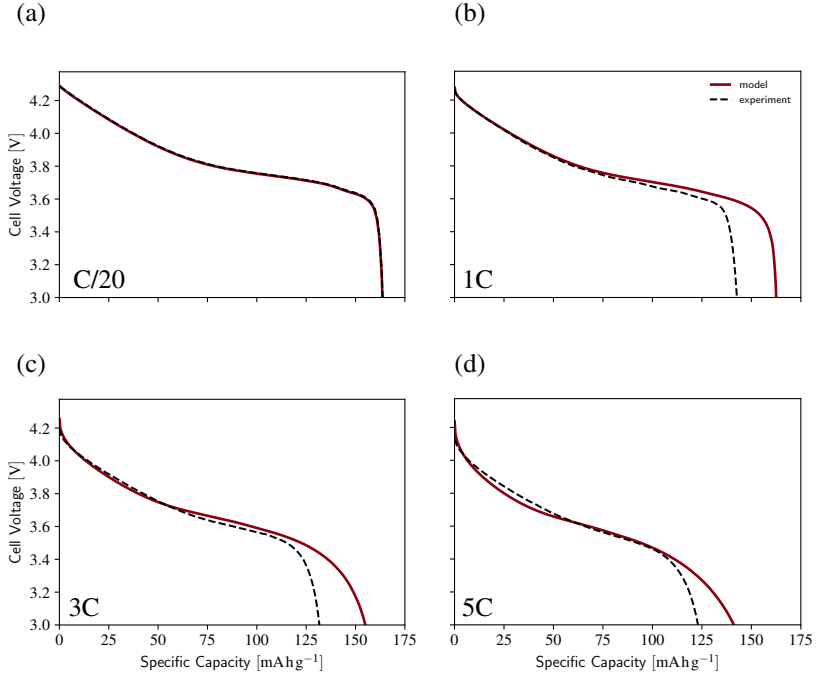
Electrode	Loading [mg cm <sup>-2</sup> ]	Thickness [μm]	Volume		Electrode		Volume
			Fraction NMC111 (w/ internal porosity)	[-]	Porosity (w/o internal porosity)	[-]	Fraction Additives
A <sup>[c]</sup>	7.9	48	0.3470 (0.7141)		0.5253 (0.1582)		0.1277
B <sup>[c]</sup>	7.4	45	0.3609 (0.6433)		0.5064 (0.2240)		0.1327
C <sup>[c]</sup>	7.4	43	0.3548 (0.6771)		0.5147 (0.1924)		0.1305
D <sup>[c]</sup>	8.0	50	0.3354 (0.6377)		0.5412 (0.2389)		0.1234
E1 <sup>[a][c]</sup>	8.2	<b>46</b>	0.3734 (0.5762)		0.4893 (0.2865)		0.1373
E2 <sup>[b][s]</sup>	12.4	<b>73</b>	0.3559 (0.5991)		0.5132 (0.2700)		0.1309
E3 <sup>[b][s]</sup>	18.6	<b>107</b>	0.3650 (0.6145)		0.5007 (0.2512)		0.1343
E4 <sup>[b][s]</sup>	22.3	<b>154</b>	0.3032 (0.5104)		0.5853 (0.3781)		0.1115

[a] Comparable powder to P900 from Wagner et al. [15] was used.


[b] Powder from Dreizler et al. [151] was used.

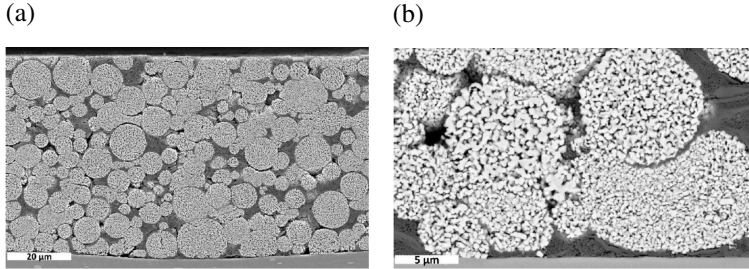
[c] Electrochemical testing was performed using CR2032 coin-type cells.

[s] Electrochemical testing was performed using Swagelok-type cells.



**Figure 3.7:** Comparison of the modeled and experimental discharge behavior of the E1 reference cell at (a) C/20, (b) 1C, (c) 3C, (d) 5C.

Experimental results by Amalia Wagner and Nicole Bohn. The images have previously been published in Naumann et al. (2023) [1] 





**Figure 3.8:** SEM images: Ion-milled cross-sections of electrode Cal-3 [88].  
Images by Marcus Müller and Nicole Bohn.

with an error of  $\leq 11.7\%$ . Therefore, I considered the model appropriate to qualitatively study the E1 reference cell and cells with similar electrodes.

### 3.6 Properties of Calendered Hierarchically Structured NMC Electrodes

To investigate the influence of calendering on the ionic transport (Chapter 5) via the HSCM, I studied HSEs by Müller et al. [88] (Chapter A.2), which were compressed to different porosities<sup>5</sup>. When calendering HSEs (Chapter 2.4) to electrode porosities above 0.3, the intergranular porosity reduces while the particles stay intact [88]. Particles may even undergo plasticity-like deformation without disintegrating. Only after eliminating most of the intergranular porosity, the intragranular porosity decreases with further compaction [93]. Therefore, I assumed that the intragranular porosity  $\epsilon_s^{(II)}$  of all electrodes remains constant at

<sup>5</sup> The following chapter has previously been published in Naumann et al. (2024) [2] . The text has been modified.

**Table 3.3:** Electrode characteristics at different calendaring steps.  
 Measurements by Marcus Müller and Luca Schneider [88, 93].  
 This table has previously been published in Naumann et al. (2024) [2] .

Calendering	Uncalendered	Cal-1	Cal-2	Cal-3
Electrode thickness $L^{\text{pos}}$ [ $\mu\text{m}$ ]	89	69	57	52
Intergranular porosity $\epsilon_e^{\text{pos}}$ [-]	0.435	0.271	0.118	0.032
Volume fraction of porous particles $\epsilon_s^{\text{pos}}$ [-]	0.487	0.628	0.760	0.834
Volume fraction of NMC111 $\epsilon_s^{\text{pos (II)}}$ [-]	0.272	0.351	0.424	0.465
Volume fraction of additives $\epsilon_f^{\text{pos}}$ [-]	0.078	0.101	0.122	0.134
Total porosity $\epsilon_e^{\text{pos}} + \epsilon_s^{\text{pos (II)}}$ [-]	0.650	0.548	0.454	0.401
Contact resistance $R_{\text{cont}}$ [ $\Omega \text{m}^2$ ]	0.006	0.0020	0.0010	0.0008
Total resistivity $R$ [ $\Omega \text{m}$ ]	50	8	5	4

0.442 during calendering, which is the intragranular porosity of the active material powder [88]. From the mass and size of the electrodes as well as the densities of active material and additives, the volume fractions of intergranular pores, porous particles, and additives were calculated (Tab. 3.3). Different magnitudes of calendering led to total electrode porosities of 0.548 (Cal-1), 0.454 (Cal-2), and 0.401 (Cal-3, Fig. 3.8). Chapter B.2 lists geometric properties (Tab. B.5), material properties (Tab. B.6 and B.7), and effective transport properties (Tab. B.8) of the investigated cells. Upon cycling, NMC111 undergoes very little volume change. When lithium atoms intercalate in the crystal structure, the a-lattice expands. At the same time, the c-lattice shrinks due to electrostatic repulsion of the oxygen layers [152]. This anisotropic behavior results in a volume change of no more than 1% [153–155]. Therefore, I assumed that the volume fractions remain constant during cell discharge.

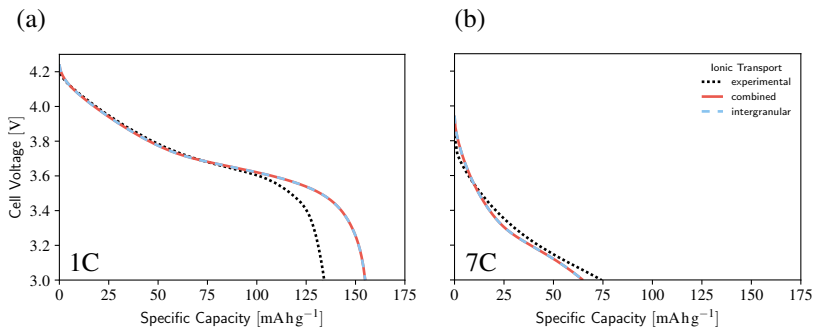
The diffusivity of lithium ions in the considered active material NMC111 changes around 1.5 orders of magnitude depending on the degree of lithiation  $\xi$  [156]. I employed the piecewise fit

$$D_s[\text{m}^2\text{s}^{-1}] = \begin{cases} 10^{-\gamma} & \text{if } \xi \leq 0.5 \\ 10^{-7.5\xi+3.75-\gamma} & \text{if } 0.5 < \xi < 0.7 \\ 10^{-1.5-\gamma} & \text{if } \xi \geq 0.7 \end{cases} \quad (3.52)$$


with fitting parameter  $\gamma$ .

The HSCM (Chapter 3.1) with the purely intergranular assumption (Eq. 3.38) and with the combined intra- plus intergranular assumption (Eq. 3.39) for ionic transport was fitted to experimental discharge curves [88] of the slightly calendered electrode Cal-1 at 1C and 7C (Fig. 3.9). For  $\gamma = 14.4$  (Eq. 3.52) and an active material electronic conductivity of  $\sigma^{(\text{II})} = 3 \cdot 10^{-5} \text{ S m}^{-1}$ , the models yielded similar results to the experiment. The values of the two fitting parameters comply with measurements of the diffusivity [157] and electronic conductivity [140] of NMC111. The models reproduced the beginning of the experimental 1C discharge and the entire 7C discharge curve. However, for the 1C discharge, they





**Figure 3.9:** Comparison between experimental [88] and modeled discharge curves of electrode Cal-1 at (a) 1C and (b) 7C.

These images have previously been published in Naumann et al. (2024) [2] .


overestimated the specific capacity of the cell. Overall, I found the model suitable to describe the electrochemical processes within the studied HSE.



## 4 Influences of Morphology on the Cell Performance of Hierarchically Structured Electrodes

The performance of the cell depends on the morphology of the hierarchically structured electrode (HSE) [15]<sup>1</sup>. Despite first experimental studies, the structure-property relationships in HSEs are not fully understood. Although incorporating the same electrochemical processes as conventional electrode structures, the hierarchical structure affects the interrelation of these processes and additionally requires electronic and ionic transport within the secondary particles. During manufacturing, setting different morphological properties is often interrelated, so separating their influence by individual adjustment remains difficult. Furthermore, experimentally extracting the interplay of morphology and material properties takes great effort. It requires the investigation of a wide range of materials and statistically correlating their inherent characteristics. To complement experimental investigations, porous secondary particles for battery electrodes have been modeled by several groups (Chapter 2.5). However, systematic model-based investigations of the relationship between electrode morphology, material properties, and cell performance across all scales in HSEs have not been performed so far.

---

<sup>1</sup> The following chapter has previously been published in Naumann et al. (2023) [1] . The text has been modified.

Here, I combined a continuum cell modeling framework (Chapter 3) with experimental investigations to show that different processes in the battery cell influence its performance depending on the morphology and material properties of the hierarchically structured positive electrode. I determined the change in rate capability in terms of specific capacity with a variety of morphological features as well as their interplay with material properties. Under different conditions, different physical processes within the cell limit its rate capability. From these findings, I deduced recommendations for the design of HSEs. My investigations extend the work of Birkholz et al. [16, 150] including a refined parameter set (Chapter B.1). My contribution provides a basis for a more intentional development of HSEs.

With my investigations, I aimed to gain insight into the structure-property relationships of HSEs. For this purpose, I separately varied morphological properties and modeled the discharge of the cell at rates ranging from C/20 to 10C. This work includes studies of the electrochemically active surface area, the secondary particle porosity, the secondary particle size, the primary particle size, and the electrode thickness. For each property, I identified the underlying physical processes which explained the observed behavior of the cell. Besides structural parameters, I modified material properties in order to study their interaction with morphology.

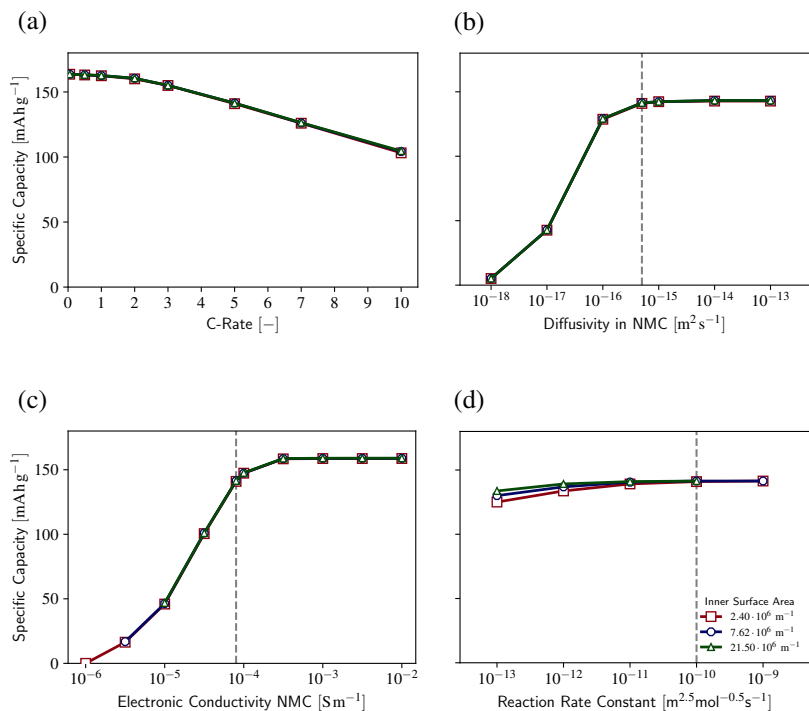
## **4.1 Effect of Electrochemically Active Surface Area on Reaction Kinetics**

The first goal was to quantify the influence of the electrochemically active surface area on the rate capability. Studying this property experimentally is especially difficult since, in reality, the electrochemically active surface area depends on primary and secondary particle size as well as on porosity. The HSCM provides a deeper understanding of these single factors by separating the effect of electrochemically active surface area on the cell performance from the other influencing factors. With a modification of the boundary condition at the primary

particle surfaces (Chapter 3.4), I enabled a variation of the electrochemically active surface area independent from all other electrode properties. In addition to the boundary condition, the electrochemically active surface area affects the source terms of the HSCM (Eq. 3.11, 3.12, 3.16, 3.17, and 3.18), which describe the magnitude of intercalation. The reference electrode E1 (Chapter B.1) had an electrochemically active surface area of  $7.62 \cdot 10^6 \text{ m}^{-1}$ . The investigated range of  $2.40 \cdot 10^6 \text{ m}^{-1}$  ( $0.5 \text{ m}^2 \text{ g}^{-1}$ ) to  $21.50 \cdot 10^6 \text{ m}^{-1}$  ( $4.5 \text{ m}^2 \text{ g}^{-1}$ ) corresponds to typical values observed in experiments [15]. Eq. B.8 gives a conversion of  $\text{m}^{-1}$ , which is required by the HSCM, to  $\text{m}^2 \text{ g}^{-1}$ , which is common in experimental contexts.

The acquired rate capability of cells with electrodes of different electrochemically active surface areas was identical (Fig. 4.1a). Therefore, I find that within the chosen range, the electrochemically active surface area of the electrode has no effect on the cell performance. Lüth et al. [126] found the discharge capacity of agglomerates significantly depends on the electrochemically active surface area of the electrode. Agglomerates have a significantly lower porosity and therefore a lower electrochemically active surface area than secondary particles with a designed inner porosity. Thus, they are limited by the electrochemical reaction at high discharge rates and would benefit from an increased electrochemically active surface area. This can be realized by hierarchically structuring the electrode, which overcomes the reaction limitation by offering electrochemically active surface areas of at least  $2.40 \cdot 10^6 \text{ m}^{-1}$ .

To broaden my results, I studied electrodes with different material properties. Namely, I altered material properties which interdepend with the studied morphological properties, i.e. reaction rate (Eq. 3.19), electronic conductivity of the active material (Eq. 3.18), and diffusivity in the active material (Eq. 3.22). Fig. 4.1b depicts the dependence of cell performance on the active material diffusivity at 5C as an example of a high discharge rate. For a given diffusivity, electrodes with different electrochemically active surface areas yielded identical cell performance. Likewise, varying the electrochemically active surface area



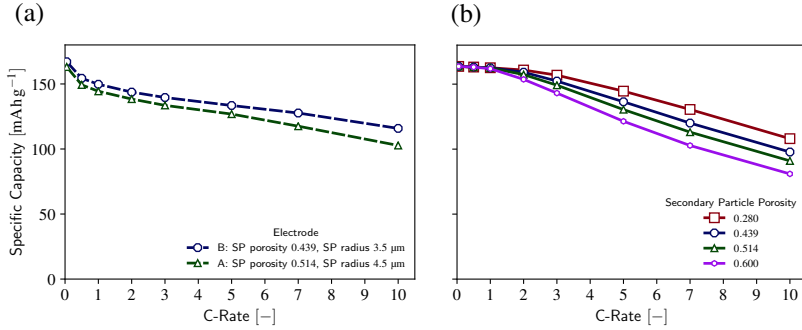
**Figure 4.1:** (a) Rate capability of electrodes with different electrochemically active surface area. (b-d) Influence of (b) diffusivity in the active material, (c) electronic conductivity of the active material, (d) reaction rate on the cell performance at 5C. The vertical line corresponds to the reference electrode E1.

These images have previously been published in Naumann et al. (2023) [1] .

did not affect the influence of the electronic conductivity of the active material on the cell performance (Fig. 4.1c). Only reaction rate constants lower than  $10^{-10} \text{ m}^{2.5} \text{ mol}^{-0.5} \text{ s}^{-1}$  caused a difference in rate capability (Fig. 4.1d). In this case, high surface area electrodes retained a higher specific capacity at 5C because the rate of the electrochemical reaction determined the cell performance. Since the deviation was small even under these extreme conditions, I conclude that hierarchically structured electrodes in general tend to be insensitive to a change in electrochemically active surface area.

## 4.2 Interplay between Secondary Particle Porosity and Electronic Conductivity

Next, I investigated to what extent the cell performance of HSEs depends on the secondary particle porosity. For this purpose, I studied electrodes A and B (Chapter 3.5), which featured differing secondary particle porosity and size but comparable primary particle size. With increasing discharge rate, the specific capacity decreased in experiments (Fig. 4.2a). Furthermore, the capacity fade was more pronounced for electrode A containing more porous and larger secondary particles. The HSCM could separate the two influences. In this chapter, I first investigated the influence of secondary particle porosity on the rate capability. For this purpose, I modeled electrodes of varying secondary particle porosity. At the same time, all other electrode properties complied with the reference electrode E1 (Chapter B.1). The secondary particle porosity enters the HSCM in three ways. It explicitly affects the ionic transport (Eq. 3.16) as well as the effective transport properties (Eq. 3.36 and 3.37) in the secondary particle. Furthermore, it changes the applied current (Eq. 3.1, 3.2, and 3.4) in order to be consistent with the C-rate. The HSCM reproduced the general discharge and rate behavior (Fig. 4.2b). Hence, the modeling results could be used to qualitatively explain the processes during discharge. In addition, the model confirmed the experimental trend with respect to secondary particle porosity. More porous particles provided



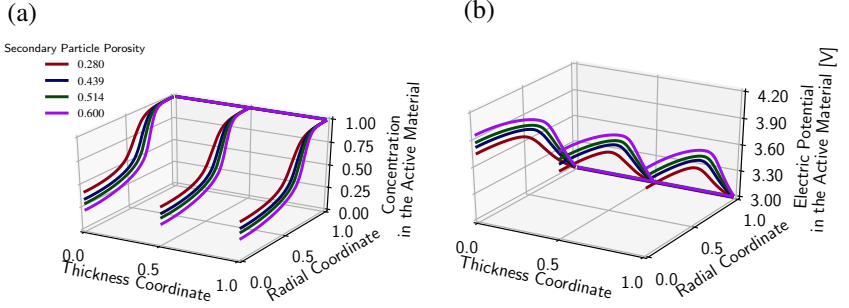
**Figure 4.2:** (a) Experimental rate capability of electrodes A and B (Tab. 3.1 and 3.2) with differing secondary particle porosity and size. (b) Modeled rate capability depending on secondary particle porosity.

Experimental results by Amalia Wagner and Nicole Bohn. These images have previously been published in Naumann et al. (2023) [1] .


a lower rate capability, which explained part of the deviation between electrodes A and B.

The first step to understanding why a high secondary particle porosity yielded a lower rate capability lay in locating the capacity loss within the electrode structure. Fig. 4.3a displays the concentration profile in the active material at the end of a 5C discharge over the electrode thickness and the secondary particle radius. Here, the normalized thickness coordinate runs from 0 at the separator to 1 at the current collector. For the normalized radial coordinate of the secondary particles at the respective thickness position, 0 denotes the particle center and 1 denotes the particle surface. Irrespective of the position within the electrode, the concentration in the active material decreased towards the center of the secondary particles. The concentration gradient intensified if the secondary particles were more porous. Corresponding to the concentration gradient, a gradient in electric potential arose within the active material close to the surface of the secondary particles (Fig. 4.3b). Again, the gradient was aggravated by the increasing porosity of the secondary particles. From this, I deduced that the effective electronic



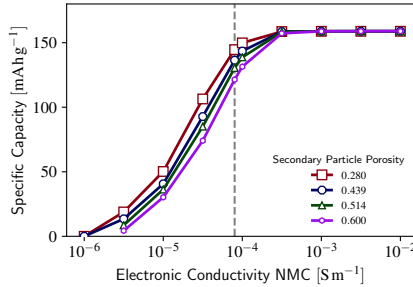


**Figure 4.3:** (a) Normalized concentration in the active material and (b) electric potential in the solid phase at the end of a 5C discharge.


These images have previously been published in Naumann et al. (2023) [1] .

conductivity within the secondary particles limited the cell performance. The low electronic conductivity of NMC111 caused poor exploitation of the active material in primary particles close to the center of secondary particles. As the secondary particle porosity increased, the effective electronic conductivity further declined. In consequence, low secondary particle porosities outperformed high porosities.

A study of cells with varying electronic conductivity of the active material further validated my finding. Amin et al. [158] found that the electronic conductivity of NMC111 varies between  $10^{-6} \text{ S m}^{-1}$  and  $10^0 \text{ S m}^{-1}$  depending on lithiation and temperature. Furthermore, results from Kuo et al. [159] suggested that measuring the electronic conductivity of NMC111 is difficult and includes uncertainties. For this reason, I chose a range of  $10^{-6} \text{ S m}^{-1}$  to  $10^{-2} \text{ S m}^{-1}$  for studying the qualitative influence of electronic conductivity on the cell performance. The cell performance scaled with the electronic conductivity in the range between  $10^{-5.5} \text{ S m}^{-1}$  and  $10^{-4} \text{ S m}^{-1}$  (Fig. 4.4). Above this range, the cell performance reached a limit and other physical processes in the electrode became restrictive. Below  $10^{-5} \text{ S m}^{-1}$ , the specific capacity at 5C declined rapidly. Already at  $10^{-6} \text{ S m}^{-1}$ , the electrode ceased to deliver any capacity. Raising the

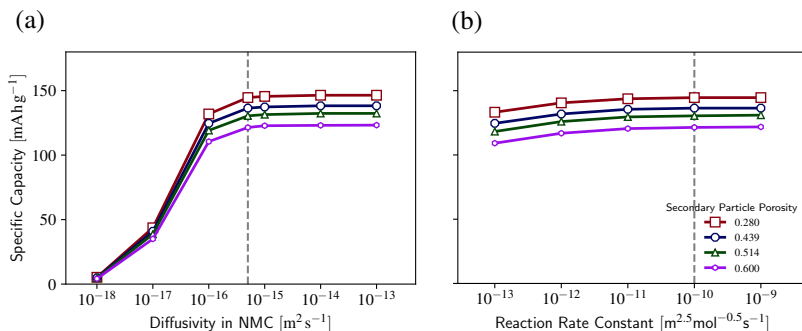


**Figure 4.4:** Influence of electronic conductivity within the secondary particles on the cell performance at 5C. The vertical line corresponds to the reference electrode E1.


This image has previously been published in Naumann et al. (2023) [1] .

electronic conductivity in the secondary particles could enhance the rate capability of the cell, which proves that this material property is crucial for HSEs. If the electronic conductivity of the active material is poor, an enhancement of the overall electronic conductivity in the secondary particles, e.g. by carbon coating of the primary particles, is essential to ensure a good cell performance [160, 161]. My conclusions agreed with Wagner et al. [15], Lüth et al. [126], and Birkholz et al. [16], who identified the electronic conductivity as a main limiting property for the cell performance depending on the electrode morphology.

Other material properties had less influence on the relationship between secondary particle porosity and specific capacity. The specific capacity at 5C hardly changed for active material diffusivities between  $10^{-16} \text{ m}^2 \text{ s}^{-1}$  and  $10^{-13} \text{ m}^2 \text{ s}^{-1}$  (Fig. 4.5a). A diffusivity below  $10^{-16} \text{ m}^2 \text{ s}^{-1}$  caused the difference in cell performance at 5C to decrease. This went hand in hand with an overall drastic decrease of specific capacity for this regime until it completely faded at  $10^{-18} \text{ m}^2 \text{ s}^{-1}$  for all values of secondary particle porosity. When altering the reaction rate constant, the difference induced by secondary particle porosity remained the same (Fig. 4.5b). In summary, a change in the diffusivity of the active material or in the reaction rate constant hardly affected how the secondary particle porosity related to the cell performance.

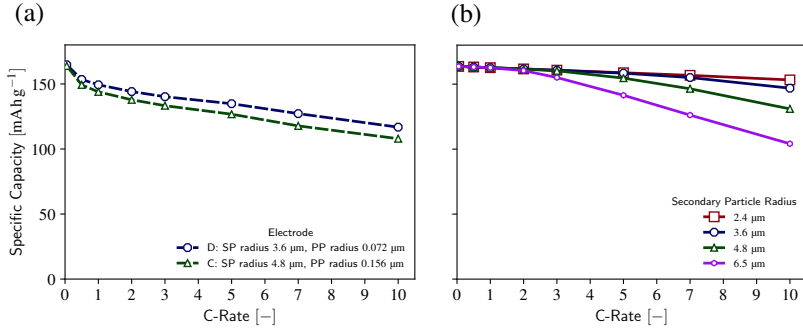


**Figure 4.5:** Influence of (a) diffusivity in the active material and (b) reaction rate on the cell performance at 5C. The vertical line corresponds to the reference electrode E1.

These images have previously been published in Naumann et al. (2023) [1] .

## 4.3 Dependence of Electronic Conductivity on the Secondary Particle Size

In Chapter 4.2, I identified the electronic conductivity within the secondary particles as a limiting factor for the rate capability of HSEs. Naturally, the question arose as to what extent the secondary particle size affects the performance of HSEs. The secondary particle size determines the path lengths of electronic and ionic transport within the secondary particle. The HSCM includes the secondary particle size at the secondary particle level via the range of the radial coordinate  $r^{(II)}$  (Eq. 3.16, 3.17, and 3.18). In addition to a varying secondary particle porosity (Chapter 4.2), the secondary particles of electrodes A and B showed a difference in size (Chapter 3.5). Electrode B with smaller and less porous secondary particles outperformed electrode A in terms of rate capability in experiments (Fig. 4.2a). In addition, I considered electrodes C and D, which differed both in secondary and primary particle size (Chapter 3.5). Electrode D consists of smaller secondary as well as primary particles and showed a higher rate capability in experiments (Fig. 4.6a).

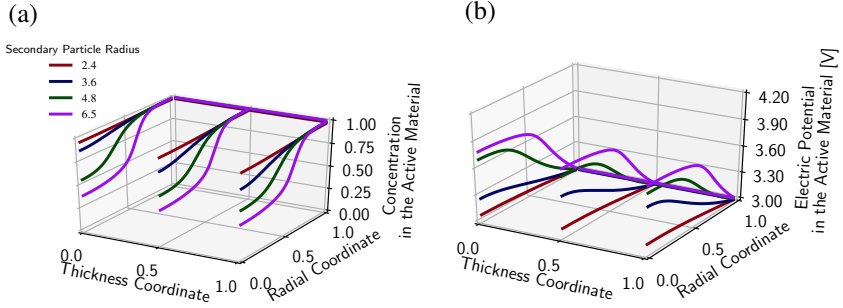


**Figure 4.6:** (a) Experimental rate capability of electrodes C and D (Tab. 3.1 and 3.2) with differing secondary and primary particle size. (b) Modeled rate capability depending on secondary particle size.


Experimental results by Amalia Wagner and Nicole Bohn. These images have previously been published in Naumann et al. (2023) [1] .

Again, the HSCM could elucidate the impact of each single property. This chapter contains modeled results of electrodes with different secondary particle sizes to study their impact, while all other properties corresponded to the reference electrode E1 (Chapter B.1). The rate capability decreased with increasing secondary particle size (Fig. 4.6b). This indicated that the difference in secondary particle size could explain the difference in performance between electrodes A and B as well as between electrodes C and D to some extent. In electrodes A and B, the effects of secondary particle porosity and secondary particle size combined.

The loss in rate capability for larger secondary particles originated from an increased concentration drop over the secondary particle radius (Fig. 4.7a). In the centers of large secondary particles, the active material was used to less of its capacity compared to small particles. The reason again lay in the low electronic conductivity within the secondary particles, as shown by steeper drops in electric potential with increasing secondary particle size (Fig. 4.7b). The long electronic

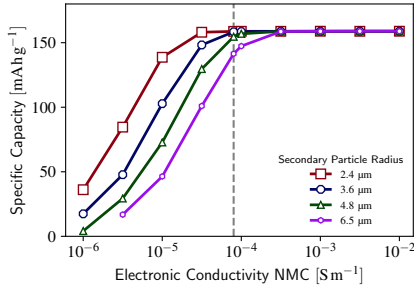


**Figure 4.7:** (a) Normalized concentration in the active material and (b) electric potential in the solid phase at the end of a 5C discharge.


These images have previously been published in Naumann et al. (2023) [1] .

transport paths to the center of large secondary particles impair rate capability if the electronic conductivity of the active material is low.

Investigating electrodes with varying electronic conductivity in the secondary particles confirmed its relation with the secondary particle size (Fig. 4.8). If the electronic conductivity lay between  $10^{-6} \text{ Sm}^{-1}$  and  $10^{-4} \text{ Sm}^{-1}$ , a larger secondary particle size significantly reduced the cell performance at high rates. Increasing the electronic conductivity raised the specific capacity at 5C from less than  $40 \text{ mAh g}^{-1}$  at the lowest electronic conductivity to a maximum of  $159 \text{ mAh g}^{-1}$  at  $10^{-3} \text{ Sm}^{-1}$  or higher. For small secondary particles up to  $4.8 \mu\text{m}$  radius, an electronic conductivity of  $10^{-4} \text{ Sm}^{-1}$  sufficed to ensure an optimal specific capacity. Below this electronic conductivity, the size of the secondary particles significantly governed the rate capability. My findings deviated from Wagner et al. [15], who reported an improved rate capability for large secondary particles. However, the compared electrodes not only differed in secondary particle size but also in secondary particle porosity and electrode porosity. Possibly, the influence of these properties surpassed the influence of the secondary particle size.



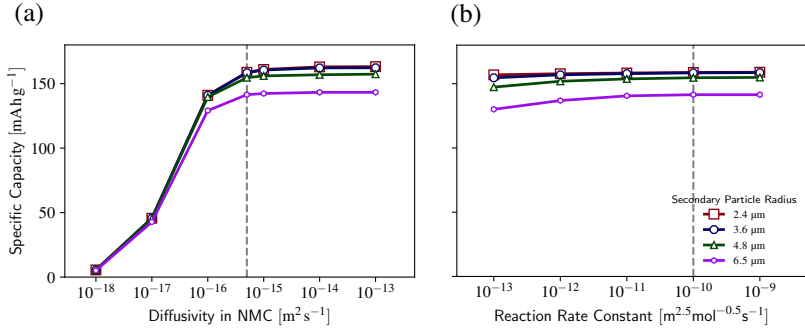
**Figure 4.8:** Influence of electronic conductivity within the secondary particles on the cell performance at 5C. The vertical line corresponds to the reference electrode E1.

This image has previously been published in Naumann et al. (2023) [1] .


Similar to the secondary particle porosity, the secondary particle size played a role if the diffusivity in the active material lay above  $10^{-16} \text{ m}^2 \text{ s}^{-1}$  (Fig. 4.9a). For lower diffusivities, the specific capacity at 5C declined. At the same time, the behavior of electrodes with different secondary particle sizes assimilated. Now the diffusion in the active material limited the cell performance. Therefore the effects of the low electronic conductivity in the secondary particle lost their relevance. The reaction rate constant barely affected the performance of electrodes with different secondary particle sizes (Fig. 4.9b).

## 4.4 Limitations Due to Primary Particle Size and Solid Diffusion

In Chapter 4.3, I showed that a difference in secondary particle size caused the rate capability of electrodes C and D (Chapter 3.5) to diverge. Since these electrodes also differed in primary particle size, I now studied its influence with the HSCM. The primary particle size determines the length of diffusion paths within the active material, i.e. the range of the radial coordinate  $r^{(1)}$  (Eq. 3.22). Note that after studying the electrochemically active surface area separately (Chapter 4.1), in this chapter the electrochemically active surface area changed according to

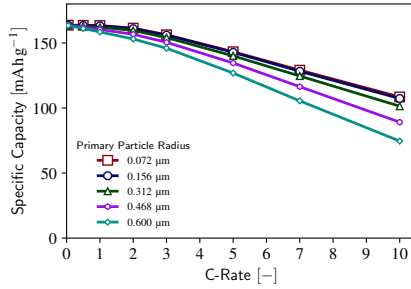


**Figure 4.9:** Influence of (a) diffusivity in the active material and (b) reaction rate on the cell performance at 5C. The vertical line corresponds to the reference electrode E1.


These images have previously been published in Naumann et al. (2023) [1] .

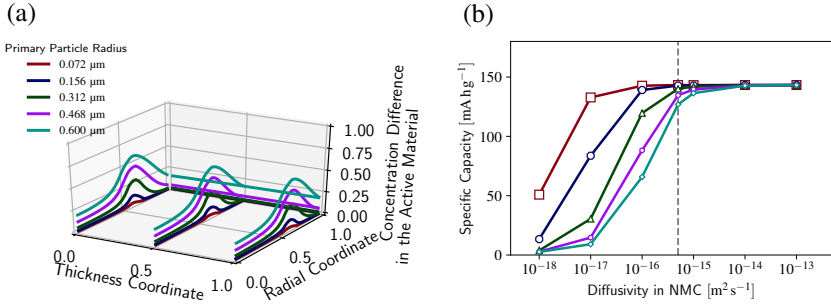
the primary particle size. The model (Fig. 4.10) yielded a lower rate capability for large primary particles. However, the model predicted barely any difference between primary particle radii of 0.072 μm and 0.156 μm, which corresponded to electrodes C and D (Fig. 4.6a). I conclude that the diverging secondary particle size accounted for almost all of the performance alteration between the two electrodes, while the primary particle size only contributed a small additional deviation. The primary particle size plays a role in determining the rate capability of HSEs if the radius exceeds around 0.300 μm.

The loss in rate capability due to a large primary particle size could be attributed to concentration drops inside the primary particles. Fig. 4.11a depicts the difference in concentration between primary particle surfaces and centers. The increased difference for large primary particles in one specific region of the secondary particles indicated larger concentration drops due to diffusion limitations in the active material. This region lay close enough to the secondary particle surface such that it did not suffer from the poor electronic conductivity in the secondary particles. In the center of the secondary particles, the electronic conductivity limited the intercalation, so that the concentration was low, independent of the primary particle size.




**Figure 4.10:** Modeled rate capability depending on primary particle size.

This image has previously been published in Naumann et al. (2023) [1] .



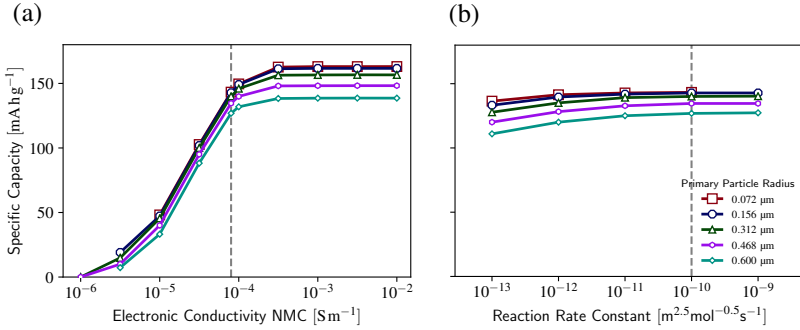
**Figure 4.11:** (a) Difference in normalized concentration in the active material between primary particle surfaces and centers at the end of a 5C discharge. The magnitude in concentration difference indicates the magnitude in concentration drop from the surface to the center of primary particles at each position in the electrode. (b) Influence of diffusivity in the active material on the cell performance at 5C. The vertical line corresponds to the reference electrode E1.


These images have previously been published in Naumann et al. (2023) [1] .



Studies of electrodes with different diffusivity of the active material (Fig. 4.11b) further confirm my explanation. Electrodes containing small primary particles with a radius of  $0.072\ \mu\text{m}$  remained close to the maximum performance until a diffusivity as low as  $10^{-17}\ \text{m}^2\text{s}^{-1}$ . With increasing primary particle size, the specific capacity already started dropping at higher diffusivity. At  $10^{-18}\ \text{m}^2\text{s}^{-1}$ , electrodes with primary particle radii above  $0.156\ \mu\text{m}$  failed completely. From this, it follows that the diffusion in the active material can restrain the cell performance of HSEs. Small primary particles therefore achieve the best exploitation of the active material and take full advantage of the reduced diffusion paths in HSEs. In contrast to my conclusion, Birkholz et al. [16] found the cell performance to be entirely independent of the diffusivity. In comparison, I used a refined value for the diffusivity in the active material and considered diffusion paths longer than the primary particle radius. With my more realistic approach, I could show that an impact of the primary particle size is possible even in HSEs.

The effect of the primary particle size intensified in magnitude after increasing the electronic conductivity of the active material (Fig. 4.12a). At  $10^{-3}\ \text{S m}^{-1}$  and higher, the absolute value of the specific capacity at 5C varied more strongly between different particle sizes than for the reference electrode E1 with  $8 \cdot 10^{-5}\ \text{S m}^{-1}$ . The absolute variation decreased for lower electronic conductivities while the overall cell performance diminished. At  $10^{-6}\ \text{S m}^{-1}$ , the cell performance almost completely faded. A low electronic conductivity of the active material can restrict the cell performance (compare Chapter 4.2). This agrees with my finding that the primary particle size plays a more important role if the electronic conductivity of the active material is high since this allows diffusion to become more prominent as a limiting factor. Based on experimental investigations, Wagner et al. [15] also drew the conclusion that large primary particles can limit cell performance. At low reaction rates, the impact of primary particle size slightly increased (Fig. 4.12b). If the maximum reaction rate dropped below  $10^{-11}\ \text{m}^{2.5}\text{mol}^{-0.5}\text{s}^{-1}$ , the specific capacity at 5C differed more significantly. Large primary particles imply a lower electrochemically active surface area for the same active material content of the electrode. Therefore, the electrochemical reaction slowed down (Chapter 4.1).

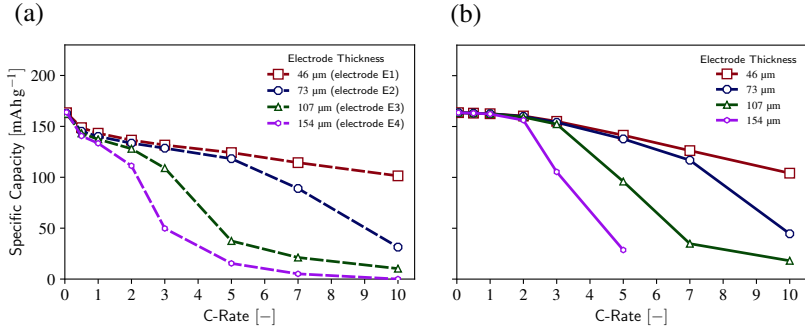


**Figure 4.12:** Influence of (a) electronic conductivity of the active material and (b) reaction rate on the cell performance at 5C. The vertical line corresponds to the reference electrode E1. These images have previously been published in Naumann et al. (2023) [1] .


## 4.5 Impact of Ionic Transport Depending on Electrode Thickness

Finally, I investigated the electrode thickness of HSEs. The HSCM incorporates the electrode thickness at the cell level (Eq. 3.3, 3.9, and 3.10) by the range of the spatial coordinate  $x$ . The modeling studies (Fig. 4.13b) of electrodes E1-E4 (Chapter 3.5) displayed the same qualitative behavior as the experiment (Fig. 4.13a), i.e. for progressively thick electrodes, the rate capability decreased. Electrodes of 107 μm and thicker experienced a drastic drop in specific capacity within a small range of discharge rates before the decrease continued moderately above 7C.

I further investigated the reason for the changing rate capability of HSEs of different thicknesses. Thin electrodes up to 73 μm experienced a general slight decrease of concentration in the active material within the secondary particles (Fig. 4.14a). Furthermore, at a thickness of 107 μm a steep drop in concentration close to the current collector occurred. Electrodes that were even thicker reached the low level of concentration across a larger portion of the thickness.

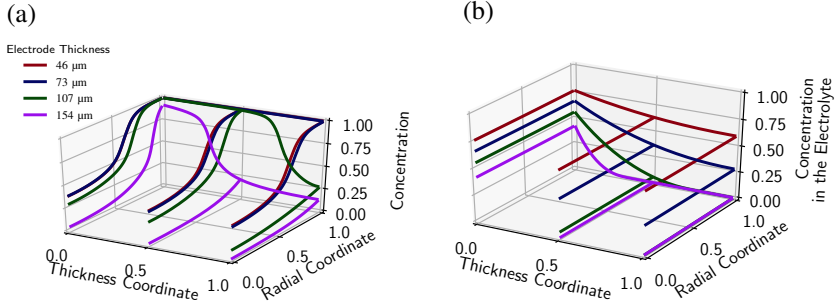


**Figure 4.13:** (a) Experimental (electrode E1-4, see Tab. 3.2) and (b) modeled rate capability depending on electrode thickness.


Experimental results by Amalia Wagner and Nicole Bohn. These images have previously been published in Naumann et al. (2023) [1] 

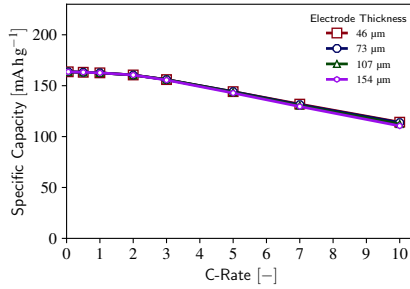
The concentration drop in the active material related to a concentration drop in the electrolyte over the electrode thickness (Fig. 4.14b). This drop steepened with increasing electrode thickness. A lower concentration in the electrolyte caused the electrochemical reaction to run slower, so less concentration entered the active material. Electrodes of 107 μm or thicker even experienced a complete salt depletion of the electrolyte in regions close to the current collector. When the electrolyte depleted, the electrochemical reaction stopped. This explained the drastically reduced concentration in the active material of these regions at the end of discharge. From my results, I deduce that the ionic transport in the electrolyte compromises the cell performance in thick electrodes.

For additional proof of my finding, I increased the conductivity and the diffusivity of the electrolyte by a factor of 10. This resulted in an almost identical rate capability of the cells independent of the electrode thickness (Fig. 4.15). Therefore, I confirmed that concentration drops in the electrolyte reduced the performance of thick electrodes. Classical electrodes with dense secondary active material particles experience the same effect [162, 163]. Note that for even thicker electrodes or higher discharge rates the electronic transport through the solid phase of




**Figure 4.14:** Normalized concentration (a) in the active material and (b) in the electrolyte at the end of a 5C discharge.

These images have previously been published in Naumann et al. (2023) [1] .



**Figure 4.15:** Rate capability when the conductivity and the diffusivity of the electrolyte are artificially increased by a factor of 10.


This image has previously been published in Naumann et al. (2023) [1] .

the electrode, which is mainly determined by conductive additives, may become limiting [164].

## 5 Ionic Transport Paths in Hierarchically Structured Electrodes

Despite first insights into ionic transport in hierarchically structured electrodes (HSEs) (Chapter 2.4), the interplay of intra- and intergranular porosity during ionic transport has not yet been understood<sup>1</sup>. Modeling HSEs can predict the local change in concentration within the electrolyte over time. So far, modeling works focused on a single porous particle [125] or only slightly calendered HSEs [1, 16]. However, realistic applications require high compaction to achieve a sufficient energy density [93]. Here, I use the extended hierarchically structured half-cell model (Chapter 3) to uncover to what extent intra- and intergranular pores contribute to the ionic transport across the electrode. I include the newly developed explicit expression for effective ionic transport through hierarchically porous structures which assumes parallel ionic transport through intra- and intergranular pores (Eq. 3.39, combined transport, compare Fig. 3.4). Also, I consider the simpler assumption that ionic transport mainly takes place in intergranular pores only (Eq. 3.38, intergranular transport, compare Fig. 3.4). I applied Eq. 3.39 and 3.38 to all effective ionic transport properties at half-cell level  $D_{e,\text{eff}}$ ,  $\kappa_{e,\text{eff}}$ , and  $\kappa_{D,\text{eff}}$  in the model (Eq. 3.9 and 3.10). Comparing both assumptions in terms of resulting salt concentration distribution in the electrolyte as well as cell performance, I will show that ionic transport paths depend on the

---

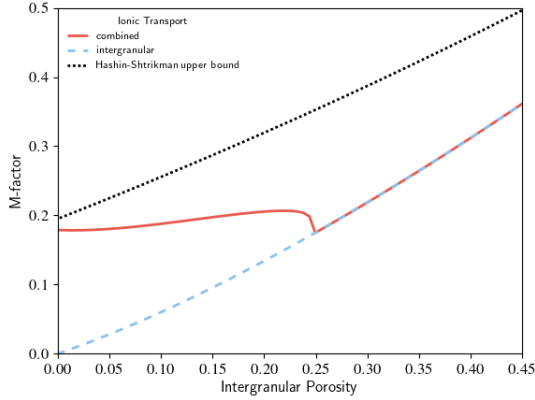
<sup>1</sup> The following chapter has previously been published in Naumann et al. (2024) [2] . The text has been modified.


degree of electrode compaction and on the discharge rate. With increasing compaction and rate, the ionic transport direction in intragranular pores shifts from transport into the particles to transport through the particles. Therefore, the intragranular porosity contributes to the ionic transport across highly calendered HSEs, which has to be accounted for in cell models.

## 5.1 Effective Ionic Transport

The M-factor  $M_{\text{ion}}^{\text{combi}}$  (Eq. 3.42) for combined intra- plus intergranular ionic transport varies with intergranular porosity during calendering (Fig. 5.1). Part of this results from the partial M-factor  $M_{\text{ion}}^{\text{pos}}$  of the intergranular pore network, which depends on the amount of available porosity. Above an intergranular porosity of 0.245, the network of porous particles shows no percolation. Therefore, the partial M-factor  $M^{\text{particles}}$  is zero and both assumptions for ionic transport yield the same overall M-factor. Below the intergranular porosity of 0.245, the intergranular porosity also influences the intragranular portion of the M-factor. Calendering increases the volume fraction and interconnectedness of the porous particles in the electrode. Therefore, M-factor  $M^{\text{particles}}$  rises with decreasing intergranular porosity. As a result, the effective combined intra- plus intergranular ionic transport yields an increasingly higher M-factor than the purely intergranular assumption. The intragranular pores carry a higher fraction of the ionic current with decreasing intergranular porosity. Upon complete elimination of the intergranular porosity, when the purely intergranular assumption yields zero effective ionic transport, an M-factor of 0.19 remains for the realistic assumption of combined intra- plus intergranular transport. This is close to the Hashin-Shtrikman upper bound for material properties of multiphase systems [165] (Chapter C).

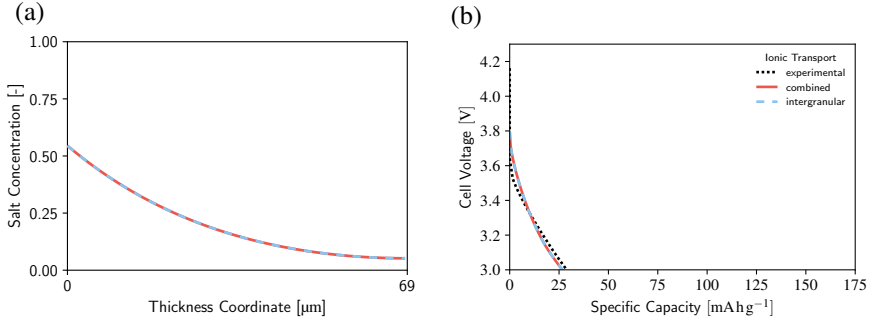
With an intergranular porosity of 0.271 (Tab. 3.3), electrode Cal-1 experiences the same effective ionic transport for both the purely intergranular and for the combined intra- plus intergranular assumption (Fig. 5.1). Ionic transport properties of the HSE directly correlate with salt concentration profiles in the electrolyte, where good ionic transport leads to a high salt concentration with little




**Figure 5.1:** M-factors  $M_{\text{ion}}^{\text{combi}}$  (combined) and  $M_{\text{ion}}^{\text{pos}}$  (intergranular) for ionic transport at cell level. This image has previously been published in Naumann et al. (2024) [2] .

gradient across the electrode thickness. Consequently, there was no difference in electrolyte salt concentration between the two assumptions even at a high discharge rate of 10C (Fig. 5.2a). Ionic transport from the separator to the current collector takes place in the intergranular pores of electrode Cal-1. The equality of effective ionic transport also led to the same discharge curves (Fig. 5.2b) for both assumptions. Chapter D provides the results for all three electrodes at all investigated discharge rates.

Electrode Cal-2 experiences a difference between the two assumptions for ionic transport (Fig. 5.3). Already at a 1C discharge, the purely intergranular assumption considerably underestimated the salt concentration in the electrode compared to the combined intra- plus intergranular assumption (Fig. 5.3b). Faster discharge of 3C (Fig. 5.3c) and 5C (Fig. 5.3d) led to large differences in electrolyte salt concentration. With an intergranular porosity of 0.118 (Tab. 3.3), I expect combined intra- plus intergranular transport at high discharge rates (Fig. 5.1) for electrode Cal-2. The decreasing intergranular porosity forces more ions to travel through



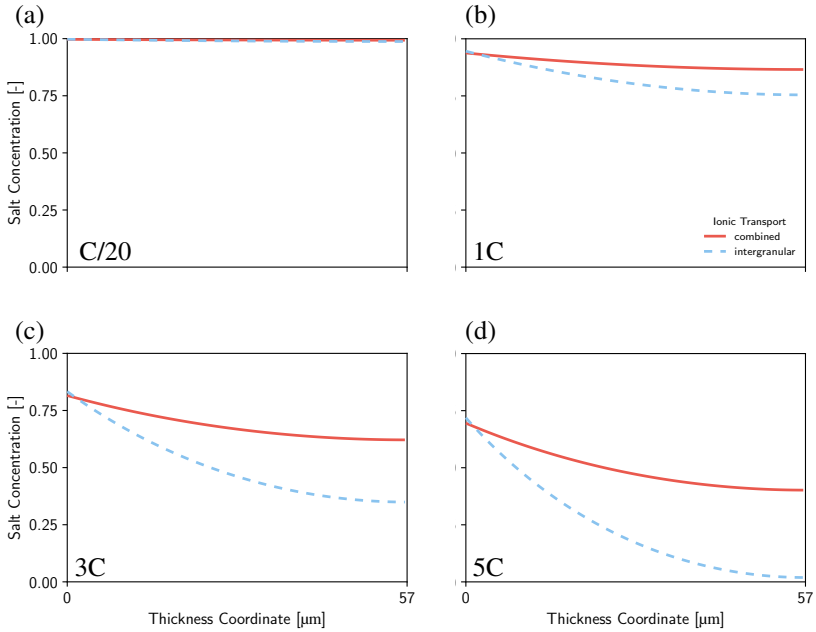
**Figure 5.2:** (a) Salt concentration in the electrolyte and (b) discharge curve of electrode Cal-1 at the end of a 10C discharge.

Experimental results by Marcus Müller and Nicole Bohn. These images have previously been published in Naumann et al. (2024) [2] .


porous particles, so a certain amount of them cross particles without being intercalated into the active material and are available for intercalation in subsequent active material particles.

Further compaction of the electrode extended the observed trend of a higher portion of intragranular ionic transport with rising C-rate and compaction. For electrode Cal-3, the combined intra- plus intergranular assumption yielded a more homogeneous salt concentration across the cell, and thus a higher salt concentration in the positive electrode region (Fig. 5.4), compared to the purely intergranular assumption. Already at C/2 the purely intergranular assumption strongly deviated from the combined intra- plus intergranular assumption (Fig. 5.4b). Even at this low discharge rate, the intragranular pores contribute significantly to the ionic current from the separator to the current collector. Intermediate discharge rates of 1C (Fig. 5.4c) and 2C (Fig. 5.4d) showed an extreme difference between the two assumptions for the ionic transport, which indicates that a large portion of ionic current moves through the intragranular pores. The intragranular porosity dominates the effective ionic transport because of the low intergranular porosity of 0.032 (Tab. 3.3, Fig. 5.1).



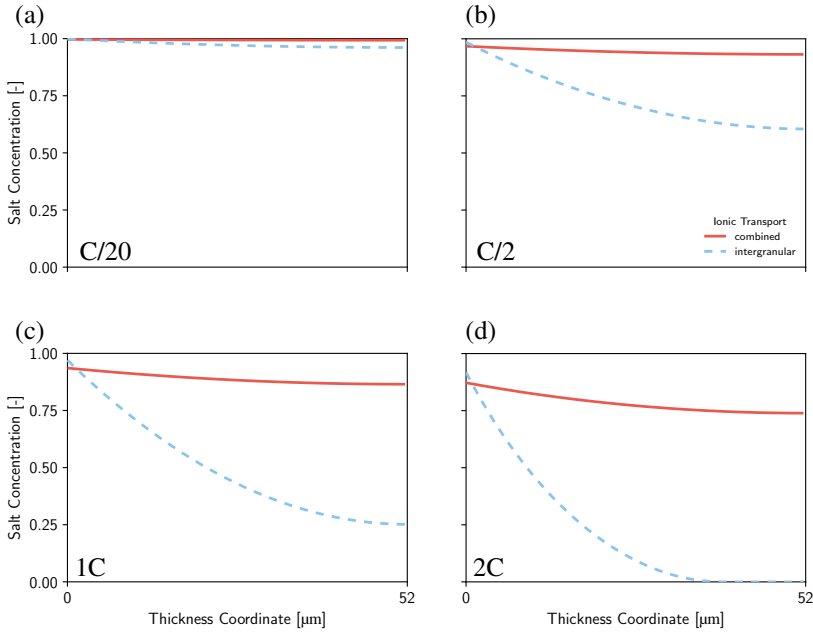


**Figure 5.3:** Salt concentration in the electrolyte of electrode Cal-2 at the end of a (a) C/20, (b) 1C, (c) 3C, (d) 5C discharge.


These images have previously been published in Naumann et al. (2024) [2] .

## 5.2 Effect on the Cell Performance

Up to intermediate discharge rates, both assumptions for the ionic transport yielded similar energy densities of electrode Cal-2 compared to the experiment. At 3C, the deviation lay below 5% (Tab. 5.1). The purely intergranular prediction of the discharge curve only showed a slightly lower cell voltage than the combined intra- plus intergranular prediction (Fig. 5.5a). The energy density obtained by the purely intergranular assumptions became unrealistic at 5C when the model predicted partial salt depletion of the electrolyte (Fig. 5.3d). This causes




**Figure 5.4:** Salt concentration in the electrolyte of electrode Cal-3 at the end of (a) C/20, (b) C/2, (c) 1C, (d) 2C discharge.

These images have previously been published in Naumann et al. (2024) [2] .

the intercalation to come to a halt in the affected electrode regions, yielding a significantly different discharge curve compared to the experiment (Fig. 5.5b) with a 19% deviation in energy density (Tab. 5.1). Assuming combined intra- plus intergranular transport more accurately predicted the experimental discharge curve with only 10% deviation in energy density.

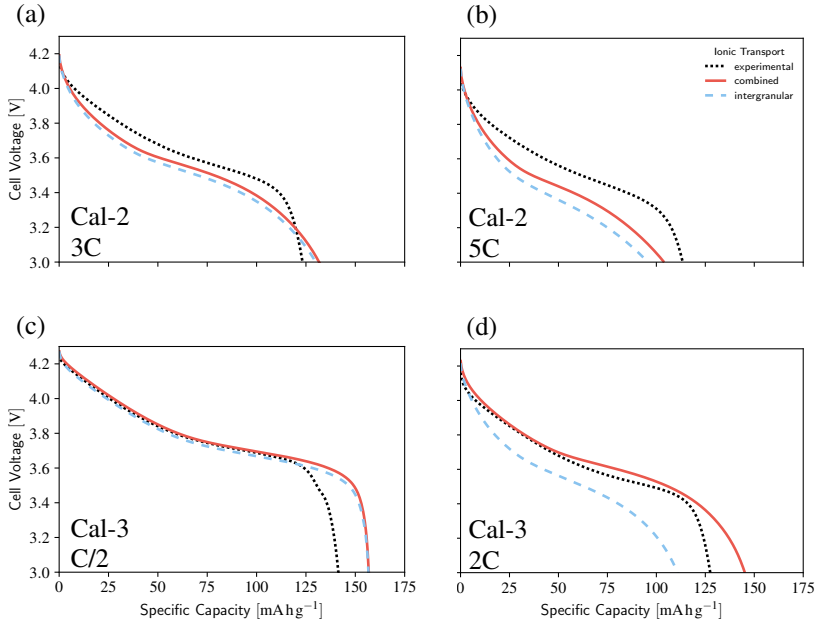
The discharge curve of electrode Cal-3 at 2C resulting from the purely intergranular assumption had no similarity to the experimental results, while the combined intra- plus intergranular assumption closely matched them (Fig. 5.5d). When determining the energy density, the purely intergranular assumption underestimated

**Table 5.1:** Gravimetric energy density [ $\text{Wh kg}^{-1}$ ] (and deviation compared to the experiment) depending on the assumption for ionic transport.


Experimental results by Marcus Müller and Nicole Bohn. This table has previously been published in Naumann et al. (2024) [2] .

Electrode	Discharge Rate	Experiment <sup>[a]</sup>	Intragranular + Intergranular	Intergranular
Cal-2	3C	449	472 (+5%)	462 (+3%)
Cal-2	5C	402	361 (-10%)	326 (-19%)
Cal-3	C/2	535	593 (+11%)	589 (+10%)
Cal-3	2C	464	529 (+14%)	393 (-15%)

the experimental value at 2C by 15%. (Tab. 5.1). Up to a C/2 discharge, both assumptions yielded a higher energy density compared to the experiment (Fig. 5.5c) due to the tendency of the model to overestimate the specific capacity at intermediate discharge rates (Chapter 3.6). Again, the deviation of the modeled discharge curve and the underestimation of energy density occurred when the purely intergranular assumption led to the depletion of the electrolyte in regions close to the current collector (Fig. 5.4d).



**Figure 5.5:** Discharge curve of electrode Cal-2 at (a) 3C and (b) 5C, of electrode Cal-3 at (c) C/2 and (d) 2C.



Experimental results by Marcus Müller and Nicole Bohn. These images have previously been published in Naumann et al. (2024) [2] .

## 6 Summary and Outlook

My goal was to elucidate the relationship between the morphology of hierarchically structured electrodes (HSEs) and the cell performance<sup>1</sup>. The hierarchically structured half-cell model predicts local state changes and thereby tracks the electrochemical processes within the cell across length scales. In addition, the model provides the possibility to independently study the influence of single morphology properties and material properties, which lies beyond experimental capabilities.

Within this work, I outlined the interplay between electrochemical processes within the novel concept of HSEs. Electronic transport in the secondary particles is the dominant process that determines the rate capability of the studied NMC111 electrodes. In case of low electronic conductivity of the active material and no additional conductive aids inside the secondary particles of HSEs, the transport of electrons to the primary particle surfaces where the electrochemical reaction takes place is insufficient. Despite the main transport taking place via conductive additives surrounding the secondary particles and comparatively short electronic transport paths within the secondary particles, the latter play a dominant role since the electronic conductivity of additives and active material differ by several orders of magnitude. A low secondary particle porosity and a small secondary particle size reduce the limitations due to electronic conductivity.

---

<sup>1</sup> Parts of the following chapter have previously been published in Naumann et al. (2023) [1]  and Naumann et al. (2024) [2] . The texts have been combined and modified.

HSEs rely on the small size of the primary particles for short diffusion paths. Still, I showed that diffusion within large primary particles may limit rate capability if the diffusivity in the active material is low. Compared to conventional electrode structures the limitation is mitigated. Electrode thickness affects HSEs in a similar way as classical granular electrodes consisting of dense secondary particles. Namely, I showed that with increasing thickness salt depletion of the electrolyte reduces the rate capability of the cell.

While transport proved to be limiting, the cell performance is insensitive to the experimentally achievable variation of electrochemically active surface area for HSEs contrary to previous anticipation. This insight was enabled by separating the effects of the electrochemically active surface area from primary particle size in the model, while it is nearly impossible to vary these properties independently of each other when processing electrodes.

From my studies, I deduce the following recommendations for the design of HSEs. To increase the rate capability, a good electronic conductivity within the secondary particles of at least  $10^{-4} \text{ S m}^{-1}$  is crucial. In addition, if the diffusivity in the active material lies below  $10^{-15} \text{ m}^2 \text{ s}^{-1}$ , a small primary particle radius below 100 nm fully exploits the advantage of short diffusion paths in HSEs. Ultrafast applications require thin electrodes, at most 70  $\mu\text{m}$ , or electrolytes with a high ion mobility. While this work focuses on balancing effective transport properties to increase the performance of HSEs, considerations of processability and long-term cyclability should be taken into account additionally.

In this work, I also aimed to elucidate ionic transport paths in HSEs. I found that there are different scenarios depending on the discharge rate and the intergranular porosity of the electrode. In electrodes with high intergranular porosity, the ionic current from the separator to the current collector mainly takes place in these pores. The porosity within the particles only transports the ions from the intergranular pores to the particle centers, while they are successively consumed on the way by intercalation into the active material primary particles. Calendered electrodes with a reduced intergranular porosity only display this behavior at low discharge rates. Increasing the discharge rate leads to a transition from the purely

intergranular transport mode to a combined intra- plus intergranular ionic transport across the electrode. Highly calendared electrodes experience this transition at lower discharge rates.

For calendared HSEs, continuum cell models have to account for the ionic transport through porous particles to accurately predict the cell performance, in particular at high levels of calendaring and high discharge rates. In these cases, the purely intergranular assumption severely underestimates the effective ionic transport from the separator to the current collector, which results in an unrealistically low rate of intercalation. Slow discharge may lead to the same prediction of discharge curves and energy density for both assumptions, even though they result in different profiles of electrolyte salt concentration. Only if the intergranular porosity is high, ionic transport from separator to current collector mainly takes place in the intergranular pores, so the purely intergranular assumption correctly predicts the discharge behavior of the cell. My modeling results suggest considering combined intra- plus intergranular ionic transport from the separator to the current collector if the secondary particles are percolated. I proposed a set of explicit formulas for the combined effective ionic transport, which can be readily integrated into multiphysics battery models.

My findings present a guideline for the morphology design of high-performing electrodes of hierarchical structure. Conclusions for HSEs were derived for NMC111 electrodes. However, the general relationships between morphology, material properties, and rate capability likely apply to other systems as well, in particular for active materials with poor electronic conductivity. The developed modeling framework facilitates the systematic morphology optimization of HSEs and enables the realistic prediction of cell performance at high degrees of calendaring, which are necessary to accomplish superior energy and power density. Combined with the specific design recommendations from this work, I have created a basis to fabricate batteries with hierarchically structured electrodes that deliver extraordinarily high power. My work contributes one puzzle piece on the road to energy sustainability.





# Bibliography

- [1] J. Naumann, N. Bohn, O. Birkholz, M. Neumann, M. Müller, J. R. Binder, and M. Kamlah, “Morphology-dependent influences on the performance of battery cells with a hierarchically structured positive electrode,” *Batteries & Supercaps*, vol. 6, no. 12, p. e202300264, 2023. [Online]. Available: <https://onlinelibrary.wiley.com/doi/abs/10.1002/batt.202300264>
- [2] J. Naumann, M. Müller, N. Bohn, J. R. Binder, M. Kamlah, and Y. Gan, “Uncovering ionic transport paths within hierarchically structured battery electrodes,” *ACS Applied Energy Materials*, vol. 7, no. 11, pp. 4786–4793, Jun. 2024. [Online]. Available: <https://doi.org/10.1021/acsaem.4c00505>
- [3] F. Zenith, “Battery-powered freight trains,” *Nature Energy*, vol. 6, no. 11, pp. 1003–1004, Nov. 2021. [Online]. Available: <https://www.nature.com/articles/s41560-021-00914-6>
- [4] J. Zuo and X. Lin, “High-power laser systems,” *Laser & Photonics Reviews*, vol. 16, no. 5, p. 2100741, 2022. [Online]. Available: <https://onlinelibrary.wiley.com/doi/abs/10.1002/lpor.202100741>
- [5] A. Eftekhari, “Lithium-ion batteries with high rate capabilities,” *ACS Sustainable Chemistry & Engineering*, vol. 5, no. 4, pp. 2799–2816, Apr. 2017. [Online]. Available: <https://doi.org/10.1021/acssuschemeng.7b00046>
- [6] M. Sotoudeh, S. Baumgart, M. Dillenz, J. Döhn, K. Forster-Tonigold, K. Helmbrecht, D. Stottmeister, and A. Groß, “Ion mobility in crystalline

- battery materials,” *Advanced Energy Materials*, vol. 14, no. 4, p. 2302550, 2024. [Online]. Available: <https://onlinelibrary.wiley.com/doi/abs/10.1002/aenm.202302550>
- [7] J. Ni and L. Li, “Cathode architectures for rechargeable ion batteries: Progress and perspectives,” *Advanced Materials*, vol. 32, no. 28, p. 2000288, 2020. [Online]. Available: <https://onlinelibrary.wiley.com/doi/abs/10.1002/adma.202000288>
- [8] H. B. Lin, Y. M. Zhang, J. N. Hu, Y. T. Wang, L. D. Xing, M. Q. Xu, X. P. Li, and W. S. Li, “LiNi<sub>0.5</sub>Mn<sub>1.5</sub>O<sub>4</sub> nanoparticles: Synthesis with synergistic effect of polyvinylpyrrolidone and ethylene glycol and performance as cathode of lithium ion battery,” *Journal of Power Sources*, vol. 257, pp. 37–44, Jul. 2014. [Online]. Available: <https://www.sciencedirect.com/science/article/pii/S037877531400113X>
- [9] S. P. Woo, S. H. Lee, K. S. Lee, and Y. S. Yoon, “Effect of increased surface area of LiMn<sub>0.475</sub>Ni<sub>0.475</sub>Al<sub>0.05</sub>O<sub>2</sub> cathode material for Li-ion battery,” *Materials Letters*, vol. 129, pp. 80–83, Aug. 2014. [Online]. Available: <https://www.sciencedirect.com/science/article/pii/S0167577X14008015>
- [10] W. He, W. Guo, H. Wu, L. Lin, Q. Liu, X. Han, Q. Xie, P. Liu, H. Zheng, L. Wang, X. Yu, and D.-L. Peng, “Challenges and recent advances in high capacity Li-rich cathode materials for high energy density lithium-ion batteries,” *Advanced Materials*, vol. 33, no. 50, p. 2005937, 2021. [Online]. Available: <https://onlinelibrary.wiley.com/doi/abs/10.1002/adma.202005937>
- [11] H. Liu, X. Cheng, Y. Chong, H. Yuan, J.-Q. Huang, and Q. Zhang, “Advanced electrode processing of lithium ion batteries: A review of powder technology in battery fabrication,” *Particuology*, vol. 57, pp. 56–71, Aug. 2021. [Online]. Available: <https://www.sciencedirect.com/science/article/pii/S1674200121000134>

- [12] M. Häring, H. Geßwein, N. Bohn, H. Ehrenberg, and J. R. Binder, "Influence of process parameters on the electrochemical properties of hierarchically structured  $\text{Na}_3\text{V}_2(\text{PO}_4)_3/\text{C}$  composites," *ChemElectroChem*, vol. 11, no. 3, p. e202300401, 2024. [Online]. Available: <https://onlinelibrary.wiley.com/doi/abs/10.1002/celec.202300401>
- [13] J. Li, B. Peng, Y. Li, L. Yu, G. Wang, L. Shi, and G. Zhang, "Designed one-pot strategy for dual-carbon-protected  $\text{Na}_3\text{V}_2(\text{PO}_4)_3$  hybrid structure as high-rate and ultrastable cathode for sodium-ion batteries," *Chemistry - A European Journal*, vol. 25, no. 57, pp. 13 094–13 098, 2019. [Online]. Available: <https://onlinelibrary.wiley.com/doi/abs/10.1002/chem.201902400>
- [14] G. Cui, H. Wang, F. Yu, H. Che, X. Liao, L. Li, W. Yang, and Z. Ma, "Scalable synthesis of  $\text{Na}_3\text{V}_2(\text{PO}_4)_3/\text{C}$  with high safety and ultrahigh-rate performance for sodium-ion batteries," *Chinese Journal of Chemical Engineering*, vol. 46, pp. 280–286, Jun. 2022. [Online]. Available: <https://www.sciencedirect.com/science/article/pii/S1004954121003104>
- [15] A. C. Wagner, N. Bohn, H. Geßwein, M. Neumann, M. Osenberg, A. Hilger, I. Manke, V. Schmidt, and J. R. Binder, "Hierarchical structuring of NMC111-cathode materials in lithium-ion batteries: An in-depth study on the influence of primary and secondary particle sizes on electrochemical performance," *ACS Applied Energy Materials*, vol. 3, no. 12, pp. 12 565–12 574, Dec. 2020. [Online]. Available: <https://pubs.acs.org/doi/10.1021/acsaem.0c02494>
- [16] O. Birkholz and M. Kamlah, "Electrochemical modeling of hierarchically structured lithium-ion battery electrodes," *Energy Technology*, vol. 9, no. 6, p. 2000910, 2021. [Online]. Available: <https://onlinelibrary.wiley.com/doi/abs/10.1002/ente.202000910>

- [17] S. Passerini, D. Bresser, A. Moretti, and A. Varzi, *Batteries: Present and Future Energy Storage Challenges*. John Wiley & Sons, Jul. 2020, google-Books-ID: so7zDwAAQBAJ.
- [18] A. Börger and H. Wenzl, *Batterien: Grundlagen, Systeme, Anwendungen*. John Wiley & Sons, Dec. 2022, google-Books-ID: hwiHEAAQBAJ.
- [19] C. M. Julien and A. Mauger, "NCA, NCM811, and the route to Ni-richer lithium-ion batteries," *Energies*, vol. 13, no. 23, p. 6363, Jan. 2020. [Online]. Available: <https://www.mdpi.com/1996-1073/13/23/6363>
- [20] Y.-L. Ding, "Cathode for thin-film lithium-ion batteries," *Lithium-ion Batteries*, p. 55, 2019. [Online]. Available: [https://library.oapen.org/bitstream/handle/20.500.12657/43415/1/external\\_content.pdf#page=69](https://library.oapen.org/bitstream/handle/20.500.12657/43415/1/external_content.pdf#page=69)
- [21] J. Molenda, A. Kulka, A. Milewska, W. Zając, and K. Świerczek, "Structural, transport and electrochemical properties of LiFePO<sub>4</sub> substituted in lithium and iron sublattices (Al, Zr, W, Mn, Co and Ni)," *Materials*, vol. 6, no. 5, pp. 1656–1687, May 2013. [Online]. Available: <https://www.mdpi.com/1996-1944/6/5/1656>
- [22] S. Chen, C. Wu, L. Shen, C. Zhu, Y. Huang, K. Xi, J. Maier, and Y. Yu, "Challenges and perspectives for NASICON-type electrode materials for advanced sodium-ion batteries," *Advanced Materials*, vol. 29, no. 48, p. 1700431, 2017. [Online]. Available: <https://onlinelibrary.wiley.com/doi/abs/10.1002/adma.201700431>
- [23] G. L. Plett, *Battery Management Systems: Battery Modeling. Volume 1*. Boston : London: Artech House, 2015, oCLC: ocn909081842.
- [24] M. Armand, P. Axmann, D. Bresser, M. Copley, K. Edström, C. Ekberg, D. Guyomard, B. Lestriez, P. Novák, M. Petranikova, W. Porcher, S. Trabesinger, M. Wohlfahrt-Mehrens, and H. Zhang, "Lithium-ion batteries - Current state of the art and anticipated developments," *Journal of Power Sources*, vol. 479, p. 228708, Dec. 2020. [Online]. Available: <https://www.sciencedirect.com/science/article/pii/S0378775320310120>

- [25] V. Etacheri, R. Marom, R. Elazari, G. Salitra, and D. Aurbach, "Challenges in the development of advanced Li-ion batteries: A review," *Energy & Environmental Science*, vol. 4, no. 9, pp. 3243–3262, 2011. [Online]. Available: <https://pubs.rsc.org/en/content/articlelanding/2011/ee/c1ee01598b>
- [26] A. Manthiram, "An outlook on lithium ion battery technology," *ACS Central Science*, vol. 3, no. 10, pp. 1063–1069, Oct. 2017. [Online]. Available: <https://doi.org/10.1021/acscentsci.7b00288>
- [27] R. Marom, S. Francis Amalraj, N. Leifer, D. Jacob, and D. Aurbach, "A review of advanced and practical lithium battery materials," *Journal of Materials Chemistry*, vol. 21, no. 27, pp. 9938–9954, 2011. [Online]. Available: <https://pubs.rsc.org/en/content/articlelanding/2011/jm/c0jm04225k>
- [28] Y. Fang, L. Xiao, Z. Chen, X. Ai, Y. Cao, and H. Yang, "Recent advances in sodium-ion battery materials," *Electrochemical Energy Reviews*, vol. 1, no. 3, pp. 294–323, Sep. 2018. [Online]. Available: <https://doi.org/10.1007/s41918-018-0008-x>
- [29] J.-Y. Hwang, S.-T. Myung, and Y.-K. Sun, "Sodium-ion batteries: Present and future," *Chemical Society Reviews*, vol. 46, no. 12, pp. 3529–3614, 2017. [Online]. Available: <https://pubs.rsc.org/en/content/articlelanding/2017/cs/c6cs00776g>
- [30] A. N. Singh, M. Islam, A. Meena, M. Faizan, D. Han, C. Bathula, A. Hajibabaei, R. Anand, and K.-W. Nam, "Unleashing the potential of sodium-ion batteries: Current state and future directions for sustainable energy storage," *Advanced Functional Materials*, vol. 33, no. 46, p. 2304617, 2023. [Online]. Available: <https://onlinelibrary.wiley.com/doi/abs/10.1002/adfm.202304617>
- [31] J. Xiao, X. Li, K. Tang, D. Wang, M. Long, H. Gao, W. Chen, C. Liu, H. Liu, and G. Wang, "Recent progress of emerging cathode materials for

- sodium ion batteries,” *Materials Chemistry Frontiers*, vol. 5, no. 10, pp. 3735–3764, 2021. [Online]. Available: <https://pubs.rsc.org/en/content/articlelanding/2021/qm/d1qm00179e>
- [32] N. Yabuuchi, K. Kubota, M. Dahbi, and S. Komaba, “Research development on sodium-ion batteries,” *Chemical Reviews*, vol. 114, no. 23, pp. 11 636–11 682, Dec. 2014. [Online]. Available: <https://doi.org/10.1021/cr500192f>
- [33] M. Huon Han, E. Gonzalo, G. Singh, and T. Rojo, “A comprehensive review of sodium layered oxides: Powerful cathodes for Na-ion batteries,” *Energy & Environmental Science*, vol. 8, no. 1, pp. 81–102, 2015. [Online]. Available: <https://pubs.rsc.org/en/content/articlelanding/2015/ee/c4ee03192j>
- [34] K. Kubota, N. Yabuuchi, H. Yoshida, M. Dahbi, and S. Komaba, “Layered oxides as positive electrode materials for Na-ion batteries,” *MRS Bulletin*, vol. 39, no. 5, pp. 416–422, May 2014. [Online]. Available: <https://www.cambridge.org/core/journals/mrs-bulletin/article/layered-oxides-as-positive-electrode-materials-for-na-ion-batteries/B99E6B69070009ABEED1A231A78C16C9>
- [35] W. Li, E. M. Erickson, and A. Manthiram, “High-nickel layered oxide cathodes for lithium-based automotive batteries,” *Nature Energy*, vol. 5, no. 1, pp. 26–34, Jan. 2020. [Online]. Available: <https://www.nature.com/articles/s41560-019-0513-0>
- [36] J. Liu, J. Wang, Y. Ni, K. Zhang, F. Cheng, and J. Chen, “Recent breakthroughs and perspectives of high-energy layered oxide cathode materials for lithium ion batteries,” *Materials Today*, vol. 43, pp. 132–165, Mar. 2021. [Online]. Available: <https://www.sciencedirect.com/science/article/pii/S1369702120303837>
- [37] A. Manthiram, B. Song, and W. Li, “A perspective on nickel-rich layered oxide cathodes for lithium-ion batteries,” *Energy Storage Materials*,

- vol. 6, pp. 125–139, Jan. 2017. [Online]. Available:  
<https://www.sciencedirect.com/science/article/pii/S2405829716302112>
- [38] N. Ortiz-Vitoriano, N. E. Drewett, E. Gonzalo, and T. Rojo, “High performance manganese-based layered oxide cathodes: Overcoming the challenges of sodium ion batteries,” *Energy & Environmental Science*, vol. 10, no. 5, pp. 1051–1074, 2017. [Online]. Available:  
<https://pubs.rsc.org/en/content/articlelanding/2017/ee/c7ee00566k>
- [39] P. Rozier and J. M. Tarascon, “Review - Li-rich layered oxide cathodes for next-generation Li-ion batteries: Chances and challenges,” *Journal of The Electrochemical Society*, vol. 162, no. 14, p. A2490, Oct. 2015. [Online]. Available:  
<https://iopscience.iop.org/article/10.1149/2.0111514jes/meta>
- [40] P.-F. Wang, Y. You, Y.-X. Yin, and Y.-G. Guo, “Layered oxide cathodes for sodium-ion batteries: Phase transition, air stability, and performance,” *Advanced Energy Materials*, vol. 8, no. 8, p. 1701912, 2018. [Online]. Available:  
<https://onlinelibrary.wiley.com/doi/abs/10.1002/aenm.201701912>
- [41] Y. Huang, Y. Dong, S. Li, J. Lee, C. Wang, Z. Zhu, W. Xue, Y. Li, and J. Li, “Lithium manganese spinel cathodes for lithium-ion batteries,” *Advanced Energy Materials*, vol. 11, no. 2, p. 2000997, 2021. [Online]. Available:  
<https://onlinelibrary.wiley.com/doi/abs/10.1002/aenm.202000997>
- [42] J.-H. Kim, N. P. W. Pieczonka, and L. Yang, “Challenges and approaches for high-voltage spinel lithium-ion batteries,” *ChemPhysChem*, vol. 15, no. 10, pp. 1940–1954, 2014. [Online]. Available:  
<https://onlinelibrary.wiley.com/doi/abs/10.1002/cphc.201400052>
- [43] J. Wang and X. Sun, “Olivine LiFePO<sub>4</sub>: The remaining challenges for future energy storage,” *Energy & Environmental Science*, vol. 8, no. 4, pp. 1110–1138, 2015. [Online]. Available:  
<https://pubs.rsc.org/en/content/articlelanding/2015/ee/c4ee04016c>

- [44] Y. Wang, P. He, and H. Zhou, “Olivine  $\text{LiFePO}_4$  : Development and future,” *Energy & Environmental Science*, vol. 4, no. 3, pp. 805–817, 2011. [Online]. Available: <https://pubs.rsc.org/en/content/articlelanding/2011/ee/c0ee00176g>
- [45] A. Yamada, M. Hosoya, S.-C. Chung, Y. Kudo, K. Hinokuma, K.-Y. Liu, and Y. Nishi, “Olivine-type cathodes: Achievements and problems,” *Journal of Power Sources*, vol. 119-121, pp. 232–238, Jun. 2003. [Online]. Available: <https://www.sciencedirect.com/science/article/pii/S0378775303002398>
- [46] K. Zaghib, A. Guerfi, P. Hovington, A. Vijn, M. Trudeau, A. Mauger, J. B. Goodenough, and C. M. Julien, “Review and analysis of nanostructured olivine-based lithium rechargeable batteries: Status and trends,” *Journal of Power Sources*, vol. 232, pp. 357–369, Jun. 2013. [Online]. Available: <https://www.sciencedirect.com/science/article/pii/S0378775312019490>
- [47] M. Zhang, N. Garcia-Araez, and A. L. Hector, “Understanding and development of olivine  $\text{LiCoPO}_4$  cathode materials for lithium-ion batteries,” *Journal of Materials Chemistry A*, vol. 6, no. 30, pp. 14 483–14 517, 2018. [Online]. Available: <https://pubs.rsc.org/en/content/articlelanding/2018/ta/c8ta04063j>
- [48] L. Bläubaum, F. Röder, C. Nowak, H. S. Chan, A. Kwade, and U. Krewer, “Impact of particle size distribution on performance of lithium-ion batteries,” *ChemElectroChem*, vol. 7, no. 23, pp. 4755–4766, 2020. [Online]. Available: <https://onlinelibrary.wiley.com/doi/abs/10.1002/celec.202001249>
- [49] H. Buqa, D. Goers, M. Holzapfel, M. E. Spahr, and P. Novák, “High rate capability of graphite negative electrodes for lithium-ion batteries,” *Journal of The Electrochemical Society*, vol. 152, no. 2, p. A474, Jan. 2005. [Online]. Available: <https://iopscience.iop.org/article/10.1149/1.1851055/meta>



- [50] I. Hwang, C. W. Lee, J. C. Kim, and S. Yoon, "Particle size effect of Ni-rich cathode materials on lithium ion battery performance," *Materials Research Bulletin*, vol. 47, no. 1, pp. 73–78, Jan. 2012. [Online]. Available: <https://www.sciencedirect.com/science/article/pii/S002554081100482X>
- [51] Y. Liu, H. Liu, X. Zhao, L. Wang, and G. Liang, "Effect of spherical particle size on the electrochemical properties of lithium iron phosphate," *Journal Wuhan University of Technology, Materials Science Edition*, vol. 34, no. 3, pp. 549–557, Jun. 2019. [Online]. Available: <https://doi.org/10.1007/s11595-019-2086-y>
- [52] H. Seng Chan, L. Bläubaum, D. Vijayshankar, F. Röder, C. Nowak, A. Weber, A. Kwade, and U. Krewer, "Revealing the impact of particle size distribution on ageing of lithium-ion batteries with frequency response analysis," *Batteries & Supercaps*, vol. 6, no. 10, p. e202300203, 2023. [Online]. Available: <https://onlinelibrary.wiley.com/doi/abs/10.1002/batt.202300203>
- [53] M. Abdollahifar, H. Cavers, S. Scheffler, A. Diener, M. Lippke, and A. Kwade, "Insights into influencing electrode calendaring on the battery performance," *Advanced Energy Materials*, p. 2300973, 2023. [Online]. Available: <https://onlinelibrary.wiley.com/doi/abs/10.1002/aenm.202300973>
- [54] A. Shodiev, M. Chouchane, M. Gaberscek, O. Arcelus, J. Xu, H. Oularbi, J. Yu, J. Li, M. Morcrette, and A. A. Franco, "Deconvoluting the benefits of porosity distribution in layered electrodes on the electrochemical performance of Li-ion batteries," *Energy Storage Materials*, vol. 47, pp. 462–471, 2022. [Online]. Available: <https://www.sciencedirect.com/science/article/pii/S2405829722000654>
- [55] T. R. Jow, Xu, Kang, Borodin, Oleg, and Ue, Makoto, *Electrolytes for lithium and lithium-ion batteries*, ser. Modern aspects of electrochemistry. New York: Springer, 2014, no. No. 58.

- [56] Y. Li, F. Wu, Y. Li, M. Liu, X. Feng, Y. Bai, and C. Wu, "Ether-based electrolytes for sodium ion batteries," *Chemical Society Reviews*, vol. 51, no. 11, pp. 4484–4536, 2022. [Online]. Available: <https://pubs.rsc.org/en/content/articlelanding/2022/cs/d1cs00948f>
- [57] A. Ponrouch, D. Monti, A. Boschín, B. Steen, P. Johansson, and M. R. Palacín, "Non-aqueous electrolytes for sodium-ion batteries," *Journal of Materials Chemistry A*, vol. 3, no. 1, pp. 22–42, 2015. [Online]. Available: <https://pubs.rsc.org/en/content/articlelanding/2015/ta/c4ta04428b>
- [58] K. Xu, "Electrolytes and interphases in Li-ion batteries and beyond," *Chemical Reviews*, vol. 114, no. 23, pp. 11 503–11 618, Dec. 2014. [Online]. Available: <https://doi.org/10.1021/cr500003w>
- [59] J. Newman and K. E. Thomas-Alyea, *Electrochemical Systems*. John Wiley & Sons, Nov. 2012, google-Books-ID: eyj4MRa7vLAC.
- [60] I. Baccouche, S. Jemmali, B. Manai, A. Nikolian, N. Omar, and N. Essoukri Ben Amara, "Li-ion battery modeling and characterization: An experimental overview on NMC battery," *International Journal of Energy Research*, vol. 46, no. 4, pp. 3843–3859, 2022. [Online]. Available: <https://onlinelibrary.wiley.com/doi/abs/10.1002/er.7445>
- [61] T. E. Ashton, P. J. Baker, C. Sotelo-Vazquez, C. J. M. Footer, K. M. Kojima, T. Matsukawa, T. Kamiyama, and J. A. Darr, "Stoichiometrically driven disorder and local diffusion in NMC cathodes," *Journal of Materials Chemistry A*, vol. 9, no. 16, pp. 10 477–10 486, 2021. [Online]. Available: <https://pubs.rsc.org/en/content/articlelanding/2021/ta/d1ta01639c>
- [62] K. M. Shaju and P. G. Bruce, "Macroporous  $\text{Li}(\text{Ni}_{1/3}\text{Co}_{1/3}\text{Mn}_{1/3})\text{O}_2$ : A high-power and high-energy cathode for rechargeable lithium batteries," *Advanced Materials*, vol. 18, no. 17, pp. 2330–2334, 2006. [Online]. Available: <https://onlinelibrary.wiley.com/doi/abs/10.1002/adma.200600958>

- [63] B. L. Ellis, K. T. Lee, and L. F. Nazar, "Positive electrode materials for Li-ion and Li-batteries," *Chemistry of Materials*, vol. 22, no. 3, pp. 691–714, Feb. 2010. [Online]. Available: <https://doi.org/10.1021/cm902696j>
- [64] M. Li and J. Lu, "Cobalt in lithium-ion batteries," *Science*, vol. 367, no. 6481, pp. 979–980, Feb. 2020. [Online]. Available: <https://www.science.org/doi/10.1126/science.aba9168>
- [65] J. Xu, F. Lin, M. M. Doeff, and W. Tong, "A review of Ni-based layered oxides for rechargeable Li-ion batteries," *Journal of Materials Chemistry A*, vol. 5, no. 3, pp. 874–901, 2017. [Online]. Available: <https://pubs.rsc.org/en/content/articlelanding/2017/ta/c6ta07991a>
- [66] R. Robert, C. Villevieille, and P. Novák, "Enhancement of the high potential specific charge in layered electrode materials for lithium-ion batteries," *Journal of Materials Chemistry A*, vol. 2, no. 23, pp. 8589–8598, 2014. [Online]. Available: <https://pubs.rsc.org/en/content/articlelanding/2014/ta/c3ta12643a>
- [67] B. Xu, D. Qian, Z. Wang, and Y. S. Meng, "Recent progress in cathode materials research for advanced lithium ion batteries," *Materials Science and Engineering R: Reports*, vol. 73, no. 5, pp. 51–65, May 2012. [Online]. Available: <https://www.sciencedirect.com/science/article/pii/S0927796X12000186>
- [68] S.-C. Yin, Y.-H. Rho, I. Swainson, and L. F. Nazar, "X-ray/neutron diffraction and electrochemical studies of lithium de/re-intercalation in  $\text{Li}_{1-x}\text{Co}_{1/3}\text{Ni}_{1/3}\text{Mn}_{1/3}\text{O}_2$  ( $x = 0 \rightarrow 1$ )," *Chemistry of Materials*, vol. 18, no. 7, pp. 1901–1910, Apr. 2006. [Online]. Available: <https://doi.org/10.1021/cm0511769>
- [69] M. Oljaca, B. Blizanac, A. Du Pasquier, Y. Sun, R. Bontchev, A. Suszko, R. Wall, and K. Koehlert, "Novel  $\text{Li}(\text{Ni}_{1/3}\text{Co}_{1/3}\text{Mn}_{1/3})\text{O}_2$  cathode morphologies for high power Li-ion batteries," *Journal of Power Sources*,

- vol. 248, pp. 729–738, Feb. 2014. [Online]. Available:  
<https://www.sciencedirect.com/science/article/pii/S037877531301608X>
- [70] W. Zheng, X. Huang, Y. Ren, H. Wang, S. Zhou, Y. Chen, X. Ding, and T. Zhou, “Porous spherical  $\text{Na}_3\text{V}_2(\text{PO}_4)_3/\text{C}$  composites synthesized via a spray drying-assisted process with high-rate performance as cathode materials for sodium-ion batteries,” *Solid State Ionics*, vol. 308, pp. 161–166, Oct. 2017. [Online]. Available:  
<https://www.sciencedirect.com/science/article/pii/S0167273817303065>
- [71] L. Li, L. Wang, X. Zhang, M. Xie, F. Wu, and R. Chen, “Structural and electrochemical study of hierarchical  $\text{LiNi}_{1/3}\text{Co}_{1/3}\text{Mn}_{1/3}\text{O}_2$  cathode material for lithium-ion batteries,” *ACS Applied Materials & Interfaces*, vol. 7, no. 39, pp. 21 939–21 947, Oct. 2015. [Online]. Available:  
<https://doi.org/10.1021/acsami.5b06584>
- [72] A. H. Salehi, S. M. Masoudpanah, M. Hasheminasari, A. Yaghtin, D. Safanama, C. K. Ong, S. Adams, K. Zaghib, and M. V. Reddy, “Facile synthesis of hierarchical porous  $\text{Na}_3\text{V}_2(\text{PO}_4)_3/\text{C}$  composites with high-performance Na storage properties,” *Journal of Power Sources*, vol. 481, p. 228828, Jan. 2021. [Online]. Available:  
<https://www.sciencedirect.com/science/article/pii/S0378775320311320>
- [73] P.-E. Cabelguen, D. Peralta, M. Cugnet, and P. Maillet, “Impact of morphological changes of  $\text{LiNi}_{1/3}\text{Mn}_{1/3}\text{Co}_{1/3}\text{O}_2$  on lithium-ion cathode performances,” *Journal of Power Sources*, vol. 346, pp. 13–23, Apr. 2017. [Online]. Available:  
<https://www.sciencedirect.com/science/article/pii/S0378775317301891>
- [74] L. Zhou, K. Zhang, Z. Hu, Z. Tao, L. Mai, Y.-M. Kang, S.-L. Chou, and J. Chen, “Recent developments on and prospects for electrode materials with hierarchical structures for lithium-ion batteries,” *Advanced Energy Materials*, vol. 8, no. 6, p. 1701415, 2018. [Online]. Available:  
<https://onlinelibrary.wiley.com/doi/abs/10.1002/aenm.201701415>

- [75] Z. Chen, J. Wang, D. Chao, T. Baikie, L. Bai, S. Chen, Y. Zhao, T. C. Sum, J. Lin, and Z. Shen, "Hierarchical porous  $\text{LiNi}_{1/3}\text{Co}_{1/3}\text{Mn}_{1/3}\text{O}_2$  nano-/micro spherical cathode material: Minimized cation mixing and improved  $\text{Li}^+$  mobility for enhanced electrochemical performance," *Scientific Reports*, vol. 6, no. 1, pp. 1–10, May 2016. [Online]. Available: <https://www.nature.com/articles/srep25771>
- [76] P.-E. Cabelguen, D. Peralta, M. Cugnet, J.-C. Badot, O. Dubrunfaut, and P. Mailley, "Rational analysis of layered oxide power performance limitations in a lithium battery application," *Advanced Sustainable Systems*, vol. 1, no. 11, p. 1700078, 2017. [Online]. Available: <https://onlinelibrary.wiley.com/doi/abs/10.1002/adsu.201700078>
- [77] D. Chen, D. Kramer, and R. Mönig, "Chemomechanical fatigue of  $\text{LiMn}_{1.95}\text{Al}_{0.05}\text{O}_4$  electrodes for lithium-ion batteries," *Electrochimica Acta*, vol. 259, pp. 939–948, Jan. 2018. [Online]. Available: <https://www.sciencedirect.com/science/article/pii/S0013468617323253>
- [78] Z. Jian, W. Han, X. Lu, H. Yang, Y.-S. Hu, J. Zhou, Z. Zhou, J. Li, W. Chen, D. Chen, and L. Chen, "Superior electrochemical performance and storage mechanism of  $\text{Na}_3\text{V}_2(\text{PO}_4)_3$  cathode for room-temperature sodium-ion batteries," *Advanced Energy Materials*, vol. 3, no. 2, pp. 156–160, 2013. [Online]. Available: <https://onlinelibrary.wiley.com/doi/abs/10.1002/aenm.201200558>
- [79] P. L. Mani Kanta, N. L. Priya, P. Oza, M. Venkatesh, S. K. Yadav, B. Das, G. Sundararajan, and R. Gopalan, "Unusual case of higher cyclic stability at a wider voltage window in sodium vanadium phosphate," *ACS Applied Energy Materials*, vol. 4, no. 11, pp. 12 581–12 592, Nov. 2021. [Online]. Available: <https://doi.org/10.1021/acsaem.1c02367>
- [80] R. Thangavel, D. Han, B. Moorthy, B. K. Ganesan, M. Moorthy, Y. Park, K.-W. Nam, and Y.-S. Lee, "Understanding the structural phase transitions in  $\text{Na}_3\text{V}_2(\text{PO}_4)_3$  symmetrical sodium-ion batteries using synchrotron-based X-ray techniques," *Small Methods*, vol. 6, no. 2, p.

- 2100888, 2022. [Online]. Available:  
<https://onlinelibrary.wiley.com/doi/abs/10.1002/smt.202100888>
- [81] K. Saravanan, C. W. Mason, A. Rudola, K. H. Wong, and P. Balaya, “The first report on excellent cycling stability and superior rate capability of  $\text{Na}_3\text{V}_2(\text{PO}_4)_3$  for sodium ion batteries,” *Advanced Energy Materials*, vol. 3, no. 4, pp. 444–450, 2013. [Online]. Available:  
<https://onlinelibrary.wiley.com/doi/abs/10.1002/aenm.201200803>
- [82] A. S. Aricò, P. Bruce, B. Scrosati, J.-M. Tarascon, and W. van Schalkwijk, “Nanostructured materials for advanced energy conversion and storage devices,” *Nature Materials*, vol. 4, no. 5, pp. 366–377, May 2005. [Online]. Available: <https://www.nature.com/articles/nmat1368>
- [83] A. A. AbdelHamid, A. Mendoza-Garcia, and J. Y. Ying, “Advances in and prospects of nanomaterials’ morphological control for lithium rechargeable batteries,” *Nano Energy*, vol. 93, p. 106860, Mar. 2022. [Online]. Available:  
<https://linkinghub.elsevier.com/retrieve/pii/S2211285521011095>
- [84] Y.-G. Guo, J.-S. Hu, and L.-J. Wan, “Nanostructured materials for electrochemical energy conversion and storage devices,” *Advanced Materials*, vol. 20, no. 15, pp. 2878–2887, 2008. [Online]. Available:  
<https://onlinelibrary.wiley.com/doi/abs/10.1002/adma.200800627>
- [85] W. Duan, Z. Zhu, H. Li, Z. Hu, K. Zhang, F. Cheng, and J. Chen, “ $\text{Na}_3\text{V}_2(\text{PO}_4)_3$ @C core-shell nanocomposites for rechargeable sodium-ion batteries,” *Journal of Materials Chemistry A*, vol. 2, no. 23, pp. 8668–8675, 2014. [Online]. Available:  
<https://pubs.rsc.org/en/content/articlelanding/2014/ta/c4ta00106k>
- [86] H. Wang, D. Jiang, Y. Zhang, G. Li, X. Lan, H. Zhong, Z. Zhang, and Y. Jiang, “Self-combustion synthesis of  $\text{Na}_3\text{V}_2(\text{PO}_4)_3$  nanoparticles coated with carbon shell as cathode materials for sodium-ion batteries,” *Electrochimica Acta*, vol. 155, pp. 23–28, Feb. 2015. [Online]. Available:  
<https://www.sciencedirect.com/science/article/pii/S0013468614026218>

- [87] X. Tian, Y. Zhu, Z. Tang, P. Xie, A. Natarajan, and Y. Zhou, "Ni-rich  $\text{LiNi}_{0.6}\text{Co}_{0.2}\text{Mn}_{0.2}\text{O}_2$  nanoparticles enwrapped by a 3D graphene aerogel network as a high-performance cathode material for Li-ion batteries," *Ceramics International*, vol. 45, no. 17, Part A, pp. 22 233–22 240, Dec. 2019. [Online]. Available: <https://www.sciencedirect.com/science/article/pii/S0272884219320693>
- [88] M. Müller, L. Schneider, N. Bohn, J. R. Binder, and W. Bauer, "Effect of nanostructured and open-porous particle morphology on electrode processing and electrochemical performance of Li-ion batteries," *ACS Applied Energy Materials*, vol. 4, no. 2, pp. 1993–2003, Feb. 2021. [Online]. Available: <https://doi.org/10.1021/acsaem.0c03187>
- [89] M. Schmidt, V. Mereacre, H. Geßwein, N. Bohn, S. Indris, and J. R. Binder, "High performance of porous, hierarchically structured  $\text{P2-Na}_{0.6}\text{Al}_{0.11-x}\text{Ni}_{0.22-y}\text{Fe}_{x+y}\text{Mn}_{0.66}\text{O}_2$  cathode materials," *Advanced Energy Materials*, vol. 14, no. 19, p. 2301854, 2024. [Online]. Available: <https://onlinelibrary.wiley.com/doi/abs/10.1002/aenm.202301854>
- [90] J. Weng, J. Duan, C. Sun, P. Liu, A. Li, P. Zhou, and J. Zhou, "Construction of hierarchical  $\text{K}_{0.7}\text{Mn}_{0.7}\text{Mg}_{0.3}\text{O}_2$  microparticles as high capacity & long cycle life cathode materials for low-cost potassium-ion batteries," *Chemical Engineering Journal*, vol. 392, p. 123649, Jul. 2020. [Online]. Available: <https://www.sciencedirect.com/science/article/pii/S1385894719330645>
- [91] X. Wu, C. Yin, M. Zhang, Y. Xie, J. Hu, R. Long, X. Wu, and X. Wu, "The intercalation cathode of MOFs-driven vanadium-based composite embedded in N-doped carbon for aqueous zinc ion batteries," *Chemical Engineering Journal*, vol. 452, p. 139573, Jan. 2023. [Online]. Available: <https://www.sciencedirect.com/science/article/pii/S1385894722050525>
- [92] L. Li, X. Du, G. Liu, Y. Zhang, Z. Zhang, and J. Li, "Micro-/mesoporous Co-NC embedded three-dimensional ordered macroporous metal framework as Li-S battery cathode towards effective polysulfide catalysis

- and retention,” *Journal of Alloys and Compounds*, vol. 893, p. 162327, Feb. 2022. [Online]. Available:  
<https://www.sciencedirect.com/science/article/pii/S0925838821037373>
- [93] L. Schneider, J. Klemens, E. C. Herbst, M. Müller, P. Scharfer, W. Schabel, W. Bauer, and H. Ehrenberg, “Transport properties in electrodes for lithium-ion batteries: Comparison of compact versus porous NCM particles,” *Journal of The Electrochemical Society*, vol. 169, no. 10, p. 100553, Oct. 2022. [Online]. Available:  
<https://dx.doi.org/10.1149/1945-7111/ac9c37>
- [94] R. Tao, B. Steinhoff, K. Uzun, B. La Riviere, K. Sardo, B. Skelly, R. Hill, Y.-T. Cheng, and J. Li, “Correlation among porosity, mechanical properties, morphology, electronic conductivity and electrochemical kinetics of dry-processed electrodes,” *Journal of Power Sources*, vol. 581, p. 233481, Oct. 2023. [Online]. Available:  
<https://www.sciencedirect.com/science/article/pii/S0378775323008571>
- [95] M. Häringer, “Synthese und Hochskalierung hierarchisch strukturierter NASICON-Materialien als Kathodenmaterial für Natrium-Ionen-Batterien,” 2023. [Online]. Available:  
<https://publikationen.bibliothek.kit.edu/1000162274>
- [96] K.-Y. Oh, N. A. Samad, Y. Kim, J. B. Siegel, A. G. Stefanopoulou, and B. I. Epureanu, “A novel phenomenological multi-physics model of Li-ion battery cells,” *Journal of Power Sources*, vol. 326, pp. 447–458, Sep. 2016. [Online]. Available:  
<https://linkinghub.elsevier.com/retrieve/pii/S0378775316308758>
- [97] X. Feng, C. Weng, M. Ouyang, and J. Sun, “Online internal short circuit detection for a large format lithium ion battery,” *Applied Energy*, vol. 161, pp. 168–180, Jan. 2016. [Online]. Available:  
<https://www.sciencedirect.com/science/article/pii/S0306261915012465>
- [98] A. Weng, E. Olide, I. Kovalchuk, J. Siegel, and A. Stefanopoulou, “Modeling battery formation: Boosted SEI growth, multi-species



- reactions, and irreversible expansion,” *Journal of The Electrochemical Society*, 2023. [Online]. Available: <http://iopscience.iop.org/article/10.1149/1945-7111/aceffe>
- [99] S. Nejad, D. T. Gladwin, and D. A. Stone, “A systematic review of lumped-parameter equivalent circuit models for real-time estimation of lithium-ion battery states,” *Journal of Power Sources*, vol. 316, pp. 183–196, Jun. 2016. [Online]. Available: <https://www.sciencedirect.com/science/article/pii/S0378775316302427>
- [100] L. Zhang, H. Peng, Z. Ning, Z. Mu, and C. Sun, “Comparative research on RC equivalent circuit models for lithium-ion batteries of electric vehicles,” *Applied Sciences*, vol. 7, no. 10, p. 1002, Oct. 2017. [Online]. Available: <https://www.mdpi.com/2076-3417/7/10/1002>
- [101] M.-K. Tran, A. DaCosta, A. Mevawalla, S. Panchal, and M. Fowler, “Comparative study of equivalent circuit models performance in four common lithium-ion batteries: LFP, NMC, LMO, NCA,” *Batteries*, vol. 7, no. 3, p. 51, Sep. 2021. [Online]. Available: <https://www.mdpi.com/2313-0105/7/3/51>
- [102] J. Zhou, B. Xing, and C. Wang, “A review of lithium ion batteries electrochemical models for electric vehicles,” *E3S Web of Conferences*, vol. 185, p. 04001, 2020. [Online]. Available: [https://www.e3s-conferences.org/articles/e3sconf/abs/2020/45/e3sconf\\_iceeb2020\\_04001/e3sconf\\_iceeb2020\\_04001.html](https://www.e3s-conferences.org/articles/e3sconf/abs/2020/45/e3sconf_iceeb2020_04001/e3sconf_iceeb2020_04001.html)
- [103] P. Hashemzadeh, M. Désilets, M. Lacroix, and A. Jokar, “Investigation of the P2D and of the modified single-particle models for predicting the nonlinear behavior of Li-ion batteries,” *Journal of Energy Storage*, vol. 52, p. 104909, Aug. 2022. [Online]. Available: <https://www.sciencedirect.com/science/article/pii/S2352152X22009161>
- [104] F. B. Planella, W. Ai, A. M. Boyce, A. Ghosh, I. Korotkin, S. Sahu, V. Sulzer, R. Timms, T. G. Tranter, M. Zyskin, S. J. Cooper, J. S. Edge,

- J. M. Foster, M. Marinescu, B. Wu, and G. Richardson, "A continuum of physics-based lithium-ion battery models reviewed," *Progress in Energy*, vol. 4, no. 4, p. 042003, Jul. 2022. [Online]. Available: <https://dx.doi.org/10.1088/2516-1083/ac7d31>
- [105] S. Hein, T. Danner, and A. Latz, "An electrochemical model of lithium plating and stripping in lithium ion batteries," *ACS Applied Energy Materials*, vol. 3, no. 9, pp. 8519–8531, Sep. 2020. [Online]. Available: <https://doi.org/10.1021/acsaem.0c01155>
- [106] H. Euchner and A. Groß, "Atomistic modeling of Li- and post-Li-ion batteries," *Physical Review Materials*, vol. 6, no. 4, p. 040302, Apr. 2022. [Online]. Available: <https://link.aps.org/doi/10.1103/PhysRevMaterials.6.040302>
- [107] M. Doyle, T. F. Fuller, and J. Newman, "Modeling of galvanostatic charge and discharge of the lithium/polymer/insertion cell," *Journal of The Electrochemical Society*, vol. 140, no. 6, p. 1526, Jun. 1993. [Online]. Available: <https://iopscience.iop.org/article/10.1149/1.2221597/meta>
- [108] T. F. Fuller, M. Doyle, and J. Newman, "Simulation and optimization of the dual lithium ion insertion cell," *Journal of The Electrochemical Society*, vol. 141, no. 1, pp. 1–10, Jan. 1994. [Online]. Available: <http://jes.ecsdl.org/content/141/1/1>
- [109] C. M. Doyle, "Design and simulation of lithium rechargeable batteries," Lawrence Berkeley National Lab. (LBNL), Berkeley, CA (United States), Tech. Rep. LBL-37650, Aug. 1995. [Online]. Available: <https://www.osti.gov/biblio/203473-design-simulation-lithium-rechargeable-batteries>
- [110] M. Doyle and J. Newman, "Modeling the performance of rechargeable lithium-based cells: design correlations for limiting cases," *Journal of Power Sources*, vol. 54, no. 1, pp. 46–51, Mar. 1995. [Online]. Available: <https://www.sciencedirect.com/science/article/pii/0378775394020385>

- 
- [111] M. Doyle and J. Newman, "The use of mathematical modeling in the design of lithium/polymer battery systems," *Electrochimica Acta*, vol. 40, no. 13, pp. 2191–2196, Oct. 1995. [Online]. Available: <https://www.sciencedirect.com/science/article/pii/0013468695001628>
- [112] M. Doyle, J. Newman, A. S. Gozdz, C. N. Schmutz, and J.-M. Tarascon, "Comparison of modeling predictions with experimental data from plastic lithium ion cells," *Journal of The Electrochemical Society*, vol. 143, no. 6, p. 1890, Jun. 1996. [Online]. Available: <https://iopscience.iop.org/article/10.1149/1.1836921/meta>
- [113] M. Doyle and J. Newman, "Analysis of capacity-rate data for lithium batteries using simplified models of the discharge process," *Journal of Applied Electrochemistry*, vol. 27, no. 7, pp. 846–856, Jul. 1997. [Online]. Available: <https://doi.org/10.1023/A:1018481030499>
- [114] M. Doyle, J. P. Meyers, and J. Newman, "Computer simulations of the impedance response of lithium rechargeable batteries," *Journal of The Electrochemical Society*, vol. 147, no. 1, p. 99, Jan. 2000. [Online]. Available: <https://iopscience.iop.org/article/10.1149/1.1393162/meta>
- [115] M. Doyle and Y. Fuentes, "Computer simulations of a lithium-ion polymer battery and implications for higher capacity next-generation battery designs," *Journal of The Electrochemical Society*, vol. 150, no. 6, p. A706, Apr. 2003. [Online]. Available: <https://iopscience.iop.org/article/10.1149/1.1569478/meta>
- [116] C. Lin, A. Tang, and J. Xing, "Evaluation of electrochemical models based battery state-of-charge estimation approaches for electric vehicles," *Applied Energy*, vol. 207, pp. 394–404, Dec. 2017. [Online]. Available: <https://linkinghub.elsevier.com/retrieve/pii/S030626191730613X>
- [117] J. Li, K. Adewuyi, N. Lotfi, R. G. Landers, and J. Park, "A single particle model with chemical/mechanical degradation physics for lithium ion battery State of Health (SOH) estimation," *Applied Energy*, vol. 212, pp.

- 1178–1190, Feb. 2018. [Online]. Available:  
<https://www.sciencedirect.com/science/article/pii/S0306261918300114>
- [118] M. Al-Gabalawy, N. S. Hosny, and S. A. Hussien, “Lithium-ion battery modeling including degradation based on single-particle approximations,” *Batteries*, vol. 6, no. 3, p. 37, Sep. 2020. [Online]. Available: <https://www.mdpi.com/2313-0105/6/3/37>
- [119] J. Newman and W. Tiedemann, “Porous-electrode theory with battery applications,” *AIChE Journal*, vol. 21, no. 1, pp. 25–41, 1975. [Online]. Available:  
<https://onlinelibrary.wiley.com/doi/abs/10.1002/aic.690210103>
- [120] K. E. Thomas, J. Newman, and R. M. Darling, “Mathematical modeling of lithium batteries,” in *Advances in Lithium-Ion Batteries*, W. A. van Schalkwijk and B. Scrosati, Eds. Boston, MA: Springer US, 2002, pp. 345–392. [Online]. Available: [https://doi.org/10.1007/0-306-47508-1\\_13](https://doi.org/10.1007/0-306-47508-1_13)
- [121] M. Lagnoni, C. Nicolella, and A. Bertei, “Comparison of electrolyte transport modelling in lithium-ion batteries: Concentrated solution theory vs generalized Nernst-Planck model,” *Journal of The Electrochemical Society*, vol. 169, no. 2, p. 020570, Feb. 2022. [Online]. Available:  
<https://dx.doi.org/10.1149/1945-7111/ac51f4>
- [122] M. Ganser, F. E. Hildebrand, M. Klinsmann, M. Hanauer, M. Kamlah, and R. M. McMeeking, “An extended formulation of Butler-Volmer electrochemical reaction kinetics including the influence of mechanics,” *Journal of The Electrochemical Society*, vol. 166, no. 4, p. H167, Mar. 2019. [Online]. Available:  
<https://iopscience.iop.org/article/10.1149/2.1111904jes/meta>
- [123] M. Neumann, S. E. Wetterauer, M. Osenberg, A. Hilger, P. Gräfensteiner, A. Wagner, N. Bohn, J. R. Binder, I. Manke, T. Carraro, and V. Schmidt, “A data-driven modeling approach to quantify morphology effects on transport properties in nanostructured NMC particles,” *International*

- Journal of Solids and Structures*, vol. 280, p. 112394, Sep. 2023.  
[Online]. Available:  
<https://www.sciencedirect.com/science/article/pii/S0020768323002913>
- [124] B. Wu and W. Lu, “Mechanical-electrochemical modeling of agglomerate particles in lithium-ion battery electrodes,” *Journal of The Electrochemical Society*, vol. 163, no. 14, p. A3131, Nov. 2016. [Online]. Available: <https://iopscience.iop.org/article/10.1149/2.1331614jes/meta>
- [125] S. Cernak, F. Schürholz, M. Kespe, and H. Nirschl, “Three-dimensional numerical simulations on the effect of particle porosity of lithium-nickel-manganese-cobalt-oxide on the performance of positive lithium-ion battery electrodes,” *Energy Technology*, vol. 9, no. 6, p. 2000676, 2021. [Online]. Available:  
<https://onlinelibrary.wiley.com/doi/abs/10.1002/ente.202000676>
- [126] S. Lüth, U. S. Sauter, and W. G. Bessler, “An agglomerate model of lithium-ion battery cathodes,” *Journal of The Electrochemical Society*, vol. 163, no. 2, p. A210, Nov. 2015. [Online]. Available:  
<https://iopscience.iop.org/article/10.1149/2.0291602jes/meta>
- [127] Q. Xiong, T. G. Baychev, and A. P. Jivkov, “Review of pore network modelling of porous media: Experimental characterisations, network constructions and applications to reactive transport,” *Journal of Contaminant Hydrology*, vol. 192, pp. 101–117, 2016. [Online]. Available:  
<https://www.sciencedirect.com/science/article/pii/S016977221630122X>
- [128] J. J. Meyers and A. I. Liapis, “Network modeling of the intraparticle convection and diffusion of molecules in porous particles packed in a chromatographic column,” *Journal of Chromatography A*, vol. 827, no. 2, pp. 197–213, 1998. [Online]. Available:  
<https://www.sciencedirect.com/science/article/pii/S002196739800658X>
- [129] J. J. Meyers and A. I. Liapis, “Network modeling of the convective flow and diffusion of molecules adsorbing in monoliths and in porous particles

- packed in a chromatographic column,” *Journal of Chromatography A*, vol. 852, no. 1, pp. 3–23, 1999. [Online]. Available: <https://www.sciencedirect.com/science/article/pii/S0021967399004434>
- [130] M. A. Sadeghi, M. Aghighi, J. Barralet, and J. T. Gostick, “Pore network modeling of reaction-diffusion in hierarchical porous particles: The effects of microstructure,” *Chemical Engineering Journal*, vol. 330, pp. 1002–1011, 2017. [Online]. Available: <https://www.sciencedirect.com/science/article/pii/S138589471731286X>
- [131] L. Chen, R. Zhang, T. Min, Q. Kang, and W. Tao, “Pore-scale study of effects of macroscopic pores and their distributions on reactive transport in hierarchical porous media,” *Chemical Engineering Journal*, vol. 349, pp. 428–437, 2018. [Online]. Available: <https://www.sciencedirect.com/science/article/pii/S1385894718309203>
- [132] D. Schneider, D. Kondrashova, R. Valiullin, A. Bunde, and J. Kärger, “Mesopore-promoted transport in microporous materials,” *Chemie Ingenieur Technik*, vol. 87, no. 12, pp. 1794–1809, 2015. [Online]. Available: <https://onlinelibrary.wiley.com/doi/abs/10.1002/cite.201500037>
- [133] D. Schneider, D. Mehlhorn, P. Zeigermann, J. Kärger, and R. Valiullin, “Transport properties of hierarchical micro-mesoporous materials,” *Chemical Society Reviews*, vol. 45, no. 12, pp. 3439–3467, 2016. [Online]. Available: <https://pubs.rsc.org/en/content/articlelanding/2016/cs/c5cs00715a>
- [134] B. Coasne, A. Galarneau, C. Gerardin, F. Fajula, and F. Villemot, “Molecular simulation of adsorption and transport in hierarchical porous materials,” *Langmuir*, vol. 29, no. 25, pp. 7864–7875, 2013. [Online]. Available: <https://doi.org/10.1021/la401228k>
- [135] U. Tallarek, D. Hlushkou, J. Rybka, and A. Höltzel, “Multiscale simulation of diffusion in porous media: From interfacial dynamics to

- hierarchical porosity,” *The Journal of Physical Chemistry C*, vol. 123, no. 24, pp. 15 099–15 112, 2019. [Online]. Available: <https://doi.org/10.1021/acs.jpcc.9b03250>
- [136] F. Gritti and G. Guiochon, “Theoretical investigation of diffusion along columns packed with fully and superficially porous particles,” *Journal of Chromatography A*, vol. 1218, no. 22, pp. 3476–3488, 2011. [Online]. Available: <https://www.sciencedirect.com/science/article/pii/S0021967311004389>
- [137] F. Gritti and G. Guiochon, “Diffusion models in chromatographic columns packed with fully and superficially porous particles,” *Chemical Engineering Science*, vol. 66, no. 17, pp. 3773–3781, 2011. [Online]. Available: <https://www.sciencedirect.com/science/article/pii/S0009250911002934>
- [138] M. Barrande, R. Bouchet, and R. Denoyel, “Tortuosity of porous particles,” *Analytical Chemistry*, vol. 79, no. 23, pp. 9115–9121, 2007. [Online]. Available: <https://doi.org/10.1021/ac071377r>
- [139] A. Schmidt, E. Ramani, T. Carraro, J. Joos, A. Weber, M. Kamlah, and E. Ivers-Tiffée, “Understanding deviations between spatially resolved and homogenized cathode models of lithium-ion batteries,” *Energy Technology*, vol. 9, no. 6, p. 2000881, 2021. [Online]. Available: <https://onlinelibrary.wiley.com/doi/abs/10.1002/ente.202000881>
- [140] J. Zahnow, T. Bernges, A. Wagner, N. Bohn, J. R. Binder, W. G. Zeier, M. T. Elm, and J. Janek, “Impedance analysis of NCM cathode materials: Electronic and ionic partial conductivities and the influence of microstructure,” *ACS Applied Energy Materials*, vol. 4, no. 2, pp. 1335–1345, Feb. 2021. [Online]. Available: <https://doi.org/10.1021/acsaem.0c02606>
- [141] S. J. Cooper, A. Bertei, P. R. Shearing, J. A. Kilner, and N. P. Brandon, “TauFactor: An open-source application for calculating tortuosity factors

- from tomographic data,” *SoftwareX*, vol. 5, pp. 203–210, Jan. 2016.  
[Online]. Available:  
<https://www.sciencedirect.com/science/article/pii/S23527111016300280>
- [142] S. Kench, I. Squires, and S. Cooper, “TauFactor 2: A GPU accelerated python tool for microstructural analysis,” *Journal of Open Source Software*, vol. 8, no. 88, p. 5358, Aug. 2023. [Online]. Available:  
<https://joss.theoj.org/papers/10.21105/joss.05358>
- [143] G. Gaiselmann, M. Neumann, V. Schmidt, O. Pecho, T. Hocker, and L. Holzer, “Quantitative relationships between microstructure and effective transport properties based on virtual materials testing,” *AIChE Journal*, vol. 60, no. 6, pp. 1983–1999, 2014. [Online]. Available:  
<https://onlinelibrary.wiley.com/doi/abs/10.1002/aic.14416>
- [144] V. Becker, O. Birkholz, Y. Gan, and M. Kamlah, “Modeling the influence of particle shape on mechanical compression and effective transport properties in granular lithium-ion battery electrodes,” *Energy Technology*, vol. 9, no. 6, p. 2000886, 2021. [Online]. Available:  
<https://onlinelibrary.wiley.com/doi/abs/10.1002/ente.202000886>
- [145] O. Birkholz, Y. Gan, and M. Kamlah, “Modeling the effective conductivity of the solid and the pore phase in granular materials using resistor networks,” *Powder Technology*, vol. 351, pp. 54–65, Jun. 2019. [Online]. Available:  
<https://linkinghub.elsevier.com/retrieve/pii/S003259101930244X>
- [146] M. Neumann, O. Stenzel, F. Willot, L. Holzer, and V. Schmidt, “Quantifying the influence of microstructure on effective conductivity and permeability: Virtual materials testing,” *International Journal of Solids and Structures*, vol. 184, pp. 211–220, 2020.
- [147] O. Birkholz, M. Neumann, V. Schmidt, and M. Kamlah, “Statistical investigation of structural and transport properties of densely-packed assemblies of overlapping spheres using the resistor network method,”



- Powder Technology*, vol. 378, pp. 659–666, Jan. 2021. [Online]. Available:  
<https://linkinghub.elsevier.com/retrieve/pii/S0032591020309207>
- [148] D. a. G. Bruggeman, “Berechnung verschiedener physikalischer Konstanten von heterogenen Substanzen. I. Dielektrizitätskonstanten und Leitfähigkeiten der Mischkörper aus isotropen Substanzen,” *Annalen der Physik*, vol. 416, no. 7, pp. 636–664, 1935. [Online]. Available:  
<https://onlinelibrary.wiley.com/doi/abs/10.1002/andp.19354160705>
- [149] B. Tjaden, S. J. Cooper, D. J. Brett, D. Kramer, and P. R. Shearing, “On the origin and application of the Bruggeman correlation for analysing transport phenomena in electrochemical systems,” *Current Opinion in Chemical Engineering*, vol. 12, pp. 44–51, May 2016. [Online]. Available:  
<https://www.sciencedirect.com/science/article/pii/S2211339816300119>
- [150] O. Birkholz, *Modeling transport properties and electrochemical performance of hierarchically structured lithium-ion battery cathodes using resistor networks and mathematical half-cell models*. KIT Scientific Publishing, Oct. 2022. [Online]. Available:  
<https://www.ksp.kit.edu/site/books/m/10.5445/KSP/1000143556/>
- [151] A. M. Dreizler, N. Bohn, H. Geßwein, M. Müller, J. R. Binder, N. Wagner, and K. A. Friedrich, “Investigation of the influence of nanostructured  $\text{LiNi}_{0.33}\text{Co}_{0.33}\text{Mn}_{0.33}\text{O}_2$  lithium-ion battery electrodes on performance and aging,” *Journal of The Electrochemical Society*, vol. 165, no. 2, p. A273, Jan. 2018. [Online]. Available:  
<https://iopscience.iop.org/article/10.1149/2.1061802jes/meta>
- [152] O. Dolotko, A. Senyshyn, M. J. Mühlbauer, K. Nikolowski, and H. Ehrenberg, “Understanding structural changes in NMC Li-ion cells by in situ neutron diffraction,” *Journal of Power Sources*, vol. 255, pp. 197–203, 2014. [Online]. Available:  
<https://www.sciencedirect.com/science/article/pii/S0378775314000214>

- [153] A. O. Kondrakov, A. Schmidt, J. Xu, H. Geßwein, R. Mönig, P. Hartmann, H. Sommer, T. Brezesinski, and J. Janek, “Anisotropic lattice strain and mechanical degradation of high- and low-nickel NCM cathode materials for Li-ion batteries,” *The Journal of Physical Chemistry C*, vol. 121, no. 6, pp. 3286–3294, 2017. [Online]. Available: <https://doi.org/10.1021/acs.jpcc.6b12885>
- [154] L. de Biasi, A. O. Kondrakov, H. Geßwein, T. Brezesinski, P. Hartmann, and J. Janek, “Between scylla and charybdis: Balancing among structural stability and energy density of layered NCM cathode materials for advanced lithium-ion batteries,” *The Journal of Physical Chemistry C*, vol. 121, no. 47, pp. 26 163–26 171, 2017. [Online]. Available: <https://doi.org/10.1021/acs.jpcc.7b06363>
- [155] F. Strauß, L. de Biasi, A.-Y. Kim, J. Hertle, S. Schweidler, J. Janek, P. Hartmann, and T. Brezesinski, “Rational design of quasi-zero-strain NCM cathode materials for minimizing volume change effects in all-solid-state batteries,” *ACS Materials Letters*, vol. 2, no. 1, pp. 84–88, 2020. [Online]. Available: <https://doi.org/10.1021/acsmaterialslett.9b00441>
- [156] S. D. Kang, J. J. Kuo, N. Kapate, J. Hong, J. Park, and W. C. Chueh, “Galvanostatic intermittent titration technique reinvented: Part II. Experiments,” *Journal of The Electrochemical Society*, vol. 168, no. 12, p. 120503, 2021. [Online]. Available: <https://dx.doi.org/10.1149/1945-7111/ac3939>
- [157] S.-L. Wu, W. Zhang, X. Song, A. K. Shukla, G. Liu, V. Battaglia, and V. Srinivasan, “High rate capability of  $\text{Li}(\text{Ni}_{1/3}\text{Mn}_{1/3}\text{Co}_{1/3})\text{O}_2$  electrode for Li-ion batteries,” *Journal of The Electrochemical Society*, vol. 159, no. 4, pp. A438–A444, Jan. 2012. [Online]. Available: <http://jes.ecsdl.org/content/159/4/A438>
- [158] R. Amin and Y.-M. Chiang, “Characterization of electronic and ionic transport in  $\text{Li}_{1-x}\text{Ni}_{0.33}\text{Mn}_{0.33}\text{Co}_{0.33}\text{O}_2$  (NMC333) and

- $\text{Li}_{1-x}\text{Ni}_{0.50}\text{Mn}_{0.20}\text{Co}_{0.30}\text{O}_2$  (NMC523) as a function of Li content,” *Journal of The Electrochemical Society*, vol. 163, no. 8, pp. A1512–A1517, 2016. [Online]. Available: <https://iopscience.iop.org/article/10.1149/2.0131608jes>
- [159] J. J. Kuo, S. D. Kang, and W. C. Chueh, “Contact resistance of carbon- $\text{Li}_x(\text{Ni}, \text{Mn}, \text{Co})\text{O}_2$  interfaces,” *Advanced Energy Materials*, vol. 12, no. 31, p. 2201114, 2022. [Online]. Available: <https://onlinelibrary.wiley.com/doi/abs/10.1002/aenm.202201114>
- [160] M.-J. Lee, E. Lho, P. Bai, S. Chae, J. Li, and J. Cho, “Low-temperature carbon coating of nanosized  $\text{Li}_{1.015}\text{Al}_{0.06}\text{Mn}_{1.925}\text{O}_4$  and high-density electrode for high-power Li-ion batteries,” *Nano Letters*, vol. 17, no. 6, pp. 3744–3751, Jun. 2017. [Online]. Available: <https://doi.org/10.1021/acs.nanolett.7b01076>
- [161] N. Phattharasupakun, J. Wutthiprom, S. Duangdangchote, S. Sarawutanukul, C. Tomon, F. Duriyasart, S. Tubtimkuna, C. Aphirakaramwong, and M. Sawangphruk, “Core-shell Ni-rich NMC-nanocarbon cathode from scalable solvent-free mechanofusion for high-performance 18650 Li-ion batteries,” *Energy Storage Materials*, vol. 36, pp. 485–495, Apr. 2021. [Online]. Available: <https://www.sciencedirect.com/science/article/pii/S2405829721000386>
- [162] Z. Du, D. L. Wood, C. Daniel, S. Kalnaus, and J. Li, “Understanding limiting factors in thick electrode performance as applied to high energy density Li-ion batteries,” *Journal of Applied Electrochemistry*, vol. 47, no. 3, pp. 405–415, Mar. 2017. [Online]. Available: <https://doi.org/10.1007/s10800-017-1047-4>
- [163] Y. Kuang, C. Chen, D. Kirsch, and L. Hu, “Thick electrode batteries: Principles, opportunities, and challenges,” *Advanced Energy Materials*, vol. 9, no. 33, p. 1901457, 2019. [Online]. Available: <https://onlinelibrary.wiley.com/doi/abs/10.1002/aenm.201901457>

- [164] M. Xu, B. Reichman, and X. Wang, "Modeling the effect of electrode thickness on the performance of lithium-ion batteries with experimental validation," *Energy*, vol. 186, p. 115864, Nov. 2019. [Online]. Available: <https://linkinghub.elsevier.com/retrieve/pii/S0360544219315361>
- [165] Z. Hashin and S. Shtrikman, "A variational approach to the theory of the elastic behaviour of multiphase materials," *Journal of the Mechanics and Physics of Solids*, vol. 11, no. 2, pp. 127–140, 1963. [Online]. Available: <https://www.sciencedirect.com/science/article/pii/0022509663900607>
- [166] J. Landesfeind and H. A. Gasteiger, "Temperature and concentration dependence of the ionic transport properties of lithium-ion battery electrolytes," *Journal of The Electrochemical Society*, vol. 166, no. 14, p. A3079, Sep. 2019. [Online]. Available: <https://iopscience.iop.org/article/10.1149/2.0571912jes/meta>
- [167] F. M. I. L. VWR International, LLC, "Glass microfibre filters without binder, grade GF/C, Whatman," 2021. [Online]. Available: <https://de.vwr.com/store/product/en/16930809/glasmikrofaserfilter-ohne-binder-sorter-gf-c-whatmantm?languageChanged=en>
- [168] S. G. Stewart, V. Srinivasan, and J. Newman, "Modeling the performance of lithium-ion batteries and capacitors during hybrid-electric-vehicle operation," *Journal of The Electrochemical Society*, vol. 155, no. 9, p. A664, Jul. 2008. [Online]. Available: <https://iopscience.iop.org/article/10.1149/1.2953524/meta>
- [169] A. R. Boccaccini, D. R. Acevedo, G. Brusatin, and P. Colombo, "Borosilicate glass matrix composites containing multi-wall carbon nanotubes," *Journal of the European Ceramic Society*, vol. 25, no. 9, pp. 1515–1523, Jun. 2005. [Online]. Available: <https://www.sciencedirect.com/science/article/pii/S0955221904002511>
- [170] R. Balbierer, "Charakterisierung von Lithium-Ionen-Batterien und deren Komponenten mittels NMR-Methoden," 2021. [Online]. Available: <https://publikationen.bibliothek.kit.edu/1000130864>

# List of Figures

2.1	Working principle of an intercalation battery cell. . . . .	5
2.2	Crystal structures of intercalation materials. . . . .	7
2.3	Schematic of a discharge curve. . . . .	10
2.4	SEM images: Cross-section of hierarchically structured electrode E2, secondary particle of comparable powder to F900. .	12
2.5	Schematic of a Doyle-Fuller-Newman model. . . . .	14
3.1	Schematic of the hierarchically structured half-cell model. . . . .	17
3.2	Schematic of electric potential over cell thickness with potential drop due to contact resistance between the electrode and the current collector. . . . .	24
3.3	Fit of M-factor for ionic and electronic transport in the secondary particles. . . . .	27
3.4	Schematic of possible ionic transport paths across the electrode thickness. . . . .	28
3.5	Spherical particle inside a unit cell, oval particle with partially blocked surface. . . . .	30
3.6	SEM images: NMC111 powders A-D with different secondary particle porosity, electrochemically active surface area, and primary particle size. . . . .	34
3.7	Comparison of the modeled and experimental discharge behavior of the E1 reference cell at C/20, 1C, 3C, 5C. . . . .	37
3.8	SEM images: Ion-milled cross-sections of electrode Cal-3. . . . .	38
3.9	Comparison between experimental and modeled discharge curves of electrode Cal-1 at 1C and 7C. . . . .	41

4.1	Rate capability of electrodes with different electrochemically active surface area; influence of diffusivity in the active material, electronic conductivity of the active material, reaction rate on the cell performance at 5C. . .	46
4.2	Experimental rate capability of electrodes A and B with differing secondary particle porosity and size, modeled rate capability depending on secondary particle porosity. . . . .	48
4.3	Normalized concentration in the active material and electric potential in the solid phase at the end of a 5C discharge. . . . .	49
4.4	Influence of electronic conductivity within the secondary particles on the cell performance at 5C. . . . .	50
4.5	Influence of diffusivity in the active material and reaction rate on the cell performance at 5C. . . . .	51
4.6	Experimental rate capability of electrodes C and D with differing secondary and primary particle size, modeled rate capability depending on secondary particle size. . . . .	52
4.7	Normalized concentration in the active material and electric potential in the solid phase at the end of a 5C discharge. . . . .	53
4.8	Influence of electronic conductivity within the secondary particles on the cell performance at 5C. . . . .	54
4.9	Influence of diffusivity in the active material and reaction rate on the cell performance at 5C. . . . .	55
4.10	Modeled rate capability depending on primary particle size. . . . .	56
4.11	Difference in normalized concentration in the active material between primary particle surfaces and centers at the end of a 5C discharge, influence of diffusivity in the active material on the cell performance at 5C. . . . .	56
4.12	Influence of electronic conductivity of the active material and reaction rate on the cell performance at 5C. . . . .	58
4.13	Experimental and modeled rate capability depending on electrode thickness. . . . .	59
4.14	Normalized concentration in the active material and in the electrolyte at the end of a 5C discharge. . . . .	60
4.15	Rate capability when the conductivity and the diffusivity of the electrolyte are artificially increased by a factor of 10. . . . .	60

5.1	M-factors for ionic transport at cell level. . . . .	63
5.2	Salt concentration in the electrolyte and discharge curve of electrode Cal-1 at the end of a 10C discharge. . . . .	64
5.3	Salt concentration in the electrolyte of electrode Cal-2 at the end of a C/20, 1C, 3C, 5C discharge. . . . .	65
5.4	Salt concentration in the electrolyte of electrode Cal-3 at the end of a C/20, C/2, 1C, 2C discharge. . . . .	66
5.5	Discharge curve of electrode Cal-2 at 3C and 5C, of electrode Cal-3 at C/2 and 2C. . . . .	68
B.1	Open circuit voltage of the reference cell E1. . . . .	119
B.2	Open circuit voltage of electrodes Cal-1, Cal-2, and Cal-3. . . . .	123
D.1	Salt concentration in the electrolyte of electrode Cal-1 at the end of a C/20, C/2, 1C, 2C discharge. . . . .	132
D.2	Salt concentration in the electrolyte of electrode Cal-1 at the end of a 3C, 5C, 7C, 10C discharge. . . . .	133
D.3	Discharge curve of electrode Cal-1 at C/20, C/2, 1C, 2C discharge. . . . .	134
D.4	Discharge curve of electrode Cal-1 at 3C, 5C, 7C, 10C discharge. . . . .	135
D.5	Salt concentration in the electrolyte of electrode Cal-2 at the end of a C/20, C/2, 1C, 2C discharge. . . . .	136
D.6	Salt concentration in the electrolyte of electrode Cal-2 at the end of a 3C, 5C, 7C, 10C discharge. . . . .	137
D.7	Discharge curve of electrode Cal-2 at C/20, C/2, 1C, 2C discharge. . . . .	138
D.8	Discharge curve of electrode Cal-2 at 3C, 5C, 7C, 10C discharge. . . . .	139
D.9	Salt concentration in the electrolyte of electrode Cal-3 at the end of a C/20, C/2, 1C, 2C discharge. . . . .	140
D.10	Discharge curve of electrode Cal-3 at C/20, C/2, 1C, 2C discharge. . . . .	141





## List of Tables

3.1	Powder characteristics of the porous NMC111 materials. . . . .	35
3.2	Properties of hierarchically structured electrodes. . . . .	36
3.3	Electrode characteristics at different calendering steps. . . . .	39
5.1	Gravimetric energy density depending on the assumption for ionic transport. . . . .	67
B.1	Geometric properties of the reference cell E1. . . . .	120
B.2	Electrochemical properties of the reference cell E1 (Part 1). . . . .	121
B.3	Electrochemical properties of the reference cell E1 (Part 2). . . . .	122
B.4	Effective transport properties of the reference cell E1. . . . .	123
B.5	Geometric properties of electrodes Cal-1, Cal-2, and Cal-3. . . . .	124
B.6	Electrochemical properties of electrodes Cal-1, Cal-2, and Cal-3 (Part 1). . . . .	125
B.7	Electrochemical properties of electrodes Cal-1, Cal-2, and Cal-3 (Part 2). . . . .	126
B.8	Effective transport properties of electrodes Cal-1, Cal-2, and Cal-3. . . . .	127



# List of Abbreviations and Symbols

## Alphabetical Symbols

$A^{\text{pos}}$	cross-sectional area of the positive electrode	$\text{m}^2$
$A_{\text{s}}$	accessible surface area of the active material particles	$\text{m}^2$
$a_{\text{s}}$	electrochemically active surface area	$1/\text{m}$
$a_{\text{s}}^{(\text{I})}$	electrochemically active surface area of a hierarchically structured electrode	$1/\text{m}$
$A_{\text{sph}}$	surface area of a spherical particle	$\text{m}^2$
$a_{\text{sph}}$	electrochemically active surface area of spherical particles	$\text{m}^2$
$\bar{c}_{\text{e}}$	concentration of shuttling ions in the electrolyte at electrode level	$\text{mol}/\text{m}^3$
$\hat{c}_{\text{e}}$	normalized concentration of shuttling ions in the electrolyte	—
$\bar{c}_{\text{e},0}$	initial concentration of shuttling ions in the electrolyte	$\text{mol}/\text{m}^3$
$\bar{c}_{\text{e}}^{(\text{II})}$	concentration of shuttling ions in the electrolyte at secondary particle level	$\text{mol}/\text{m}^3$
$c_{\text{s}}$	concentration of shuttling ions in compact active material particles	$\text{mol}/\text{m}^3$

$c_{s,0}$	initial concentration of shuttling ions in the active material	$\text{mol/m}^3$
$c_{s,\max}$	maximum concentration of shuttling ions in the active material	$\text{mol/m}^3$
$c_s^{(I)}$	concentration of shuttling ions in the primary active material particles	$\text{mol/m}^3$
$D$	bulk transport property	
$D_{e,\text{eff}}$	effective diffusivity of the electrolyte at electrode level	$\text{m}^2/\text{s}$
$D_{e,\text{eff}}^{\text{sep}}$	effective diffusivity of the electrolyte in the separator	$\text{m}^2/\text{s}$
$D_{e,\text{eff}}^{(II)}$	effective diffusivity of the electrolyte at secondary particle level	$\text{m}^2/\text{s}$
$D_{\text{eff}}$	effective transport property	
$D_e$	diffusivity in the electrolyte	$\text{m}^2/\text{s}$
$D_s$	diffusivity in the active material	$\text{m}^2/\text{s}$
$D_i$	material property of phase $i$	
$\text{DOD}_0$	initial depth of discharge	–
$\text{DOD}_{\max}$	maximum depth of discharge	–
$E$	energy	J
$F$	Faraday's constant	As/mol
$i_{\text{app}}$	current density	A/m <sup>2</sup>
$\bar{j}$	flux density due to electrochemical reaction at the surface of compact active material particles	$\text{mol}/(\text{m}^2\text{s})$
$\bar{j}^{(I)}$	flux density due to electrochemical reaction at the surface of primary active material particles	$\text{mol}/(\text{m}^2\text{s})$
$k_0$	reaction rate constant	$\text{mol}^{\alpha-1}\text{m}^{4-3\alpha}/\text{s}$

---

$L^{\text{pos}}$	thickness of the positive electrode	m
$L^{\text{sep}}$	thickness of the separator	m
$M$	M-factor	—
$M^{\text{particles}}$	M-factor for effective transport through interconnected spherical particles	—
$M_{\text{eon}}^{(\text{II})}$	M-factor for effective electronic transport in the secondary particles	—
$M_{\text{eon}}^{\text{pos}}$	M-factor for effective electronic transport in the positive electrode	—
$M_{\text{ion}}^{(\text{II})}$	M-factor for effective ionic transport in the secondary particles	—
$M_{\text{ion}}^{\text{combi}}$	M-factor for effective ionic transport in the combined intra- plus intergranular pore space	—
$M_{\text{ion}}^{\text{intra}}$	M-factor for effective ionic transport in the intra-granular pore space	—
$M_{\text{ion}}^{\text{pos}}$	M-factor for effective ionic transport in the intergranular pore space	—
$M_{\text{ion}}^{\text{sep}}$	M-factor for effective ionic transport in the separator	—
$m_{\text{s}}$	active material mass	kg
$n$	C-rate	—
$n_{\text{eon}}$	number of electrons	—
$P$	power	W
$p$	deviation factor of electrochemically active surface area	—
$Q$	capacity	Ah
$Q_{\text{rev}}$	specific reversibly accessible capacity	Ah/kg

$Q_{\text{spec}}$	specific nominal capacity	Ah/kg
$R$	gas constant	J/(Kmol)
$r$	radial coordinate of the compact active material particles	m
$R^{(\text{II})}$	secondary particle radius	m
$r^{(\text{II})}$	radial coordinate of the secondary particles	m
$R^{(\text{I})}$	representative length of diffusion paths in the primary active material particles	m
$r^{(\text{I})}$	radial coordinate of the primary active material particles	m
$R_{\text{cont}}$	contact resistance between positive electrode and current collector	$\Omega\text{m}^2$
$R_{\text{p}}$	particle radius	m
$T$	temperature	K
$t$	time	h
$t_+$	transference number of the shuttling ions	–
$U_{\text{cell}}$	cell voltage	V
$U_{\text{OCV}}$	open-circuit voltage	V
$V$	unit cell volume	$\text{m}^3$
$V_{\text{sph}}$	volume of a spherical particle	$\text{m}^3$
$V_{\text{s}}$	volume of the active material particles	$\text{m}^3$
$w^{\text{sep}}$	area density of the separator	$\text{kg/m}^2$
$x$	through-thickness coordinate of the positive electrode	m

### Greek Symbols

$\alpha$	charge transfer coefficient	–
$\beta$	fitting parameter	–

$\gamma$	fitting parameter	—
$\Delta G$	change in Gibbs free energy	J/mol
$\varepsilon$	volume fraction	—
$\varepsilon_e^{\text{pos}}$	volume fraction of intergranular electrolyte in the positive electrode, intergranular porosity	—
$\varepsilon_e^{\text{sep}}$	volume fraction of electrolyte in the separator	—
$\varepsilon_e^{(\text{II})}$	volume fraction of electrolyte in the secondary particles, intragranular porosity	—
$\varepsilon_f^{\text{pos}}$	volume fraction of additives in the positive electrode	—
$\varepsilon_s$	volume fraction of compact active material particles in the positive electrode	—
$\varepsilon_s^{\text{pos}}$	volume fraction of porous secondary particles in the positive electrode	—
$\varepsilon_s^{\text{pos}} \bar{j}_c$	sink term due to electrons/ions (charge) entering the secondary particles	A/m <sup>3</sup>
$\varepsilon_s^{\text{pos}} \bar{j}_m$	sink term due to ions (mass) entering the secondary particles	A/m <sup>3</sup>
$\varepsilon_s^{(\text{II})}$	volume fraction of active material in the secondary particles	—
$\bar{\eta}^{(\text{II})}$	overpotential	V
$\theta$	contact angle	°
$\kappa$	conductivity of the electrolyte	S/m
$\kappa_{\text{D,eff}}$	effective diffusional conductivity of the electrolyte in the positive electrode	A/m
$\kappa_{\text{D,eff}}^{\text{sep}}$	effective diffusional conductivity of the electrolyte in the separator	A/m

$\kappa_{D,\text{eff}}^{(\text{II})}$	effective diffusional conductivity of the electrolyte in the secondary particles	A/m
$\kappa_D$	diffusional conductivity of the electrolyte	A/m
$\kappa_{\text{eff}}$	effective conductivity of the electrolyte in the positive electrode	S/m
$\kappa_{\text{eff}}^{\text{sep}}$	effective conductivity of the electrolyte in the separator	S/m
$\kappa_{\text{eff}}^{(\text{II})}$	effective conductivity of the electrolyte in the secondary particles	S/m
$V_{\text{tdf}}$	thermodynamic factor	—
$\xi$	degree of lithiation/sodiation	—
$\rho^{\text{sep}}$	density of the separator	kg/m <sup>3</sup>
$\rho_{\text{bsg}}$	density of borosilicate glass	kg/m <sup>3</sup>
$\rho_s$	density of the active material	kg/m <sup>3</sup>
$\sigma$	electronic conductivity of the additives	S/m
$\sigma^{(\text{II})}$	electronic conductivity of the active material in the secondary particles	S/m
$\sigma_{\text{eff}}$	effective electronic conductivity of the additives	S/m
$\sigma_{\text{eff}}^{(\text{II})}$	effective electronic conductivity of the secondary particles	S/m
$\bar{\phi}_e$	electrochemical potential in the electrolyte at electrode level	V
$\bar{\phi}_e^{(\text{II})}$	electrochemical potential in the electrolyte at secondary particle level	V
$\bar{\phi}_s$	electric potential in the solid phase at electrode level	V
$\bar{\phi}_s^{(\text{II})}$	electric potential in the solid phase at secondary particle level	V



$\Delta\bar{\phi}_s$	potential drop	V
----------------------	----------------	---

**Abbreviations**

BET	Brunauer-Emmett-Teller
DFN model	Doyle-Fuller-Newman model
DOD	depth of discharge
FE-SEM	field emission scanning electron microscopy
HSCM	hierarchically structured half-cell model
HSE	hierarchically structured electrode
LIB	lithium-ion battery
NASICON	sodium superionic conductor
NIB	sodium-ion battery
NMC	lithium nickel manganese cobalt oxide
NMC111	$\text{LiNi}_{1/3}\text{Mn}_{1/3}\text{Co}_{1/3}\text{O}_2$
NMP	N-methyl-2-pyrrolidone
OCV	open-circuit voltage
PVDF	polyvinylidene fluoride
SOC	state of charge
SPM	single particle model



# A Cell Production and Experimental Testing


## A.1 Electrodes A-D and E1-E4

To compare the modeled data with experimental data in Chapter 4, Joachim R. Binder's group at the Karlsruhe Institute of Technology<sup>1</sup> prepared powders with different secondary particle porosity, electrochemically active surface area, and primary particle size<sup>2</sup>. For this, they milled a commercially available  $\text{LiNi}_{1/3}\text{Mn}_{1/3}\text{Co}_{1/3}\text{O}_2$  (NMC111) powder (NM-3100, Toda America) in an agitator bead mill with different grinding media sizes (0.2 mm and 0.1 mm) and spray dried it to form spherical secondary particles. Afterward, they sintered the two powders at different temperatures (A and B: 800 °C for 5 h, C: 850 °C for 5 h and D: 800°C for 1 h and 700 °C for 10 h) under air to adjust the primary particle size and porosity.

They characterized all powders as follows: Secondary particle size by laser diffraction, electrochemically active surface area by BET method with  $\text{N}_2$  adsorption, secondary particle porosity by mercury intrusion, and primary particle size by FE-SEM investigations in combination with image analysis. The detailed processing route and powder characterization were described in Wagner et al. [15] and Dreizler et al. [151].

---

<sup>1</sup> Dr. Joachim R. Binder, Institute for Applied Materials, Karlsruhe Institute of Technology, 76344 Eggenstein-Leopoldshafen, Germany, joachim.binder@kit.edu

<sup>2</sup> This chapter has previously been published in Naumann et al. (2023) [1] . The text has been modified.


For electrochemical tests, they produced electrodes by mixing NMC111 powder, PVDF binder (Solef 5130, Solvay Solexis), carbon black (Super C65, Imerys Graphite & Carbon), and graphite (KS6L Imerys Graphite & Carbon) in an 87:4:4:5 ratio (wt-%) in N-methyl-2-pyrrolidone (NMP). They doctor bladed the slurry on an aluminum current collector at 200  $\mu\text{m}$  gap height and dried it overnight at 80°C. After drying, they slightly compacted the electrodes.

From the prepared electrodes, a Whatman GF/C separator, electrolyte (LP30), and a lithium metal negative electrode they built Swagelok-type and CR2032 coin-type cells. For electrochemical testing, they used a BT2000 battery cycler from Arbin Instruments. They performed galvanostatic cycling at discharge rates of C/20, C/2, 1C, 2C, 3C, 5C, 7C, and 10C in a voltage range between 4.3 - 3.0 V.

## A.2 Electrodes Cal-1, Cal-2, and Cal-3

Electrodes Cal-1, Cal-2 and Cal-3 contained modified NM-3100 (NMC111) by Toda Kogyo Corp., C-ENERGY Super C65 (carbon black) and C-ENERGY KS6L (graphite) by Imerys Graphite & Carbon Switzerland, and Solef 5130 (PVDF binder) by Solvay S.A.<sup>3</sup>. The total solid content in the slurry amounted to 20.4 Vol% with a 3.3  $\text{m}^2\text{g}^{-1}$  BET surface area [88] of the active material powder. Previous publications report detailed experimental characterization and synthesis of the electrodes [88] as well as electrodes with a similar active material [15, 93]. After coating and drying, the electrodes were calendered to three different porosities (Cal-1, Cal-2, Cal-3).

---

<sup>3</sup> The following chapter has previously been published in Naumann et al. (2024) [2] . The text has been modified.

## B Cell Properties

To study the designated electrodes with the hierarchically structured half-cell model (HSCM, Chapter 3.1), I acquired the necessary parameters describing their microstructure (Tab. B.1, B.4, B.5, and B.8) as well as the material properties (Tab. B.2, B.3, B.6, and B.7) of the active material, the electrolyte, and the additives. At a discharge rate of  $C/20$ , dynamic effects on the cell performance are typically considered to be negligible. Therefore, I assumed the experimental  $C/20$  discharge curve of an electrode to represent its OCV (Fig. B.1 and B.2) and the maximum specific capacity at  $C/20$  to represent its reversibly accessible capacity. The initial depth of discharge (Eq. B.7) as well as the initial (Eq. B.6) and maximum (B.5) concentration in the active material can be calculated from the nominal and reversibly accessible capacity.

From the experimental partners<sup>1</sup>, I received microstructure parameters including particle sizes and volume fractions of the electrode components. M-factors of the electrode have been derived in Chapters 3.2 and 3.3. I used literature values for the M-factor of the separator as well as for the material properties, accounting for the dependence of electrolyte properties on the degree of lithiation (Eq. B.2, B.3, and B.4) [166]. The remaining separator properties were obtained from the specification of the manufacturer [167].

Chapter B.1 contains the parameters for electrode E1, which served as a reference electrode for the simulations in Chapter 4. The parameters for electrodes Cal-1,

---

<sup>1</sup> contact information: Dr. Joachim R. Binder and Dr. Marcus Müller, Institute for Applied Materials, Karlsruhe Institute of Technology, 76344 Eggenstein-Leopoldshafen, Germany, joachim.binder@kit.edu, marcus.mueller@kit.edu.

Cal-2, and Cal-3 from Chapter 5 are presented in Chapter B.2. Furthermore, the following functions were used for all studies with the HSCM <sup>2</sup>

$$\varepsilon_e^{\text{sep}} = 1 - \frac{\rho^{\text{sep}}}{\rho_{\text{bsg}}} = 1 - \frac{w^{\text{sep}}}{L^{\text{sep}}}, \quad (\text{B.1})$$

$$\begin{aligned} \kappa = & \left( 0.0798(1 + (T - 228))(1 - 1.22\sqrt{\hat{c}_e} \right. \\ & + 0.509(1 - 0.004 \exp(1000/T))\hat{c}_e)\hat{c}_e / \\ & \left. (1 + (0.00379 \exp(1000/T))\hat{c}_e^4) \right) \text{ S m}^{-1}, \quad (\text{B.2}) \end{aligned}$$

$$\begin{aligned} D_e = 1.47 \cdot 10^{-7} \cdot \exp \left( 1.33 \cdot \hat{c}_e - \frac{1.69 \cdot 10^3}{T} \right. \\ \left. - \frac{5.63 \cdot 10^2}{T} \cdot \hat{c}_e \right) \text{ m}^2 \text{ s}^{-1}, \quad (\text{B.3}) \end{aligned}$$

$$\begin{aligned} v_{\text{idf}} = & -5.58 + 7.17\hat{c}_e + 0.038T + 1.91\hat{c}_e^2 \\ & - 0.0665\hat{c}_e T - 0.0000508T^2 + 0.11\hat{c}_e^3 \\ & - 0.0061\hat{c}_e^2 T + 0.000151\hat{c}_e T^2, \quad (\text{B.4}) \end{aligned}$$


$$c_{\text{s,max}} = \frac{\text{DOD}_{\text{max}} Q_{\text{spec}} \rho_{\text{s}}}{F} = \frac{Q_{\text{spec}} \rho_{\text{s}}}{F}, \quad (\text{B.5})$$

$$c_{\text{s},0} = \frac{\text{DOD}_0 Q_{\text{spec}} \rho_{\text{s}}}{F} \quad (\text{B.6})$$

with

$$\hat{c}_e = \frac{\bar{c}_e}{\bar{c}_{e,0}}, \frac{\bar{c}_e^{(\text{II})}}{\bar{c}_{e,0}},$$

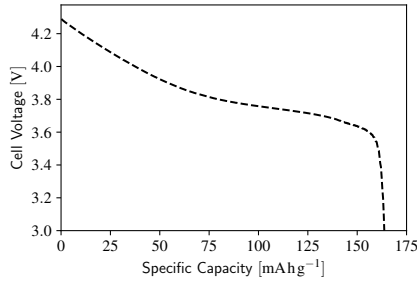
---

<sup>2</sup> These functions have previously been published in Naumann et al. (2023) [2] 


$$\text{DOD}_0 = \frac{Q_{\text{spec}} - Q_{\text{rev}}}{Q_{\text{spec}}}, \quad (\text{B.7})$$

$$a_s^{(1)} [\text{m}^2 \text{g}^{-1}] = \frac{a_s^{(1)} [\text{m}^{-1}]}{\rho_s}. \quad (\text{B.8})$$

## B.1 Reference Cell E1



**Figure B.1:** Open circuit voltage  $U_{\text{OCV}}$  of the reference cell E1 (experimental discharge curve at  $C/20$ ).

Measurements by Amalia Wagner and Nicole Bohn. This image has previously been published in Naumann et al. (2023) [1] .

**Table B.1:** Geometric properties of the reference cell E1.

This table has previously been published in Naumann et al. (2023) [1] 

Parameter	Value	Description	Source
$L^{\text{sep}}$	260 $\mu\text{m}$	thickness of the separator	[167]
$L^{\text{pos}}$	46 $\mu\text{m}$	thickness of the positive electrode	
$R^{(\text{II})}$	6.5 $\mu\text{m}$	radius of the secondary particles	
$R^{(\text{I})}$	$1.5 \cdot 0.255 \mu\text{m}$	representative length of diffusion paths within the primary active material particles	
$\epsilon_{\text{e}}^{\text{sep}}$	Eq. B.1	volume fraction of electrolyte in the separator	
$\epsilon_{\text{e}}^{\text{pos}}$	$1 - \epsilon_{\text{s}}^{\text{pos}} - \epsilon_{\text{f}}^{\text{pos}}$	volume fraction of intergranular electrolyte in the positive electrode	
$\epsilon_{\text{s}}^{\text{pos}}$	0.5762	volume fraction of secondary particles in the positive electrode	
$\epsilon_{\text{f}}^{\text{pos}}$	0.1373	volume fraction of additives in the positive electrode	
$\epsilon_{\text{e}}^{(\text{II})}$	$1 - \epsilon_{\text{s}}^{(\text{II})}$	volume fraction of electrolyte in the secondary particles = intragranular porosity	
$\epsilon_{\text{s}}^{(\text{II})}$	0.6480	volume fraction of NMC111 in the secondary particles	
$a_{\text{s}}^{(\text{I})}$	$3 \frac{\epsilon_{\text{s}}^{(\text{II})}}{R^{(\text{I})}/1.5}$	electrochemically active surface area of the electrode	



**Table B.2:** Electrochemical properties of the reference cell E1 (Part 1).This table has previously been published in Naumann et al. (2023) [1] .

Parameter	Value	Description	Source
$U_{\text{OCV}}$	Fig. B.1	open circuit voltage	
$R_{\text{cont}}$	0	contact resistance between electrode and current collector	
$\sigma$	$100 \text{ S m}^{-1}$	electronic conductivity of the additives	[168]
$\sigma^{(\text{II})}$	$8 \cdot 10^{-5} \text{ S m}^{-1}$	electronic conductivity of NMC111	[140], [a]
$\kappa$	Eq. B.2	conductivity of the electrolyte	[166]
$\kappa_{\text{D}}$	$-\frac{2RT}{F} \kappa_{\text{e}} v_{\text{df}}(1 - t_+)$	diffusional conductivity of the electrolyte	[166]
$D_{\text{e}}$	Eq. B.3	diffusivity in the electrolyte	[166]
$D_{\text{s}}$	$5 \cdot 10^{-16} \text{ m}^2 \text{ s}^{-1}$	diffusivity in NMC111	[157], [a]
$k_0$	$10^{-10} \text{ mol}^{\alpha-1} \text{ m}^{4-3\alpha} \text{ s}^{-1}$	reaction rate constant	[16]
$\alpha$	0.5	charge transfer coefficient	assumption


[a] Fitting parameter.

**Table B.3:** Electrochemical properties of the reference cell E1 (Part 2).

This table has previously been published in Naumann et al. (2023) [1] 

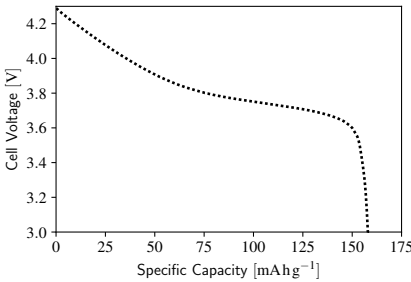
Parameter	Value	Description	Source
$V_{\text{df}}$	Eq. B.4	thermodynamic factor	[166]
$t_+$	0.23	transference number of the lithium ion	[16], [166]
$c_{\text{s,max}}$	Eq. B.5	maximum concentration in NMC111	[16]
$c_{\text{s},0}$	Eq. B.6	initial concentration in NMC111	[16]
$\bar{c}_{\text{e},0}$	1000 mol m <sup>-3</sup>	initial concentration in the electrolyte	
$\rho_{\text{s}}$	4770 kg m <sup>-3</sup>	density of NMC111	[68]
$\rho_{\text{bsg}}$	2.23 g cm <sup>-3</sup>	density of borosilicate glass	[169]
$w^{\text{sep}}$	53 g m <sup>-2</sup>	area density of the separator	[167]
$Q_{\text{spec}}$	278 mAh g <sup>-1</sup>	specific nominal capacity	[150]
$Q_{\text{rev}}$	164 mAh g <sup>-1</sup>	specific reversibly accessible capacity	
$T$	298 K	temperature	

**Table B.4:** Effective transport properties of the reference cell E1.


This table has previously been published in Naumann et al. (2023) [1] .


Parameter	Value	Description	Source
$D_{\text{eff}}$	Eq. 3.31	effective transport property	
$M_{\text{ion}}^{\text{sep}}$	$(\epsilon_{\text{e}}^{\text{sep}})^{1.42}$	M-factor for ionic transport in the separator	[170]
$M_{\text{ion}}^{\text{pos}}$	Eq. 3.33	M-factor for ionic transport in the positive electrode	[16, 147]
$M_{\text{con}}^{\text{pos}}$	Eq. 3.34	M-factor for electronic transport in the positive electrode	[16, 147]
$M_{\text{ion}}^{(\text{II})}$	Eq. 3.36	M-factor for ionic transport in the secondary particles	[123]
$M_{\text{con}}^{(\text{II})}$	Eq. 3.37	M-factor for electronic transport in the secondary particles	[123]

## B.2 Electrodes Cal-1, Cal-2, and Cal-3




**Figure B.2:** Open circuit voltage  $U_{\text{OCV}}$  of electrodes Cal-1, Cal-2, and Cal-3 (experimental discharge curve of electrode Cal-1 at C/20) [88].

This image has previously been published in Naumann et al. (2024) [2] .


**Table B.5:** Geometric properties of electrodes Cal-1, Cal-2, and Cal-3.  
This table has previously been published in Naumann et al. (2024) [2] 

Parameter	Value	Description	Source
$L^{\text{sep}}$	260 $\mu\text{m}$	thickness of the separator	[167]
$L^{\text{pos}}$	Tab. 3.3	thickness of the positive electrode	
$R^{(\text{II})}$	5 $\mu\text{m}$	radius of the secondary particles	[88]
$R^{(\text{I})}$	$1.5 \cdot 0.175 \mu\text{m}$	representative length of diffusion paths within the primary active material particles	[88]
$\epsilon_{\text{e}}^{\text{sep}}$	Eq. B.1	volume fraction of electrolyte in the separator	
$\epsilon_{\text{e}}^{\text{pos}}$	Tab. 3.3	volume fraction of intergranular electrolyte in the positive electrode	
$\epsilon_{\text{s}}^{\text{pos}}$	Tab. 3.3	volume fraction of secondary particles in the positive electrode	
$\epsilon_{\text{f}}^{\text{pos}}$	Tab. 3.3	volume fraction of additives in the positive electrode	
$\epsilon_{\text{e}}^{(\text{II})}$	$1 - \epsilon_{\text{s}}^{(\text{II})}$	volume fraction of electrolyte in the secondary particles	[88]
		= intragranular porosity	
$\epsilon_{\text{s}}^{(\text{II})}$	0.558	volume fraction of NMC111 in the secondary particles	[88]
$a_{\text{s}}^{(\text{I})}$	$3 \frac{\epsilon_{\text{s}}^{(\text{II})}}{R^{(\text{I})}/1.5}$	electrochemically active surface area of the electrode	


**Table B.6:** Electrochemical properties of electrodes Cal-1, Cal-2, and Cal-3 (Part 1).This table has previously been published in Naumann et al. (2024) [2] .

Parameter	Value	Description	Source
$U_{OCV}$	Fig. B.2	open circuit voltage	[88]
$R_{cont}$	Tab. 3.3	contact resistance between electrode and current collector	
$\sigma$	$100 \text{ S m}^{-1}$	electronic conductivity of the additives	[168]
$\sigma^{(II)}$	$3 \cdot 10^{-5} \text{ S m}^{-1}$	electronic conductivity of NMC111	[140], [a]
$\kappa$	Eq. B.2	conductivity of the electrolyte	[166]
$\kappa_D$	$-\frac{2RT}{F} \kappa_e v_{df}(1 - t_+)$	diffusional conductivity of the electrolyte	[166]
$D_e$	Eq. B.3	diffusivity in the electrolyte	[166]
$D_s$	Eq. 3.52	diffusivity in NMC111	[a]
$k_0$	$10^{-10} \text{ mol}^{\alpha-1} \text{ m}^{4-3\alpha} \text{ s}^{-1}$	reaction rate constant	[16]
$\alpha$	0.5	charge transfer coefficient	assumption

[a] Fitting parameter.

**Table B.7:** Electrochemical properties of electrodes Cal-1, Cal-2, and Cal-3 (Part 2).  
This table has previously been published in Naumann et al. (2024) [2] 

Parameter	Value	Description	Source
$V_{\text{df}}$	Eq. B.4	thermodynamic factor	[166]
$t_+$	0.23	transference number of the lithium ion	[16, 166]
$c_{\text{s,max}}$	Eq. B.5	maximum concentration in NMC111	[16]
$c_{\text{s},0}$	Eq. B.6	initial concentration in NMC111	[16]
$\bar{c}_{\text{e},0}$	1000 mol m <sup>-3</sup>	initial concentration in the electrolyte	
$\rho_{\text{s}}$	4770 kg m <sup>-3</sup>	density of NMC111	[68]
$\rho_{\text{bsg}}$	2.23 g cm <sup>-3</sup>	density of borosilicate glass	[169]
$w^{\text{sep}}$	53 g m <sup>-2</sup>	area density of the separator	[167]
$Q_{\text{spec}}$	278 mAh g <sup>-1</sup>	specific nominal capacity	[150]
$Q_{\text{rev}}$	158 mAh g <sup>-1</sup>	specific reversibly accessible capacity	
$T$	298 K	temperature	

**Table B.8:** Effective transport properties of electrodes Cal-1, Cal-2, and Cal-3.This table has previously been published in Naumann et al. (2024) [2] 

Parameter	Value	Description	Source
$D^{\text{eff}}$	Eq. 3.31	effective transport property	
$M_{\text{ion}}^{\text{sep}}$	$(\epsilon_e^{\text{sep}})^{1.42}$	M-factor for ionic transport in the separator	[170]
$M_{\text{ion}}^{\text{pos}}$	Eq. 3.33	M-factor for ionic transport in the positive electrode (purely intergranular assumption)	
$M_{\text{ion}}^{\text{combi}}$	Eq. 3.42	M-factor for ionic transport in the positive electrode (combined intragranular plus intergranular assumption)	
$M_{\text{eon}}^{\text{pos}}$	Eq. 3.34	M-factor for electronic transport in the positive electrode	[16, 147]
$M_{\text{ion}}^{(\text{II})}$	Eq. 3.36	M-factor for ionic transport in the secondary particles	[123]
$M_{\text{eon}}^{(\text{II})}$	Eq. 3.37	M-factor for electronic transport in the secondary particles	[123]





## C Hashin-Shtrikman Bound

The upper bound for material properties of multiphase system consisting of  $m$  phases with material property  $D_i$  and volume fraction  $\varepsilon_i$  of phase  $i$  with  $D_1 \leq D_2 \leq \dots \leq D_m$  [165]<sup>1</sup> is

$$D_{\text{eff}} \leq D_m + \frac{A_m}{1 - \alpha_m A_m} \quad (\text{C.1})$$

with

$$\alpha_i = (3D_i)^{-1}, \quad (\text{C.2})$$

$$A_m = \sum_{i=1}^{m-1} \frac{\varepsilon_i}{(D_i - D_m)^{-1} + \alpha_m}. \quad (\text{C.3})$$

Material properties with respect to ionic transport and volume fractions are

- for the additive phase

$$D_1 = 0, \quad (\text{C.4})$$


$$\varepsilon_1 = \varepsilon_{\text{f}}^{\text{pos}}, \quad (\text{C.5})$$

- for the porous particle phase

$$D_2 = M_{\text{ion}}^{(\text{II})} D, \quad (\text{C.6})$$

$$\varepsilon_2 = \varepsilon_{\text{s}}^{\text{pos}}, \quad (\text{C.7})$$

---

<sup>1</sup> The following chapter has previously been published in Naumann et al. (2024) [2] . The text has been modified.

- for the intergranular pore phase

$$D_m = D_3 = D, \quad (\text{C.8})$$

$$\varepsilon_3 = \varepsilon_e^{\text{pos}}. \quad (\text{C.9})$$

It follows

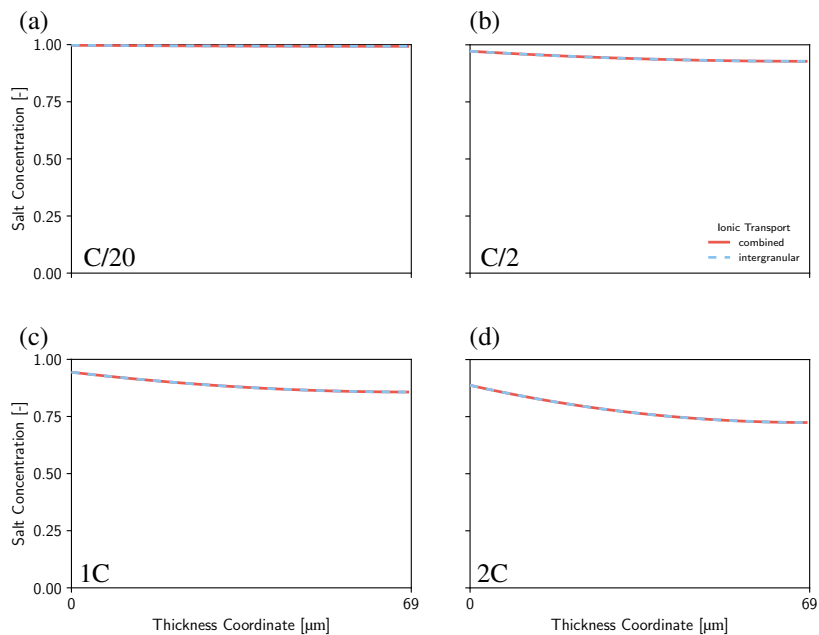
$$\alpha_m = \frac{1}{3D}, \quad (\text{C.10})$$

$$A_m = \left( \frac{\frac{\varepsilon_s^{\text{pos}}}{1} - \frac{3\varepsilon_f^{\text{pos}}}{2}}{\frac{1}{M_{\text{ion}}^{(\text{II})}} + \frac{1}{3}} \right) D, \quad (\text{C.11})$$

$$D_{\text{eff}} \leq \left( \frac{1 + \frac{\left( \frac{\varepsilon_s^{\text{pos}}}{1} - \frac{3\varepsilon_f^{\text{pos}}}{2} \right)}{M_{\text{ion}}^{(\text{II})} - 1 + \frac{1}{3}}}{1 - \frac{1}{3} \left( \frac{\varepsilon_s^{\text{pos}}}{1} - \frac{3\varepsilon_f^{\text{pos}}}{2} \right)} \right) D. \quad (\text{C.12})$$

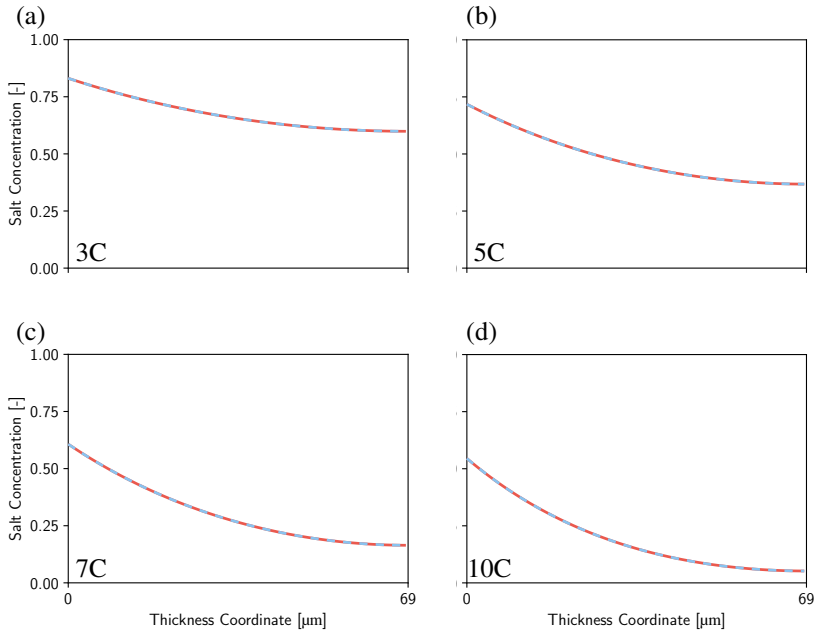
## **D      Extensive Simulation Results of Electrodes Cal-1, Cal-2, and Cal-3**

This Chapter presents the complete set of simulation results for electrodes Cal-1, Cal-2, and Cal-3 from Chapter 5. Using the purely intergranular assumption (Eq. 3.38) as well as the combined intra- plus intergranular assumption (Eq. 3.39) for ionic transport across the electrode, the salt concentration profile in the electrolytes at the end of discharge (Fig. D.1, D.2, D.5, D.6, and D.9) as well as the discharge curves (Fig. D.3, D.4, D.7, D.8, D.10) were obtained for discharge rates between  $C/20$  and  $10C$ . As a reference, the experimental discharge curves are displayed as well.




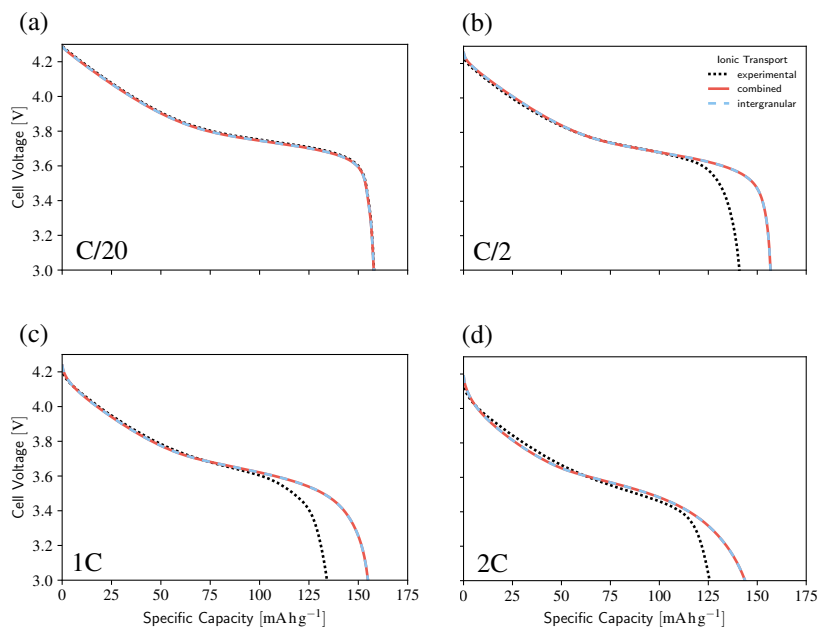
**Figure D.1:** Salt concentration in the electrolyte of electrode Cal-1 at the end of a (a)  $C/20$ , (b)  $C/2$ , (c)  $1C$ , (d)  $2C$  discharge.

These images have previously been published in Naumann et al. (2024) [2] .




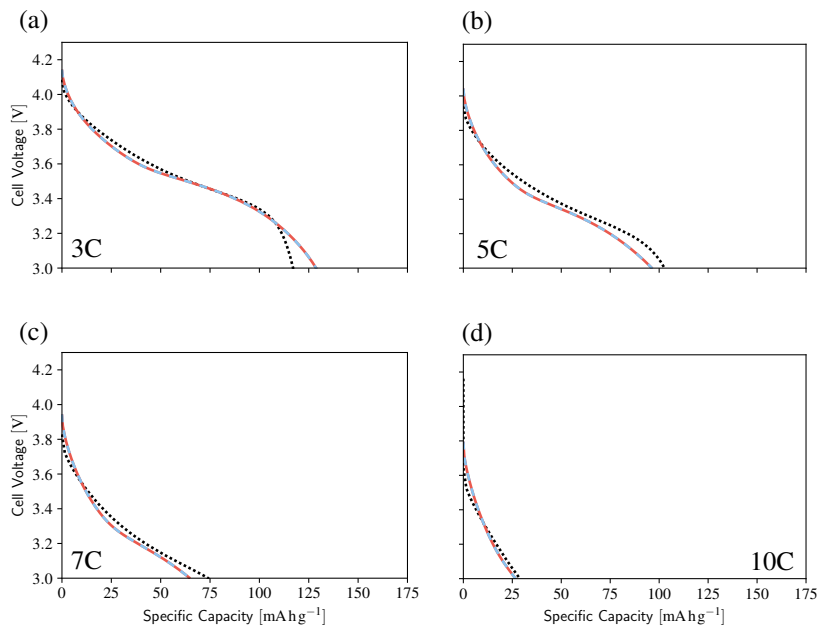
**Figure D.2:** Salt concentration in the electrolyte of electrode Cal-1 at the end of a (a) 3C, (b) 5C, (c) 7C, (d) 10C discharge.

These images have previously been published in Naumann et al. (2024) [2] .




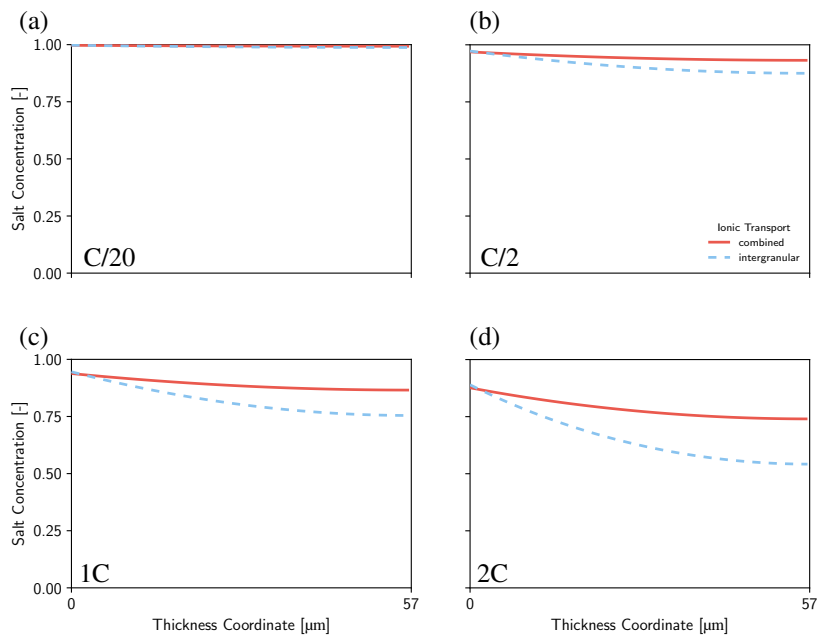
**Figure D.3:** Discharge curve of electrode Cal-1 at (a) C/20, (b) C/2, (c) 1C, (d) 2C discharge.

Experimental results by Marcus Müller and Nicole Bohn. These images have previously been published in Naumann et al. (2024) [2] .




**Figure D.4:** Discharge curve of electrode Cal-1 at (a) 3C, (b) 5C, (c) 7C, (d) 10C discharge.

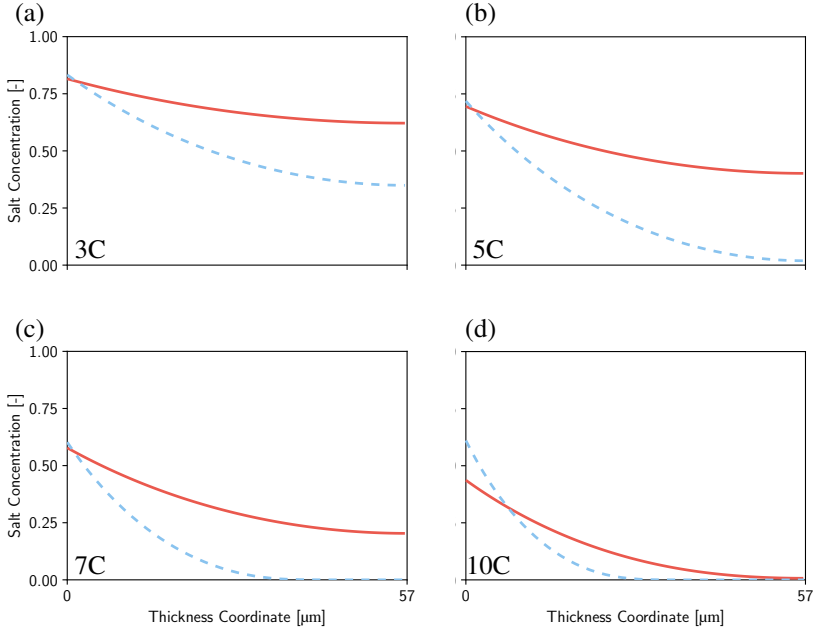
Experimental results by Marcus Müller and Nicole Bohn. These images have previously been published in Naumann et al. (2024) [2] .




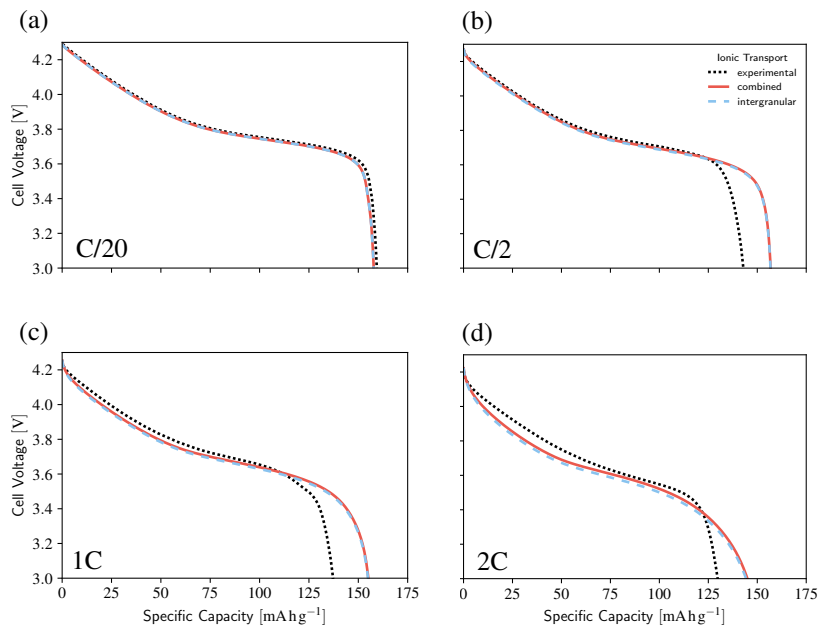
**Figure D.5:** Salt concentration in the electrolyte of electrode Cal-2 at the end of a (a) C/20, (b) C/2, (c) 1C, (d) 2C discharge.

These images have previously been published in Naumann et al. (2024) [2] .




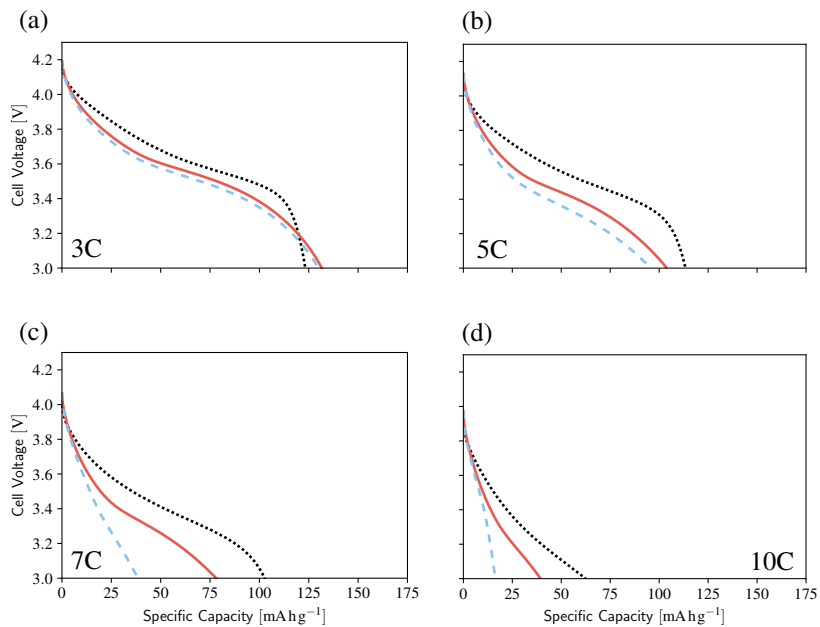



**Figure D.6:** Salt concentration in the electrolyte of electrode Cal-2 at the end of a (a) 3C, (b) 5C, (c) 7C, (d) 10C discharge. These images have previously been published in Naumann et al. (2024) [2] .

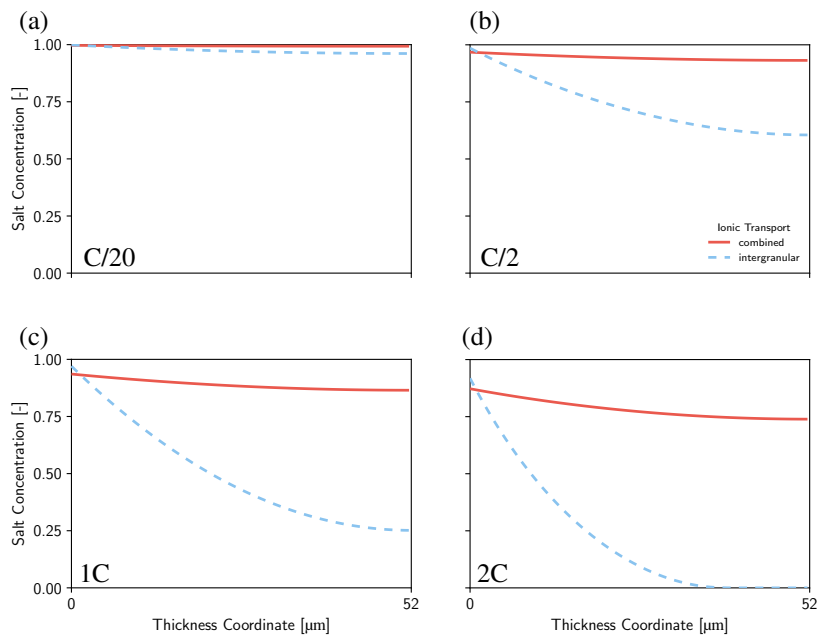


**Figure D.7:** Discharge curve of electrode Cal-2 at (a) C/20, (b) C/2, (c) 1C, (d) 2C discharge.

Experimental results by Marcus Müller and Nicole Bohn. These images have previously been published in Naumann et al. (2024) [2] .

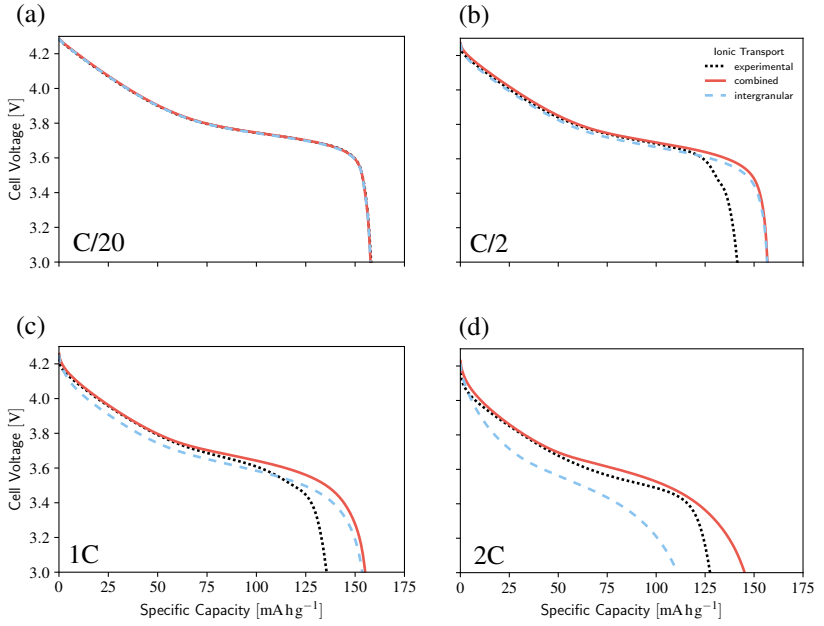


**Figure D.8:** Discharge curve of electrode Cal-2 at (a) 3C, (b) 5C, (c) 7C, (d) 10C discharge. Experimental results by Marcus Müller and Nicole Bohn. These images have previously been published in Naumann et al. (2024) [2] .




**Figure D.9:** Salt concentration in the electrolyte of electrode Cal-3 at the end of a (a)  $C/20$ , (b)  $C/2$ , (c)  $1C$ , (d)  $2C$  discharge.

These images have previously been published in Naumann et al. (2024) [2] .



**Figure D.10:** Discharge curve of electrode Cal-3 at (a) C/20, (b) C/2, (c) 1C, (d) 2C discharge.

Experimental results by Marcus Müller and Nicole Bohn. These images have previously been published in Naumann et al. (2024) [2] .